



UNIVERSITÀ DEGLI STUDI DI TRIESTE

XXXIII CICLO DEL DOTTORATO DI RICERCA IN NANOTECNOLOGIE

N-doped Graphene on Ni: growth, structure and reactivity

Settore scientifico-disciplinare: FIS/03 - Fisica della Materia

DOTTORANDA
SARA FIORI

Sara Fiori

COORDINATORE
PROF. ALBERTO MORGANTE

Alberto Morgante

SUPERVISORE DI TESI
DR. CRISTINA AFRICH

Cristina Africh

TUTOR
DR. MIRCO PANIGHEL

Mirco Panighele

ANNO ACCADEMICO 2019/2020



UNIVERSITÀ DEGLI STUDI DI TRIESTE

XXXIII CICLO DEL DOTTORATO DI RICERCA IN NANOTECNOLOGIE

N-doped Graphene on Ni: growth, structure and reactivity

settore scientifico-disciplinare FIS/03 - Fisica della Materia

STUDENT Sara Fiori

SCHOOL DIRECTOR Prof. Alberto Morgante

SUPERVISOR Dr. Cristina Africh

CO-SUPERVISOR Dr. Mirco Panighel

Academic year 2019/2020

List of Publications

- **S. Fiori**, D. Perilli, M. Panighel, C. Cepek, A. Ugolotti, A. Sala, H. Liu, G. Comelli, C. Di Valentin and C. Africh. Inside out Growth Method for High Quality Nitrogen Doped Graphene. *Carbon* 171 (2021) 704 - 710
- D. Perilli, **S. Fiori**, M. Panighel, H. Liu, C. Cepek, M. Peressi, G. Comelli, C. Africh and C. Di Valentin. Mechanism of CO intercalation through the Graphene/Ni(111) Interface and Effect of Doping. *J. Phys. Chem. Lett.* 2020, 11, 8887 - 8892
- S. Del Puppo, V. Carnevali, D. Perilli, F. Zarabara, A. Lodi Rizzini, G. Fornasier, E. Zupanič, **S. Fiori**, L. L. Patera, M. Panighel, Z. Zou, G. Comelli, C. Africh, C. Cepek, C. Di Valentin, and M. Peressi. Tuning graphene doping by carbon monoxide intercalation at the Ni(111) interface. *Carbon accepted*

Abstract

The experimental work presented in this PhD thesis fits into the fields of gas sensors, gas storage and catalysis under-cover. In particular, this thesis focuses on the characterization of the growth, structure and reactivity upon carbon monoxide exposure of pristine and nitrogen-doped graphene on Ni(111), mainly by Scanning Tunneling Microscopy (STM) and X-ray Photoemission Spectroscopy (XPS), supported by Low-Energy Electron Diffraction (LEED). The experimental measurements were corroborated by theoretical calculations in collaboration with the University of Milano-Bicocca (group of Prof. Cristiana Di Valentin) and the University of Trieste (group of Prof. Maria Peressi).

Nowadays, graphene is widely studied for a variety of applications and its already fascinating properties can be tuned and at times enhanced by introducing doping centers in the honeycomb network. Among the different chemical elements, nitrogen is one of the most promising, being predicted to improve graphene performances, for example as efficient metal-free electrocatalyst for oxygen reduction in fuel cells. However, the production of nitrogen-doped graphene is not trivial. Several approaches were reported in literature which, however, many times do not result in scalable, reproducible and high-quality graphene layers.

In the first part of this thesis, we present an alternative and highly reproducible growth method, based on a controlled preparation procedure, which ensures the formation of nitrogen-doped graphene layers of high morphological quality, and potentially easily scalable, from small samples prepared under ultra-high vacuum (UHV) conditions to large foils produced in industrial lines. In order to develop this alternative growth protocol, we exploited a Ni substrate, since this is a low-cost and widely available metal. Its high catalytic activity is particularly suitable for production of high-quality graphene layers *via* standard chemical vapor deposition (CVD) which, combined with its capability to dissolve/segregate nitrogen into the bulk/surface, allows to easily obtain nitrogen doped graphene sheets. Morphological and chemical characterization by STM and XPS demonstrates that the process yields a flat, wide, continuous nitrogen-doped graphene layer. Experimental results are complemented by a Density Functional Theory (DFT) investigation of possible structural models, to obtain a clear description at the atomic scale of the various configurations of the nitrogen atoms observed in the graphene mesh. This joint approach allowed unveiling the structural, morphological and chemical properties of N dopants trapped in the network. Two are the main configurations observed: graphitic N defects, where a nitrogen atom substitutes a carbon atom in the mesh and bonds to three neighbouring carbon atoms, and 3N pyridinic defects, where three nitrogen are placed at the edge of a carbon vacancy and each of them bonds to two carbon atoms as part of a six-membered ring.

The second part of this PhD thesis is dedicated to the investigation of the reactivity of N-doped graphene on Ni in comparison to pristine graphene. In particular, we focus on the reactivity towards carbon monoxide (CO), one of the simplest molecules in nature, often used as a model. However, being also potentially dangerous and lethal, it is important to rapidly detect and efficiently store it. We confirmed that, in the near-ambient pressure regime and at room temperature, CO interacts with pristine graphene on Ni, intercalating at the interface and detaching the graphene layer from the Ni substrate. We demonstrated that the same behavior occurs for nitrogen doped graphene exposed to CO, but at a pressure one order of magnitude lower with respect to the pristine case, thus pointing out an enhancement of the reactivity of the layer in presence of nitrogen dopants. By means of LEED, XPS and STM measurements, we present a full chemical and morphological characterization of the pristine and nitrogen doped graphene surfaces after CO exposure, point-

ing out similarities and differences between the two layers. In the nitrogen doped case, an in-depth STM morphological characterization combined with a thorough DFT investigation allowed us to identify N dopants in graphitic and pyridinic configurations even after CO exposure.

We finally rationalize the intercalation mechanism itself, which is not trivial for impermeable materials like graphene. By means of a combined experimental (STM, XPS, and LEED) and theoretical (DFT) study, we described how CO molecules succeed in permeating the graphene layer and get into the confined zone between graphene and the Ni surface. Suitably large defects allow CO reaching the interface and the presence of nitrogen dopants at their edges is found to facilitate the permeation process, reducing the CO threshold pressure by more than one order of magnitude. This enhancement in the reactivity towards CO is ascribed to the stabilization of multiatomic vacancy defects by pyridinic nitrogen atoms, opening in this way the doors for CO to the bidimensional nanospace at the interface between graphene and Ni.

Summarizing the results presented and discussed in this PhD thesis, we finally conclude that the new and alternative nitrogen-doped graphene growth method we developed is potentially scalable and suitable for the production of high-performance nano-devices with well-defined nitrogen centers, strongly reactive to CO molecules, with crucial implications for catalysis under cover and graphene-based gas sensors and storage devices.

Sommario

Il lavoro di ricerca presentato in questa tesi di dottorato si inserisce nell'ambito sperimentale dello studio di base per sistemi di immagazzinamento e sensoristica di gas e processi di catalisi "under-cover". In particolare, la ricerca di seguito presentata si focalizza sulla caratterizzazione della crescita, struttura e reattività al monossido di carbonio di grafene e grafene dopato azoto su un substrato di Ni(111), principalmente attraverso le tecniche di microscopia a scansione tunnel (STM) e spettroscopia di fotoemissione a raggi X (XPS), supportate da misure di diffrazione di elettroni a bassa energia (LEED). I risultati sperimentali ottenuti sono stati confermati da calcoli teorici in collaborazione con l'Università Milano-Bicocca (gruppo della Prof. Cristiana di Valentin) e l'Università di Trieste (gruppo della Prof. Maria Peressi).

Attualmente, il grafene è un materiale ampiamente studiato per una gamma molto vasta di applicazioni e le sue proprietà, già molto attraenti, possono essere modificate e, a volte, migliorate attraverso l'introduzione di centri di doping nel suo tipico reticolo a nido d'ape. Tra i vari elementi chimici, l'azoto è uno tra i più promettenti, in quanto è predetto essere in grado di migliorare le prestazioni del grafene, per esempio in modo efficiente come catalizzatore della reazione di ossidoriduzione nelle celle a combustibile. Ottenere grafene dopato azoto non è affatto semplice. In letteratura sono riportati vari metodi di crescita i quali, tuttavia, a volte producono fogli di grafene dopato di bassa qualità, non riproducibili e modulari.

Nella prima parte di questa tesi, presentiamo un metodo alternativo di crescita del grafene dopato con azoto riproducibile e pulito, basato su una procedura di preparazione controllata, che assicura la formazione di strati di grafene dopato di alta qualità morfologica, e potenzialmente facilmente estendibile da piccoli campioni preparati in condizioni di ultra-alto vuoto (UHV) a grandi fogli ottenuti nella produzione industriale. Per poter sviluppare tale protocollo di crescita, abbiamo utilizzato un substrato di Nickel, metallo largamente disponibile ed a basso costo. La sua alta attività catalitica è particolarmente adatta alla produzione di grafene di alta qualità attraverso la tecnica standard di deposizione chimica da vapore (CVD) la quale, combinata con l'alta capacità del Ni di disciogliere e segregare azoto dentro il volume e sulla superficie, permette di ottenere facilmente fogli di grafene dopato azoto. La caratterizzazione morfologica e chimica attraverso STM e XPS dimostra che il processo di crescita produce fogli di grafene dopato azoto piatti, continui e larghi. I risultati sperimentali sono stati completati da uno studio di teoria del funzionale della densità (Density Functional Theory, DFT) relativo ai possibili modelli strutturali, volto ad ottenere una chiara descrizione su scala atomica delle varie configurazioni degli atomi di azoto osservati nella maglia del grafene. Questo approccio combinato ha permesso di svelare le proprietà strutturali, morfologiche e chimiche dei dopanti di azoto intrappolati nella rete del grafene. Le principali configurazioni osservate sono due: difetti di azoto grafiteo, dove un atomo di azoto sostituisce un atomo di carbonio nella maglia e si lega a tre atomi di carbonio vicini, e difetti $3N$ piridinici, dove tre atomi di azoto si trovano al bordo di una vacanza di carbonio e ciascuno di essi si lega a due atomi di carbonio a formare un anello a sei atomi.

La seconda parte di questa tesi di dottorato è dedicata allo studio della reattività del grafene dopato azoto su Ni confrontato con il grafene non dopato. In particolare, ci siamo focalizzati sulla reattività al monossido di carbonio (CO), una delle molecole più semplici in natura, spesso usata come modello. Tuttavia, essendo anche potenzialmente dannosa e letale, è importante riuscire a rivelarla velocemente e immagazzinarla in modo efficiente. In condizioni di pressione quasi ambiente ed a temperatura ambiente, abbiamo confer-

mato che le molecole di CO interagiscono con il grafene su Ni, raggiungendo l'interfaccia tra Ni e grafene e staccando quest'ultimo dal substrato. Tale processo viene definito intercalazione. Abbiamo inoltre dimostrato che lo stesso effetto è stato osservato per il grafene dopato azoto esposto a CO, ma ad una pressione un ordine di grandezza minore rispetto al grafene non dopato, evidenziando così un aumento della reattività del grafene in presenza di dopanti azoto. Attraverso misure LEED, XPS e STM, presentiamo una completa caratterizzazione morfologica e chimica delle superfici di grafene non dopato e dopato in seguito all'esposizione al gas di CO, andando ad evidenziare similitudini e differenze tra i due sistemi. Nel caso del grafene dopato azoto, una meticolosa indagine STM combinata con un approfondito studio DFT ci ha permesso di identificare i dopanti azoto in configurazione grafite e piridinica anche dopo l'esposizione a CO.

Abbiamo infine studiato il meccanismo di intercalazione in sé, il quale non è affatto banale per materiali impermeabili come il grafene. Attraverso la combinazione di uno studio sperimentale (STM, XPS e LEED) e teorico (DFT), abbiamo descritto come le molecole di CO riescono a permeare lo strato di grafene, arrivando così nella zona confinata tra grafene e Ni. Difetti sufficientemente larghi permettono al CO di raggiungere l'interfaccia ed il processo di permeazione è ritenuto essere facilitato dalla presenza dell'azoto a decorare i bordi dei tali difetti, riducendo così la pressione di soglia del CO di oltre un ordine di grandezza, come riportato sopra. Tale aumento della reattività verso il CO viene dunque da noi attribuito alla stabilizzazione di vacanze multiatomiche attraverso atomi di azoto piridinici ai bordi, i quali aprono le porte al CO verso l'interfaccia tra grafene e Ni.

Combinando i risultati presentati e discussi in questa tesi, possiamo concludere che è stato mostrato un metodo nuovo ed alternativo di crescita del grafene dopato azoto, riproducibile e potenzialmente modulare. Tale metodo è adatto alla produzione di nanodispositivi con centri di azoto ben definiti risultanti in alte prestazioni, fortemente reattivi alle molecole di CO e perciò con implicazioni cruciali in processi catalitici "under-cover" e dispositivi basati sul grafene per la sensoristica e l'immagazzinamento dei gas.

Contents

1	Introduction	1
2	State of the Art	5
2.1	Graphene	5
2.2	Production Methods	7
2.2.1	Top-down approach	8
2.2.2	Bottom-up approach	9
2.3	Doped graphene	11
2.3.1	N-doped Graphene	11
2.3.2	Synthesis of N-doped Graphene	12
2.4	Gas-Graphene interaction: pristine vs. N-doped Graphene	13
2.5	Pristine and Nitrogen-doped Graphene on Ni(111)	15
2.5.1	Pristine Graphene on Ni(111)	15
2.5.2	N-doped Graphene on Ni(111)	19
2.5.3	Pristine and N-doped Graphene on Ni(111): CO reactivity	21
3	Experimental Methods	23
3.1	Why Ultra High Vacuum (UHV)	23
3.2	Scanning Tunneling Microscopy	23
3.2.1	STM Theory	24
3.2.2	Scanning Tunneling Spectroscopy	26
3.2.3	STM setup	27
3.3	Photoemission Spectroscopy	30
3.3.1	PES: fundamental basis	30
3.3.2	PES setup	32
3.3.3	PES analysis	34
3.4	Low-Energy Electron Diffraction	36
3.4.1	LEED geometrical theory	36
3.4.2	LEED instrumental setup	38
4	N-doped Graphene on Ni(111)	41
4.1	Growth	41
4.2	N-doped Graphene: epitaxial domains	45
4.2.1	Most abundant N defects	50
4.2.2	Rare N defects	57
4.3	N-doped Graphene: rotated domains	59
4.4	Other models for N defects	60
4.5	N-doped Graphene on Ni nitride	62

5	Reactivity	65
5.1	CO on pristine Graphene on Ni(111)	65
5.1.1	CO intercalation at the Graphene/Ni(111) interface	65
5.2	CO on N-doped Graphene on Ni(111)	72
5.2.1	CO intercalation at the N-doped Graphene/Ni(111) interface	73
5.3	CO intercalation mechanism	78
5.3.1	Pristine Graphene/Ni(111)	78
5.3.2	N-doped Graphene/Ni(111)	80
6	Conclusions	83
A	DFT calculation details	87
	Bibliography	89

Chapter 1

Introduction

Graphene was the first 2D material to be isolated and characterized in 2004 by Novoselov and Geim [1]. One-atom thick, a graphene layer is formed by sp^2 -hybridized carbon atoms, arranged in a honeycomb lattice. This structure is responsible for its peculiar properties: high electrical and thermal conductivity, charge mobility, transparency and flexibility are some of the unique characteristics, successfully exploited in several research fields, such as optics and photonics [2, 3, 4], biomedical applications [5], gas storage [6] and many others. Nevertheless, the practical use of graphene has some limitations: for example, it is a zero band gap semiconductor, which makes it not directly exploitable in electronic devices, and it is nearly inert to several gases [7], thus limiting its use in sensing applications or for efficient gas storage/release purposes. Therefore, the challenge is to find new strategies to overcome these issues and to fully exploit its potentiality.

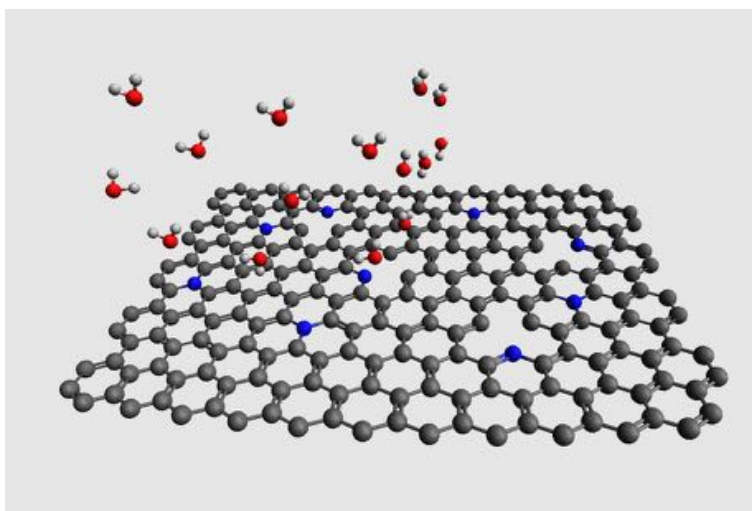


Figure 1.1: N-doped graphene exposed to a gas.

Recently, doping of graphene has been claimed to be a promising approach in order to tune and enhance its properties: for example, opening a gap and turning graphene into a semiconductor material suitable for electronic applications [8], or enhancing the gravimetric density for hydrogen storage applications [9], or resulting in a higher electrical conductivity [10], improving its electrocatalytic activity towards oxygen reduction reaction (ORR) [11, 12] and its potential for energy storage [13, 14, 15]. In particular, nitrogen-doped graphene is predicted to be a promising 2D material for sev-

eral applications, including gas sensing and gas storage [16, 17, 18].

Therefore, in the last years, especially after the growing environmental concerns and the increasing interest in clean catalytic processes for industrial applications, pristine and doped graphene supported on several metal substrates has been investigated in interaction with specific gases, for sensing applications or as part of nano-reactor devices for catalysis under cover.

To this purpose, significant experimental and theoretical efforts have been devoted to the investigation of pristine graphene interacting with simple and very common gases, among which oxygen (O_2) [19, 20], hydrogen (H_2) [21, 22], carbon monoxide (CO) [23, 24] and carbon dioxide (CO_2) [22]. However, although it plays a key role, for example, in the CO oxidation under-cover, pristine graphene results nearly inert to toxic and potentially lethal gases like nitrogen monoxide (NO) and CO itself [7], thus highlighting the necessity to tune its properties, *e.g.* through doping with nitrogen atoms.

However, the production of nitrogen-doped graphene is not trivial. In literature, several methods have been proposed, which can be summarized into two approaches: (i) direct synthesis of the doped layer, where nitrogen atoms are introduced during the graphene formation. This is the case of the chemical vapor deposition (CVD) method, where a catalytic substrate is exposed to N- and C-containing precursors, resulting in the formation of a high-quality doped graphene layer [25, 26, 27]; (ii) post-synthesis approach, where N dopants are introduced in the already grown graphene network. In this case, graphene is typically exposed to a nitrogen plasma bombardment, which promotes the replacement of some C atoms with N atoms [28, 29]. However, both these approaches have some drawbacks: in the first case, the high pressure and temperature required for the growth process, the specific equipment and the dangerous precursors needed, make the production troublesome and pose serious safety issues. On the other hand, in the post-synthesis approach, the quality of the layer is drastically reduced, due to the formation of large defects caused by the N bombardment.

The aim of this work is to investigate the reactivity of graphene, comparing its pristine phase with the doped system, in particular nitrogen-doped graphene. In order to reach this goal, a good quality of the nitrogen-doped graphene layer and the control of the N doping process are mandatory, requiring an optimization of the nitrogen-doped graphene growth process.

In order to do this, we propose a new growth approach to obtain high-quality nitrogen-doped graphene on a Ni(111) single crystal. This method, alternative to those already reported in literature, combines the chemical vapor deposition technique, using a C-containing precursor, with the segregation process of nitrogen from the Ni bulk. The Ni substrate was chosen for its catalytic properties, wide availability and for the relatively low temperature required to crack and dehydrogenate hydrocarbon molecules on its surface, making it one of the most commonly and widely used substrates in industry and research. We demonstrated that the resulting graphene layer is doped by nitrogen atoms, while keeping the high morphological quality of the layer. Moreover, due to the relatively low temperature and pressure required for this procedure, the experimental conditions adopted are fully compatible with a growth process in ultra-high vacuum (UHV), thus allowing an *in situ* characterization of the layer by means of experimental techniques that require a UHV environment.

Regarding the reactivity studies we performed, significant efforts were focused on the investigation of the interaction between gases and graphene (both pristine and nitrogen-doped system), trying to unveil the role of N dopants in the process. To this aim, in particular, we exposed the nitrogen-doped layer to carbon monoxide and we compared the

experimental results with those obtained for the pristine graphene layer on Ni(111).

Surface sensitive techniques, such as Low-Energy Electron Diffraction (LEED) and Scanning Tunneling Microscopy (STM), the latter both at room and cryogenic temperature, were used in order to characterize the nitrogen-doped graphene systems from long-range order to atomic-scale resolution. Moreover, X-ray Photoelectron Spectroscopy (XPS) provided information about the chemical composition of the sample, confirming the presence of nitrogen on the surface and giving preliminary hints of its coordination in the network. The same experimental techniques were exploited to investigate the modifications induced by the interactions with gases, from a morphological and chemical point of view. Finally, Density Functional Theory (DFT) calculations and STM simulated images allowed an in-depth understanding of the nitrogen-doped system, leading to the identification of different structural configurations of nitrogen in the graphene mesh and the interaction between the gas used and the doped graphene layer.

In chapter 2, an overview about the state of the art on graphene, its properties and its production methods is reported. A specific section is dedicated to the doping of graphene and, in particular, to nitrogen-doped graphene. Finally, in the last section, experimental and theoretical results reported in literature about the reactivity of the pristine and doped system are compared.

In chapter 3, a brief introduction to the experimental techniques used to perform this thesis will be provided, reporting the fundamental working principles and the description of the experimental setup, as well as a brief summary of the literature results on the pristine graphene growth on Ni(111), used as starting point to develop and optimize the alternative nitrogen-doped graphene growth process.

The experimental results about the growth and characterization of nitrogen-doped graphene will be presented and discussed in chapter 4. In the first section, the new growth process proposed to obtain high-quality nitrogen-doped graphene on Ni(111) will be described in detail. Then, by means of STM and XPS, the as grown nitrogen-doped layer will be characterized from a morphological and chemical point of view. DFT calculations and STM simulated images will be presented, in order to corroborate the experimental results, which will be compared with the pristine case, in order to highlight the differences among the two systems.

In chapter 5, the experimental results regarding the reactivity of the pristine and nitrogen-doped graphene will be compared, identifying the morphological differences and unraveling the crucial aspects of the interaction between the gas and the graphene layers.

Finally, in chapter 6, we will report the conclusions of this work and the perspectives for future investigations and possible technological applications.

Most of the work reported in this thesis was performed at the CNR-IOM in Trieste. The STM measurements were performed in the STRAS laboratory (Surface sTructure and Reactivity at the Atomic Scale), while XPS measurements were performed partially at the INSPECT laboratory (IN-situ Synthesis and PhotoEmission CharacTerization) of Dr. Cinzia Cepek, and at the ALOISA beamline [30], at Elettra Sincrotrone Trieste. DFT calculations were performed by the group of Prof. Cristiana di Valentin at the University of Milano-Bicocca and the group of Prof. Maria Peressi at the University of Trieste.

Chapter 2

State of the Art

2.1 Graphene

Graphene is formed by carbon atoms arranged in a 2D crystalline structure and can also be considered as the building block for other sp^2 carbon-based materials. Indeed, when it forms a sphere, it becomes a 0D fullerene, if it is rolled up, it becomes a 1D nanotube, and when several graphene layers are stacked (more than 20-30 layers), it assumes a 3D crystalline form, becoming graphite [31] (see Figure 2.1).

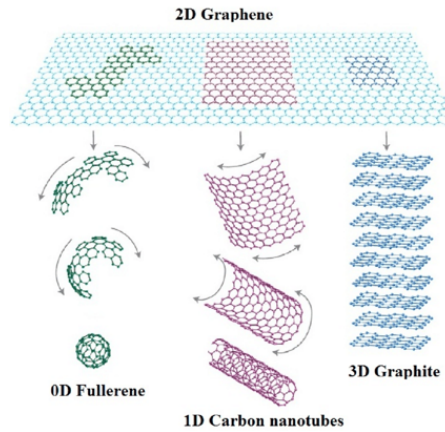


Figure 2.1: Graphene is the 2D building material for all other dimensionalities carbon materials: fullerenes (0D), carbon nanotubes (1D) and graphite (3D). From ref. [31]

In graphene, carbon atoms are arranged in a one-atom thick planar honeycomb mesh, formed by two equivalent triangular sublattices, as sketched in Figure 2.2a.

The graphene unit cell consists of two carbon atoms, one for each triangular sublattice, separated by 1.42 \AA . The primitive vectors of its unit cell are:

$$\mathbf{a}_1 = \frac{a}{2}(1, \sqrt{3}), \quad \mathbf{a}_2 = \frac{a}{2}(1, -\sqrt{3})$$

where $a = |\mathbf{a}_{1,2}| = 2.46 \text{ \AA}$ is the graphene lattice parameter. Its reciprocal lattice vectors are expressed as:

$$\mathbf{b}_1 = \frac{2\pi}{3a}(3, \sqrt{3}), \quad \mathbf{b}_2 = \frac{2\pi}{3a}(3, -\sqrt{3})$$

where $b = |\mathbf{b}_{1,2}| = 4\pi/\sqrt{3}a = 2.95 \text{ \AA}^{-1}$.

In the momentum space, the K points of the Brillouin zone are:

$$\mathbf{K} = \frac{2\pi}{3a}(\sqrt{3}, 1), \quad \mathbf{K}' = \frac{2\pi}{3a}(\sqrt{3}, -1)$$

The electrons in graphene can be described by the tight-binding model through the following Hamiltonian:

$$H = -t \sum_{\langle i,j \rangle, \sigma} (a_{\sigma,i}^\dagger b_{\sigma,j} + H.c.) - t' \sum_{\langle\langle i,j \rangle\rangle, \sigma} (a_{\sigma,i}^\dagger a_{\sigma,j} + b_{\sigma,i}^\dagger b_{\sigma,j} + H.c.)$$

where t ($\sim 2.8 \text{ eV}$) and t' ($\sim 0.1 \text{ eV}$) are the nearest-neighbour and next nearest-neighbour hopping parameters, respectively, while $a_{\sigma,i}$ and $a_{\sigma,i}^\dagger$ are the annihilation and creation operators, respectively, of an electron with spin σ ($\sigma = \uparrow, \downarrow$) on site \mathbf{R}_i on sublattice A (similarly for sublattice B). The energy bands derived from the Hamiltonian are [34]:

$$E_{\pm}(\mathbf{k}) = \pm t \sqrt{3 + f(\mathbf{k})} - t' f(\mathbf{k})$$

$$f(\mathbf{k}) = 2 \cos(\sqrt{3}k_y a) + 4 \cos\left(\frac{\sqrt{3}}{2}k_y a\right) \cos\left(\frac{3}{2}k_x a\right)$$

where the plus and minus signs are relative to the dispersion surface of π^* and π bands, respectively. This dispersion can be approximated by expanding in Taylor series the band structure, close to the Brillouin zone points K and K', given $\mathbf{k} = \mathbf{K} + \mathbf{q}$, with $|\mathbf{q}| \ll \mathbf{K}$, and resulting in:

$$E(\mathbf{q}) = \pm \hbar v_F |\mathbf{q}| + O[(q/K)^2]$$

where $v_F = \sqrt{3}ta/(2\hbar) \approx 10^6 \text{ ms}^{-1}$ is called the Fermi velocity of the electrons in graphene. Since the bands display a linear k dependence at the corners of the Brillouin zone in the reciprocal space (see Figure 2.2b), electrons in graphene behave as massless particles, called Dirac fermions. In the energy-momentum space, these bands assume a cone shape, the so-called *Dirac cones*, touching in one point, known as the *Dirac point*.

The bands structure of graphene was calculated by P. R. Wallace in 1947 [35]. Each carbon atom of the graphene network has s , p_x and p_y orbitals and is bound to three neighbouring carbon atoms of the mesh, forming an sp^2 -hybridized layer. The p_z orbitals of each carbon atom overlap, giving rise to the filled π and the empty π^* states, which form the

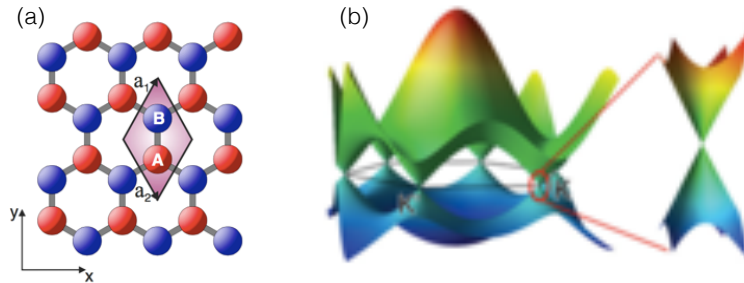


Figure 2.2: (a) Schematic representation of the graphene lattice formed by two indistinguishable sublattices, marked by two different colors and labeled A (red) and B (blue), respectively. \mathbf{a}_1 and \mathbf{a}_2 are the unit cell vectors ($|\mathbf{a}_{1,2}| = 2.46 \text{ \AA}$) [32]. (b) Band structure of graphene with a linear dispersion around K and K' points. On the right side, a magnification of the Dirac cones touching at the Dirac point [33].

valence and conduction bands in graphene, respectively. In the ideal condition of isolated and undoped graphene, the Fermi level coincides with the Dirac point, the point where the completely filled π states touch the completely empty π^* states.

Due to its peculiar electronic behavior, graphene has several fascinating properties, widely studied and applied in different fields.

In 2004, for the first time, Novoselov and Geim experimentally obtained graphene in the form of small flakes of the order of several microns by mechanical exfoliation from a single crystal graphite using scotch tape, and they demonstrated that the electronic states of graphene can be tuned by an electric field [1]. One year later, graphene was demonstrated to be an ideal 2D electron gas system after the measurement of the quantum Hall effect [36]. Moreover, such new 2D material shows other peculiar properties, such as an extremely high electron mobility at room temperature ($2 \times 10^5 \text{ cm}^2 \text{V}^{-1} \text{s}^{-1}$) [37], a Young's modulus of 1 TPa and intrinsic strength of 130 GPa [38], a very high thermal conductivity (above 3000 WmK^{-1}) [39], optical absorption of $\approx 2.3\%$ in the infrared limit [40], a large specific surface area ($2630 \text{ m}^2/\text{g}$).

However, graphene suffers from some severe limitations. For example, since its band structure at the Fermi level is formed by two Dirac cones touching at the Dirac point, thus without a measurable bandgap, graphene is often called zero-gap semiconductor. The lack of a bandgap poses a serious issue to its use in electronics, since switching off any graphene-based device would be virtually impossible. Additionally, it has been widely demonstrated that the substrate on which graphene is grown or just supported can induce dramatic effects on its transport properties.

How to bypass these and other issues is nowadays one of the most investigated topics by a large part of the scientific community. Three are the main routes followed: (i) optimizing the graphene growth process and make it suitable for a specific application, (ii) nanostructuring graphene to open a bandgap through quantum confinement and (iii) functionalizing graphene with heteroatoms, in order to improve and enhance its properties and tune its behavior.

2.2 Production Methods

Graphene can not be effectively used in any application without specific techniques aimed to synthesize high-quality and large-area graphene in a cost-effective way, as shown in Figure 2.3.

Synthesis of graphene refers to any process for production of graphene. The specific method chosen for its preparation depends on the desired size and purity of the final product. In the last decade, several techniques were established in order to synthesize graphene, following two main pathways: (i) the top-down approach, which focuses on breaking "graphene precursors" as graphite into single layers of carbon atoms, and (ii) the bottom-up synthesis, where carbon atoms are involved as building blocks in graphene formation. Examples of the top-down approach are the commonly used techniques of *mechanical* and *chemical exfoliation*, while bottom-up methods are *epitaxial growth on SiC*, *molecular self-assembly* and *chemical vapor deposition*. These techniques will be briefly described in the following sections.

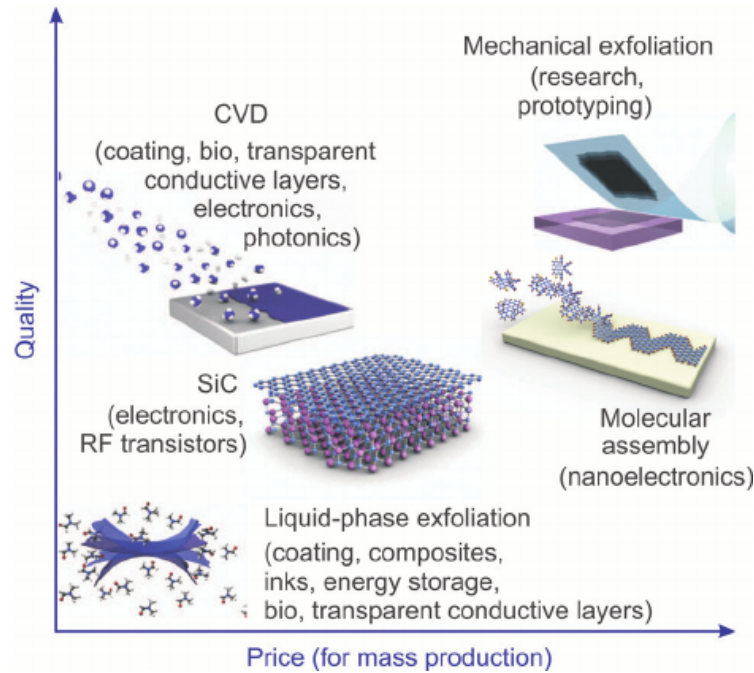


Figure 2.3: Methods of mass-production of graphene, considering the price (for mass production) as a function of the quality and size. From ref. [41].

2.2.1 Top-down approach

Mechanical Exfoliation

In 2004, for the first time, Novoselov and Geim produced small flakes of graphene by mechanical exfoliation of graphite [1]. With this technique, a longitudinal or transverse stress is applied on the surface of a layered material, in this case graphite. Since the latter is a stack of several graphene layers, separated by 3.34 \AA and bounded by weak van der Waals forces (2 eV/nm^2), an external force of $\sim 300 \text{ nN}/\mu\text{m}^2$ is required to separate one-atom thick layers from the graphite crystal. Through mechanical exfoliation from graphitic materials, different thickness of layered graphene sheets can be obtained, using a variety of agents like scotch tape [1], ultrasonication [42] or electric field [43]. As confirmed by optical microscopy, atomic force microscopy and Raman spectroscopy [44], the quality of graphene produced with this method is usually high, with almost no defects but as drawbacks the flakes are small and the number of final layers cannot be controlled and the production cost is high. Graphene obtained by this method is mostly used for production of field-effect transistor (FET) devices.

Chemical Exfoliation

Chemical exfoliation allows to obtain graphene from graphite in a two-step process: first, by intercalating small molecules, the interlayer van der Waals forces are reduced and the interlayer spacing increased, forming in this way graphene-intercalated compounds (GICs). Then, the exfoliation of single or few graphene layers is obtained by rapid heating or sonication. A similar approach can be exploited using graphene oxide, first involving the oxidation of graphite with strong oxidizing agents and then by its ultrasonic exfoliation in aqueous solution [45]. After centrifugation treatment, the final product can be de-

posited on thin films or surfaces and partially reduced. Thermal exfoliation and reduction of graphene oxide produces a slightly lower-quality graphene, with respect to mechanical exfoliation, but has also a lower production cost, as shown in Figure 2.3.

2.2.2 Bottom-up approach

Epitaxial Growth on SiC

"Epitaxy" derives from the Greek: "epi" means *over* and "taxis" means *order* or *arrangement*. Thus, a single crystalline film deposited on a single crystalline substrate produces epitaxial layer, *via* a process called epitaxial growth.

Epitaxial thermal growth of graphene on a single crystalline silicon carbide (SiC) wafer is a widely used method for graphene synthesis, resulting in homogeneous, flat and defect-free graphene layers.

Graphene growth on SiC occurs *via* the thermal decomposition of SiC. Indeed, upon annealing, only the silicon atoms leave the surface by sublimation, due to the difference in the vapor pressures of silicon and carbon, and the remaining carbon atoms rearrange on the surface forming a first C-rich $6\sqrt{3} \times 6\sqrt{3}R30^\circ$ layer, called *buffer layer*. Then, iterating the process, the buffer layer is detached from the substrate by a new buffer layer, transforming the previous one in an epitaxial monolayer graphene [46]. The heat treatment of SiC, in the temperature range of 1000-1500 °C in UHV conditions or in Ar atmosphere, allows graphene to grow on both of the SiC polar faces, with growth rate depending on the specific polar plane [47]. Indeed, on the C-terminated face, larger domains of multi-layered and rotationally disordered graphene are obtained, while the Si-terminated face allows control on the number and order of the graphene layers, in smaller domains with respect to the C-face.

Epitaxial graphene growth on SiC is a very promising method for large scale production of graphene, in particular for applications in electronics. However, some not negligible drawbacks of this method are the high cost of the SiC wafers and the high temperature required for the process.

Molecular self-assembly

Molecular self-assembly is the process by which molecules organize into structurally well-defined aggregates driven by the interplay of intermolecular and molecule-substrate interactions [48].

When the process involves also chemical reactions leading to the breaking/formations of chemical bonds, molecular self-assembly can be exploited as a synthesis strategy which is usually referred to as "on-surface synthesis". This approach is based on the careful design of suitable molecular precursors with specific shape and chemical composition to promote a stepwise reaction on a particular metal surface. This bottom-up chemical synthesis allows achieving for example atomically precise graphene nanoribbons (GNRs) [49], nanometer-wide graphene strips into which the structural confinement allow to open a band gap. In the surface-assisted synthesis of GNRs, homolytic carbon-halogen cleavage is thermally induced, and the resulting diradicals undergo polymerization (the so-called Ulmann coupling) to form linear polymers on a metal surface, typically Au(111). Subsequent annealing of the polymers at higher temperatures results in the formation of GNRs through surface-assisted intramolecular cyclodehydrogenation [50].

The on-surface synthesis was initially exclusively carried out under UHV conditions with pressures lower than $\approx 10^{-9}$ mbar. Recent progress made by employing less-demanding high vacuum (HV) [51] as well as lower vacuum and even ambient pressure conditions,

using an industry-viable chemical vapor deposition (CVD) setup [52], has led to the successful on-surface synthesis of GNRs with the same structures as those synthesized under UHV.

By using such direct surface reactions, it is possible to grow also two-dimensional supramolecular networks [49, 53, 54] as well as 2D nanoporous graphene by laterally fusing GNRs [55], which are of great interest for nanopatterning, organic electronics, nano-reactors, and immobilization of functional molecules in size matched pores, and for energy and gas storage.

This growth method has a relatively low cost, is versatile and results in stable and robust structures, even if it is usually strongly dependent on the substrate.

Chemical Vapor Deposition

Chemical vapor deposition (CVD) is a bottom-up approach in which carbon-containing precursors (like hydrocarbon molecules) are catalytically decomposed on the substrate surface and C atoms rearrange to form a graphene layer. In the recent years, the production of high-quality graphene by CVD was successfully demonstrated on several catalytic transition-metal substrates, such as Ni [56], Cu [57], Ir [58], Ru [59].

Depending on the level of carbon solubility in the metal, the CVD growth process can occur in two different ways:

(i) *Bulk-mediated growth* occurs when the solubility of carbon in the catalyst substrate is high. Indeed, C atoms resulting from hydrocarbons decomposition diffuse on the surface and dissolve into the bulk. When a C supersaturation level is reached, they segregate on the surface, resulting in graphene islands nucleation and growth. This often happens during graphene growth on Ni, Co, Pt and Ru [56, 60, 61, 62].

(ii) *Surface growth* occurs when hydrocarbon molecules dissociate on a catalytic surface and C atoms remain on it, without dissolving into the bulk. Then, C atoms aggregate and rearrange forming graphene domains. This is the case of Cu and Ir.

Among all the variety of catalysts previously cited, copper and nickel are the most popular metal substrates for CVD graphene growth, due to their availability and the possibility to synthesize high-quality graphene, even if they adopt distinct synthesis mechanisms due to their different affinities to carbon. Cu has been proposed as the best candidate for industrial exploitation of CVD graphene production, but the high temperatures (~ 1000 °C) required to completely dehydrogenate the C-containing precursors, are close to the Cu sublimation temperature, with the possibility of a consequent poisoning of the working environment. On the other hand, Ni, due to its high catalytic activity, allows graphene growth at temperature below 600 °C [56] representing a considerable improvement in terms of energy cost and avoiding contamination problems.

Due to its availability, Ni is one of the most widely used catalytic substrates in industry and research. As single crystal, as well as polycrystalline substrate, it has been investigated in-depth and, in particular, its (111) crystallographic surface has been often used as model system for graphene growth [63, 64]. Indeed, since the lattice mismatch between Ni(111) and graphene is less than 1% ($a_{Ni}=2.49$ Å, while $a_{Gr}=2.46$ Å), high-quality, homogenous and flat graphene layers can easily form on this substrate by CVD growth. Moreover, recently a combined experimental and theoretical study demonstrated the key role played by Ni surface atoms during the graphitization process [65]. This confirms that the substrate is not just a graphene support which influences its transport properties once formed, but it strongly affects the graphene growth process itself.

Finally, it is worth noting that the interaction at the interface between graphene and Ni is relatively strong compared to other substrates [66], leading to important changes in

graphene properties [67].

2.3 Doped graphene

Graphene has many interesting and peculiar properties suggesting a potential use in several scientific and technological fields. Nevertheless, there are various limitations to be overcome: (i) it is a zero-bandgap semiconductor, which prevents its direct implementation in electronic devices; (ii) when it is accommodated on a metal substrate, it loses almost totally its high charge mobility; (iii) it results nearly inert when exposed to several gases despite its large surface area.

In order to bypass these constraints, new strategies to adapt graphene to the variety of potential applications came up over time. Doping of graphene, by its combination with other chemical species, is nowadays a promising approach in order to modify its electronic structure and to successfully tune its properties. For example, theoretical calculations reported that the introduction of lithium atoms in a graphene layer opens a gap [8], thus turning it into a semiconductor material suitable for electronic applications; titanium-doped graphene has been demonstrated to enhance the gravimetric density for hydrogen storage applications [9], while boron- or nitrogen-doped graphene results in a higher electrical conductivity [10], adding holes or electrons to the system, respectively. Moreover, B and N are demonstrated to enhance the graphene electrocatalytic activity towards the oxygen reduction reaction (ORR) [11, 12] and raise its potential as energy storage material [13, 14, 15]. In particular, nitrogen-doped graphene is claimed to be a promising 2D material for several applications, such as gas sensing and gas storage, due to its high potential sensitivity and selectivity to several gases [16, 17, 18].

2.3.1 N-doped Graphene

Nitrogen (N) is a natural candidate for graphene doping, due to its atomic size (similar to that of C) and its electron donor character in substitutional doping. A theoretical work reported substitutional doping as an efficient method to open a bandgap in graphene: the linear dispersion of the electronic bands within 1 eV from the Fermi energy is not affected by the N doping but a bandgap is opened and the Fermi level shifted into the conduction band, leading to a *n*-type semiconducting electronic properties (see Figure 2.4a) [10].

In the last years, significant efforts have been focused on the investigation of nitrogen-doped graphene, studying its production process, its resulting structure and its properties, in relation to possible applications. It is often presented and discussed in comparison with boron-doped graphene, due to the similarities between the two dopants (indeed they are the neighboring atoms of C in the Periodic Table). Having a hole acceptor character, substitutional B atoms behave in the opposite way with respect to N, shifting the graphene Dirac point in the valence band and inducing *p*-type semiconducting electronic properties. From a morphological and structural point of view, N atoms can actually be found in the graphene network in three different configurations, as it is shown schematically in Figure 2.4: (i) graphitic (or substitutional) N, where N atom is substituting a C atom in the graphene network and bonds to three neighboring carbon atoms; (ii) pyridinic N, where N is placed at the edge of a C vacancy and bonds to two C atoms as part of a six-membered ring; (iii) pyrrolic N, where N is bonded to two C atoms by forming a pentagon, typically at the edges of the flake. Among the three different configurations, pyridinic and graphitic N are sp^2 -hybridized while pyrrolic N is sp^3 -hybridized.

Each dopant configuration differently affects the graphene electronic structure: the graphitic

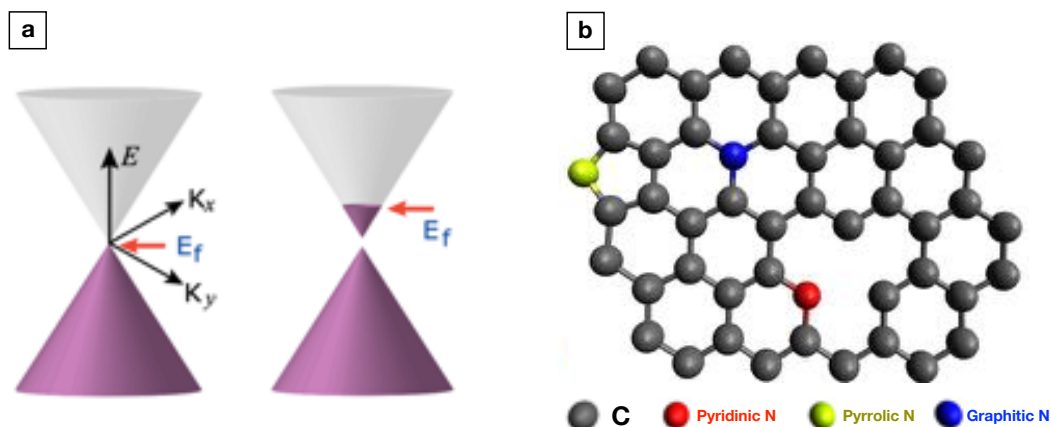


Figure 2.4: (a) Sketch of the band structures of pristine (left) and n -type (right) graphene. From ref. [68]. (b) Schematic representation of the three possible configuration of N defects in graphene: graphitic N (represented in blue), pyridinic N (represented in red) and pyrrolic N (represented in light green)

N configuration, as reported above, brings the Fermi level in the conduction band, leading to a n -type doping, while the pyridinic N structure moves it in the valence band, p -doping the graphene layer.

Therefore, the ability to engineer high-quality N-doped graphene with the desired dopant configuration would allow a precise control over doping levels and device sensitivity and would improve reproducibility.

2.3.2 Synthesis of N-doped Graphene

The production of N-doped graphene is not trivial. In the last years, significant efforts have been devoted to fine tune the doping process, in order to obtain high-quality N-doped graphene layers and to control the amount of doping and its configuration. Two are the main routes followed:

(i) a *direct synthesis* approach is usually adopted when N is introduced during graphene formation. There are several ways to grow N-doped graphene *in situ* and CVD is the widely used technique for growing high-quality layers. In general, a CVD growth involves the flow of N- and C-containing precursors through a furnace on top of a target substrate, heated to a desired temperature. The precursors can be in the gas phase, as in the case of ammonia (NH_3) [25], sublimated from solid phase, such as melamine [69], or in the liquid phase, such as pyridine [70]. Several metallic substrates are used, such as Cu, Ni, and Pt. The choice of all parameters including precursors, temperature, pressure, flow rate and substrate allows controlling the final dopant percentage and bonding configuration. In general, the combination of commonly used gas phase precursors like ammonia and methane, for example, results more likely in the formation of graphitic N defects [25]. Another technique for the direct synthesis of N-doped graphene is the arc-discharge method, in which a high-current is applied between graphite electrodes in NH_3 atmosphere [71]. This approach has many advantages: owing to its metal free production, the effects of metal impurities are ruled out, and since it does not need strict vacuum conditions, it is considered a timesaving production method. N-doped graphene layers obtained with this technique contain mainly pyridinic N configurations.

(ii) a *post growth synthesis*, on the other hand, involves the exposure of pristine graphene

to a bombardment of a chemically active nitrogen source, in order to create defects in the graphene mesh. This goal can be achieved by means of three methods: exposure to ammonia while keeping graphene at elevated temperatures [72], bombardment with ion gun, and exposure to nitrogen-containing plasma.

In the first procedure, the previously grown graphene sheets are kept at high temperature (around 1000 °C) while flowing high pressure of ammonia (around 1 Torr) in a furnace, resulting in the incorporation of N atoms into graphene.

In the second case, the graphene layer is bombarded with either a relatively low energy flux of N₂ gas (around 100 eV), mainly obtaining substitutional N defects [73, 74], or with an higher N₂ energy flux, forming pyridinic N defects in the graphene network.

Finally, graphene can be exposed to a nitrogen containing plasma. This treatment has been demonstrated to be effective for doping graphene [75] and nanotubes [76] with nitrogen. Compared with thermal treatment, plasma treatment can induce a higher concentration of nitrogen atoms.

2.4 Gas-Graphene interaction: pristine vs. N-doped Graphene

Among the variety of possible and promising applications, graphene is considered as a unique and attractive material for gas sensors.

First, graphene is predicted to have a large specific surface area (2630 m²g⁻¹), thus each C atom of the single-layer sheet represents a surface atom, allowing in principle and enhancement of gas molecules adsorption. The interaction that can occur between the C atoms of the graphene network and the gas molecules could vary from a weak van der Waals interaction to a strong covalent bond. This different interaction mainly depends on the composition and structure of the gaseous adsorbate, which can be classified in closed-shell and open-shell impurities. The first one, like water molecules (H₂O), molecular H or noble gas atoms, is almost chemically inert, having a gap between its highest occupied molecular orbitals (HOMO) and its lowest unoccupied molecular orbital (LUMO) generally of the order of $\approx 5 - 10$ eV. On the other hand, an open-shell system has one partially occupied orbital and HOMO and LUMO are separated by a gap of the order of ≈ 1 eV, that may easily induce an hybridization with the graphene bands. Alkali and halogens belong to this second category: they are chemically active and can act as dopants, thus providing electrons or holes to graphene. However, although these molecules bind to graphene as ions, they weakly hybridize with graphene bands.

Covalent bonds with graphene are instead predicted to occur with adsorbates like atomic H, OH radicals or CH₃ groups [77] which, however, are not present in gas phase and need to be produced through chemical reactions before to be adsorbed on graphene.

All these interactions result in a perturbation of the graphene electronic structure, which can be in principle monitored by suitable electronic techniques.

Another remarkable peculiarity of graphene is its high carrier mobility at room temperature (200 000 cm² V⁻¹ s⁻¹), which makes it more conductive than silver and copper, with the lowest resistivity at room temperature (10⁻⁶ Ω) among the substances known so far [78]. Furthermore, due to its high-quality crystal lattice along with its 2D structure, graphene has a low electrical noise, so even a small amount of extra electrons due to gas adsorption, even down to the molecular level, can induce a noticeable change in the graphene conductance.

In a pioneering work published in 2007, Schedin *et al.* used mechanically exfoliated graphene for detecting gases, reporting a high sensitivity down to the detection of individual gas molecules [7]. The authors experimentally demonstrated that the exposure of

graphene to NO_2 and NH_3 induces a stronger change in its resistivity, if compared to other gases such as CO and H_2O .

After the previously cited work, several groups investigated the sensing performance of pristine graphene, both experimentally and theoretically [79, 80, 81], relatively to gases such as NO, NO_2 and CO_2 .

Besides the gas nature, the performance of the graphene-based sensor is strongly dependent on several factors, namely the exposure temperature, the gas flow rate as well as the geometrical parameters of the graphene sheet, such as the length-to-width ratio and the quality in terms of defects. Indeed, it has been experimentally and theoretically demonstrated that defects in graphene, like point defects and linear defects, can enhance its ability to detect gases, showing a stronger interactions with CO, NO or NO_2 , if compared to the non-defective graphene case [18, 82].

Beside the previously cited factors, theoretical calculations demonstrated also the non trivial role of the supporting substrate in the gas-graphene interaction. For example, Ambrosetti *et al.* [17] investigated from first-principles calculations the effect of $\text{Cu}(111)$ and $\text{Ni}(111)$ substrates on defective graphene, revealing that transition-metal substrates can significantly contribute to the local reactivity of the graphene layer to CO.

A plethora of graphene-supporting substrates were then investigated after exposure to CO, in different experimental conditions of temperature and pressure. When the CO pressure is increased up to the millibar regime, intercalation was observed at the interface between the graphene layer and several metal substrates like Ir [83], Ru [84], Pt [85] already at room temperature, similarly to what observed after exposure to oxygen of graphene on Ni but at higher temperature [86]. This peculiar behavior opens a new route for graphene applications in the field of "catalysis under-cover". Indeed, it has been demonstrated that the graphene layer acts as a carpet, confining molecules at the interface with the substrate. Depending on the catalytic properties of the specific substrate, chemical reactions can take place, thus transforming the system in a "nano-reactor" [23].

Another approach that may be crucial for the improvement of the gas-graphene interaction is the embedding of heterospecies in the graphene network. Theoretical and experimental investigations report that doping graphene with atoms such as N, B or Al may improve its sensitivity to molecules and gases.

In the field of molecular sensor applications, the adsorption of Rhodamine B (RhB) molecules, usually very difficult to detect by conventional Raman spectroscopy at low concentrations, has been investigated on a N-doped graphene substrate [26]. The authors were able to anchor this molecules to the surface, thanks to the presence of nitrogen in the graphene network, and to probe the molecules by enhanced Raman scattering, opening the way to new molecular sensing devices.

Similarly, N-doped graphene has been used in order to detect molecules such as tetraphenylporphyrin (H_2TPP) [87]. These molecules were deposited on top of the N-doped graphene layer and, by means of STM/STS, a charge transfer between the N doping site and the molecule was detected, highlighting the potentiality of the N-doped graphene as sensing material in different fields.

On the other hand, in the field of gas sensors, NO_2 and CO have demonstrated to react with N-doped graphene [88, 89], NO, NO_2 and NH_3 with B-doped graphene [90, 91], while Al-doped graphene showed promising performances in CO detection [89, 92].

Recently, particular attention has been focused on N-doped graphene as a promising sensing material. The ability of N-doped graphene to selectively detect CO from air has been theoretically demonstrated [93]. The theoretical calculations indicate that, while graphene vacancies cannot selectively sense CO in air, N-doped graphene shows a high selective sen-

sitivity to this gas. Indeed, CO is predicted to chemisorb on the pyridinic N defects with a concomitant large charge transfer, which could be exploited in CO sensing applications.

2.5 Pristine and Nitrogen-doped Graphene on Ni(111)

2.5.1 Pristine Graphene on Ni(111)

In literature, transition metals have been widely used as substrates for CVD graphene growth, thanks to their catalytic properties.

Due to its availability, low cost (compared to other transition metals like Pt, Pd or Ag) and high catalytic activity, Ni is one of the most widely used substrates for research and industrial applications, varying from bulk single crystals [94, 95, 96], epitaxial Ni on W(110) [97], thin-Ni films on oxide substrates [98] to polycrystalline substrates [95]. In particular, for large industrial graphene production, polycrystals and thin films of Ni are mainly employed. However, for scientific research purposes, Ni single crystals are usually investigated as a fundamental step to be extended for reliable applications.

The thickness of these Ni-films and thus the amount of C that can be dissolved in them may influence the graphene growth [99].

The interaction between the Ni substrate and the graphene layer on top was experimentally investigated by means of several experimental techniques. From a spectroscopic point of view, a downward shift of the Dirac point below the Fermi level combined to a strong hybridization of the Ni 3d bands with the 2p bands of graphene [96, 98], as well as a higher binding energy measured for C atoms of graphene [100], represent all fingerprints of a significant change in the electronic properties of graphene. By combining nonlinear photoemission experiments and DFT calculations, the modification of the Ni(111) surface states induced by the presence of graphene were studied [101]. Graphene was demonstrated to be able to displace the Ni(111) surface states from the valence band close to the Fermi level, thus modifying their k-dispersion and the electrons effective mass. On the other hand, by local tunneling spectroscopy measurements combined with spin-polarized *ab initio* electronic structure calculations, a clear signature of spin- and edge-dependent electron scattering was revealed. It was attributed to the strong distortion of the electronic structure at the interface, where the Ni surface states significantly shift in energy and space due to the confinement induced by the graphene layer, and to the different coupling to bulk states of majority and minority Ni states [102].

Among all the different Ni substrates, Ni(111) single crystal (which is a face-centered cubic crystal) is the most commonly used substrate to investigate graphene growth, due to the hexagonal distribution of the Ni surface atoms and its lattice parameter, $a_{Ni}=2.49$ Å, very close to that of graphene ($a_{Gr}=2.46$ Å), which allows an easier accommodation of the graphene sheet on the Ni(111) surface.

Nowadays, how to grow graphene on Ni(111) by CVD is well-known and extensively reported in literature, leading to the production of reproducible and scalable layers [56, 103, 104]. This procedure, summarized below, is the starting point of this thesis, in order to obtain flat and homogeneous graphene layers on Ni(111).

Ni(111) single crystals are usually cleaned by cycles of Ar⁺ sputtering and subsequent annealing at high temperature (around 700 °C). These cleaning conditions ensure the removal of the impurities from the surface and its reconstruction, resulting in wide (~ 100 nm) and flat terraces. Once cleaned, low-pressure CVD is carried out by employing a commonly used C-containing precursor, ethylene (see Figure 2.5a and b).

This gas phase precursor, the simplest alkene, is a hydrocarbon molecule with carbon-

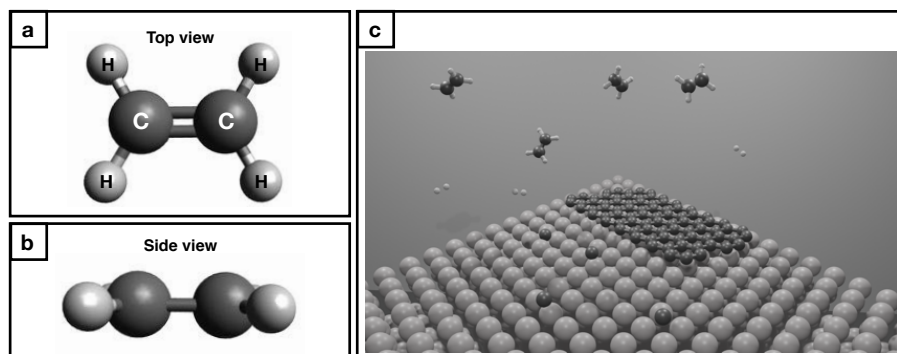


Figure 2.5: (a) Top and (b) side view of the ball-and-stick model of ethylene (C₂H₄). (c) Schematic representation of the CVD graphene growth on a Ni(111) substrate.

carbon double bonds, whose chemical formula is C₂H₄ (or H₂C=CH₂). All six atoms that form ethylene are coplanar and the H-C-H angle is close to 120°. The π -bond in the ethylene molecule is responsible for its relevant reactivity. Indeed, the double bond is a region of high electron density and several transition metals are able to catalyze its reactions. Due to these features, ethylene represents a really good precursor to use in the CVD graphene growth on transition metals, like Ni.

The well known catalytic properties of the Ni substrate, combined with the hot temperature at which it is kept, allow for the dehydrogenation and the cracking at the surface of the ethylene molecules. Carbon atoms, dissolving into the bulk and then segregating on the surface, arrange in the ordered honeycomb structure of graphene, forming domains, as sketched in Figure 2.5c.

During the growth process, an important role is played by Ni surface atoms. Indeed, at high temperatures, they are not stable but move on the surface, actively participating in the graphene growth with a catalytic action that facilitates the incorporation of C atoms in the hexagonal network [65].

Depending on the experimental conditions, the final product of the growth can result in different graphene phases, namely *epitaxial graphene* or *rotated graphene*. If an epitaxial graphene layer is grown, the lattice is in register with the Ni substrate, since the mismatch between the two lattice parameters is less than 1% ($a_{Ni}=2.49 \text{ \AA}$ and $a_{Gr}=2.46 \text{ \AA}$). In the case of rotated graphene, the layer is twisted with respect to the Ni lattice with a typical rotation angle of around 17°, thus producing the expected moiré pattern obtained when two periodical lattices are superimposed [105]. The two different phases are clearly identifiable by LEED, where the long-range periodicity of the surface is represented in the reciprocal space. Typical LEED patterns of epitaxial and rotated graphene on Ni(111) are reported in Figure 2.6 [56].

The hexagonal spots are markers of the Ni substrate. Nevertheless, due to the small mismatch between the graphene and Ni lattices, the epitaxial graphene LEED structure corresponds to that one of the Ni substrate. On the other hand, rotated graphene domains are indicated by the arrows as arc-like features, indicating the coexistence of several rotated domains, twisted at different angles.

The experimental conditions, and in particular the growth temperature, play a key role in the final graphene phase (epitaxial and/or rotated). As it is reported in Ref[56] (see Figure 2.7), for bare Ni(111), below 500 °C the formation of an intermediate, structural surface carbide (Ni₂C) is favored, which then converts into epitaxial graphene. Above 500 °C, graphene predominantly grows directly on Ni(111) *via* replacement mechanisms lead-

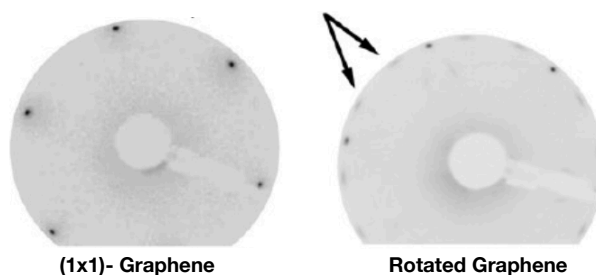


Figure 2.6: (1 \times 1)-Graphene and rotated graphene LEED patterns. From Ref[56].

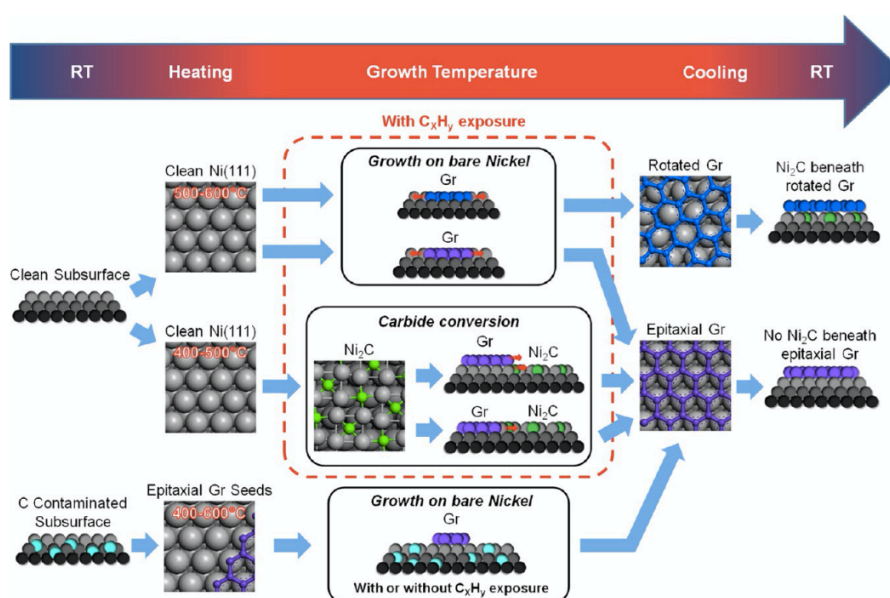


Figure 2.7: Graphene growth on Ni(111) in different experimental condition. From Ref[56].

ing to embedded epitaxial and/or rotated graphene domains.

Moreover, it is important to note that, due to the high solubility of C into the Ni metal substrate, the final phase of graphene is also strongly affected by the amount of C dissolved into the Ni bulk. In particular, after the high-temperature growth process (above 500 °C) and during the cooling of the system at room temperature, carbon bulk diffusion was observed to induce the formation of surface nickel carbide as an interlayer between graphene and Ni [56]. In this case, carbide is formed only below the rotated graphene domain. This is because graphene in the epitaxial configuration, *i.e.* in registry with the Ni(111) substrate, is more strongly adsorbed than rotated graphene, preventing carbon segregation to the surface, while rotated graphene is more weakly interacting and thus carbon can segregate from the Ni bulk more easily during the surface cooling, forming an interface of Ni₂C.

The different graphene phases are identifiable also from a spectroscopic point of view by means of XPS. Several experimental works are in agreement in identifying different subcomponents in the C 1s spectrum of graphene on Ni(111) [56, 100, 106]. In Figure 2.8, a typical C 1s core level spectrum measured for graphene on Ni(111) is shown.

In line with literature, the authors associated the main component, centered at a binding energy of 284.8 eV, to graphene strongly interacting with the Ni substrate. Then, two additional components are added to the data fitting: one centered at 283.2 eV and the other

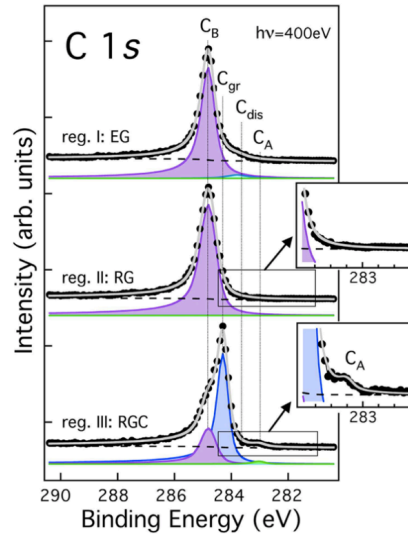


Figure 2.8: C 1s spectrum of graphene on Ni(111). From ref.[100].

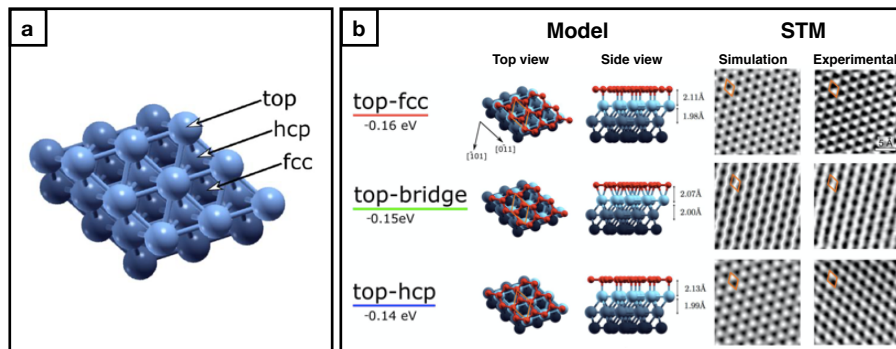


Figure 2.9: (a) Ball-and-stick model of the Ni(111) surface, where the arrows indicate top, hcp and fcc sites. (b) Different epitaxial graphene/Ni(111) configurations. Stick-and-ball models of top-view and side-view, and corresponding simulated and experimental STM images. Adsorption energies are indicated in brackets below the name of each configuration. From ref.[107].

at 284.4 eV, associated to Ni₂C and weakly-interacting graphene ascribed to the rotated domains with Ni₂C underneath, respectively [100].

Finally, different configurations of epitaxial graphene have been demonstrated to coexist on top of a Ni(111) surface [107, 66, 108], forming three chemisorbed structures with high symmetry arrangements, as sketched in Figure 2.9:

- the *top-fcc* and *top-hcp* configurations, where C atoms of one graphene sublattice are adsorbed on top of the first layer substrate atoms (top sites), and the other C atoms of the second sublattice over fcc or hcp hollow sites, respectively.
- the *top-bridge* configuration, where the C-C bonds are bridging the Ni top sites.

It was theoretically shown that the top-fcc, top-hcp and top-bridge arrangements are practically isoenergetic (see Figure 2.9), and can coexist in the same graphene monolayer [107].

2.5.2 N-doped Graphene on Ni(111)

In literature, the growth and characterization of N-doped graphene on Ni(111) still has several open questions to be addressed and investigated in detail. It is usually grown by CVD using N- and C-containing precursors [27, 109], or by a post-synthesis approach, where doping is achieved by low-energy nitrogen implantation in a previously grown graphene layer [110].

Experimentally, to the best of our knowledge, a clear morphological characterization at the atomic scale for the N-doped graphene layers on Ni(111) is still missing, while it has been reported for N-doped graphene grown on several other substrates (Cu, Pt etc.) [25, 28, 111]. On the other hand, a complete spectroscopic characterization of the as-grown N-doped layers is already reported in literature, even for N-doped graphene on Ni(111), clearly showing nitrogen fingerprints in the core level spectra. In particular, Usachov *et al.* showed that N-doped graphene grown by CVD usually contains nitrogen atoms in different chemical environments, as evidenced by the complex, multi-component profiles of the N 1s spectra (see Figure 2.10a from Ref [27]).

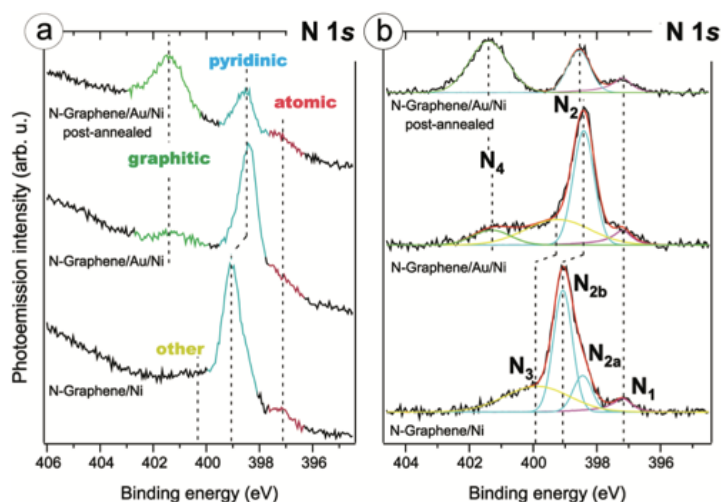


Figure 2.10: (a) XPS of the N 1s core level spectra acquired from N-doped graphene on Ni(111) samples. (b) Least-squares fit analysis of the line shape of the spectra in (a) allowing the discrimination of contributions from different nitrogen atoms configurations. From Ref [27].

The deconvolution of the spectra into individual components (Figure 2.10b from Ref [27]) allowed the authors to identify different nitrogen configurations: an asymmetric feature at ~ 399 eV of binding energy, decomposed into the N_{2a} , N_{2b} components, and two other peaks N_1 and N_3 at ~ 397.2 eV and ~ 400 eV, respectively.

Then, the authors intercalated gold at the interface between graphene and the Ni substrate. Upon intercalation, the two components N_{2a} and N_{2b} were observed to merge in a single peak and to shift to lower binding energy at ~ 398.4 eV, suggesting a nitrogen configuration embedded in the graphene network. Therefore, the initial asymmetry was associated to the different location and chemical interaction of the particular nitrogen atoms with nickel since, after gold intercalation, it reduced inducing a symmetric shape and leading to the N_2 component. According to the literature, the authors concluded that the N_2 component is ascribable to pyridinic N defects. After intercalation they highlighted the appearance of a new feature, labelled as N_4 and centered at a binding energy of 401.3 eV, which they identified as graphitic N configuration. Finally, the authors noticed that neither the en-

ergy position nor the intensity of the peak N_1 was affected by the intercalation processes. This indicates that the corresponding nitrogen atoms are not embedded into graphene but adsorbed on the nickel surface.

The growth method can drastically affect the configuration of N dopants trapped in the graphene network and their relative ratio. Zhao *et al.* synthesized N-doped graphene on Ni(111) by exposing a pristine graphene layer to a beam of low energy nitrogen ions. Then, they annealed the nitrogen bombarded graphene layer in order to "regenerate" the perturbed graphene lattice, leading to N-doped graphene [110]. As shown in Figure 2.11, the authors monitored the preparation steps by high resolution X-ray photoelectron spectroscopy, identifying two different doping sites in the N 1s core level spectrum.

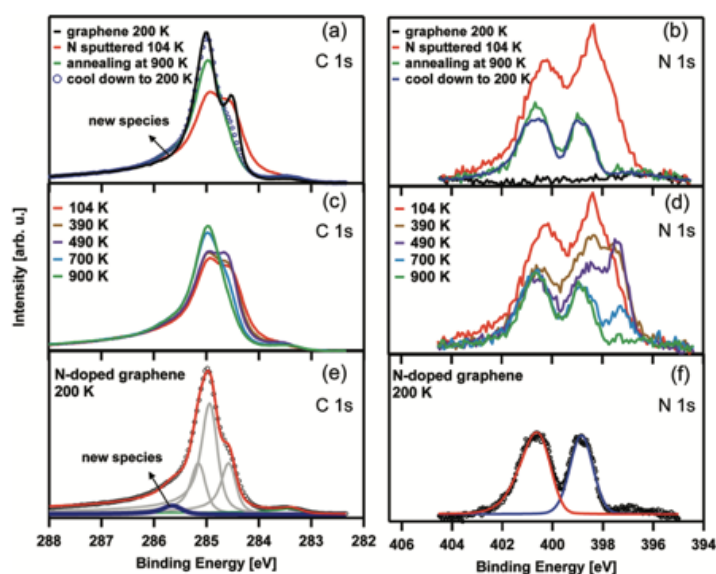


Figure 2.11: (a) C 1s spectra of graphene at 200 K, graphene sputtered with 50 eV nitrogen ions for 10 min below 120 K, nitrogen-sputtered layer after annealing at 900 K, and after cooling down to 200 K. (b) N 1s spectra corresponding to the data in (a). (c-d) Evolution of the C 1s and N 1s spectra of the sputtered sample. (e-f) Fitting of the C 1s and N 1s spectra of nitrogen-doped graphene, measured at 200 K. From Ref [110].

After N sputtering, two well-resolved symmetric peaks were observed at 398.7 eV and 400.7 eV, which, according to the literature, were ascribed to pyridinic and graphitic N, respectively. Based on the data fitting, after annealing at 900 K, the amount of graphitic and pyridinic nitrogen was determined to be similar (0.012 ML and 0.010 ML, respectively). It is worth noting that an annealing step at high temperature is required after the nitrogen bombardment in order to restore the good quality of the graphene layer and desorb excess nitrogen. However, in literature it is reported that the annealing process could have also another effect: the transformation of pyridinic N into graphitic N defects. In particular, Usachov *et al.* investigated the conversion of pyridinic dopants into graphitic ones, after a long annealing of a gold-intercalated N-doped graphene layer on Ni(111) [27, 112]. Nevertheless, the authors declared that, upon post annealing, for the N-doped graphene/Ni(111) the modification of the N 1s line shape was not as considerable as for N-doped graphene/Au/Ni(111).

The relative ratio between graphitic and pyridinic nitrogen dopants is actually crucial for the use of N-doped graphene in applications. Indeed, as explained in section 2.3.1, graphitic and pyridinic N induce an n- or p-type doping of graphene, respectively. There-

fore, finding a way to tune and convert one configuration to another, may allow to have control on the doping effect.

2.5.3 Pristine and N-doped Graphene on Ni(111): CO reactivity

The substrate supporting graphene plays a crucial role in tuning its properties, significantly affecting also the interaction with gases [17]. In this case, such effect can be ascribed to the substrate "affinity" to the considered gas. In the case of CO on Ni(111), an in-depth investigation from both a theoretical and experimental point of view was reported in literature [113, 114, 115, 116]. CO was demonstrated to adsorb on Ni(111) surface in different temperature and pressure conditions, forming ordered superstructures in strict relation to the CO coverage [117, 118]. However, a clear and unambiguous relation between CO coverage and surface structure is still missing.

Based on this, graphene on Ni(111) was investigated as promising material for CO detection. It was experimentally demonstrated that graphene on Ni(111) is inert if exposed at RT to a low partial pressure of CO ($\sim 10^{-6}$ mbar), while adsorption on the surface occurs at ~ 120 K [24]. On the other hand, a defective graphene sheet shows an enhancement of the interaction with CO. Celasco *et al.* demonstrated that C vacancies in graphene, formed by bombardment of a pristine graphene layer on Ni(111) with Ne^+ ions, promote the CO adsorption in presence of a reactive substrate such as Ni [18].

By increasing the CO exposure pressure in the millibar regime, CO was demonstrated to intercalate at the interface between the pristine graphene layer and the Ni(111) substrate [106]. Wei *et al.* systematically exposed a previously grown graphene layer on Ni(111) to several CO pressures. The resulted XPS spectra for O 1s and C 1s core levels are reported in Figure 2.12.

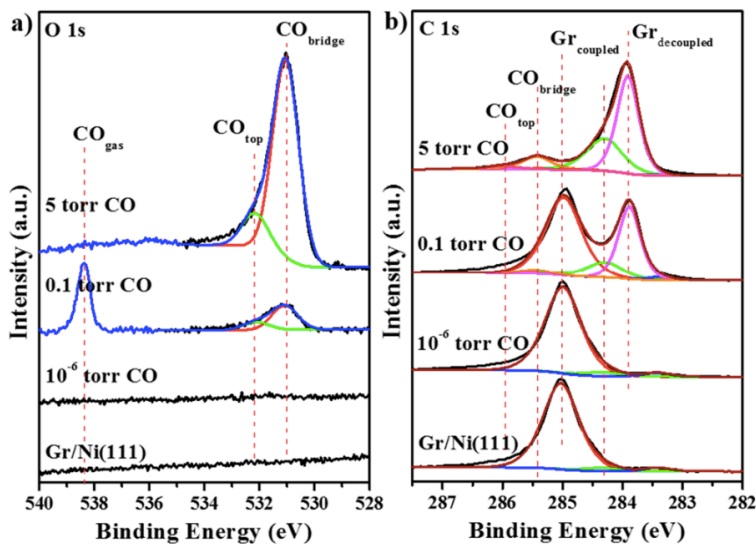


Figure 2.12: XPS O 1s (a) and C 1s (b) core level spectra of graphene on Ni(111) for various CO exposure pressures. From Ref [106]

After exposure to low pressure of CO (1×10^{-6} Torr), the authors reported no changes in the C 1s and O 1s spectra. Interestingly, at 0.1 Torr CO, a weak O 1s signal at 531 eV and a new peak at 283.9 eV in the C 1s spectrum were detected, associated to CO adsorbed on bridge site of Ni(111) and graphene decoupled from its substrate, respectively, suggesting that intercalation occurred already at this pressure. Increasing the CO pressure up to 5

Torr, in the C 1s spectrum the component at 283.9 eV becomes dominant, indicating that graphene was completely intercalated by CO, decoupling it from the Ni substrate. Nevertheless, to the best of our knowledge, from an experimental point of view just few works were published on this topic so far.

N-doped graphene system is theoretically reported to be more sensitive to gases with respect to the pristine case, due to the presence of doping centers embedded in the graphene network. In 2018, Carraro *et al.* reported the adsorption of CO at low pressure on N-doped graphene on Ni(111) at low temperature, around 90 K, demonstrating that no interaction occurs at RT [88], similarly to the case of pristine graphene on Ni(111) [24]. On the other hand, so far, nothing is reported about the exposure of the N-doped graphene on Ni(111) to high pressure of CO and the role played by the nitrogen dopant sites is still an open question to be addressed.

Based on what discussed so far, although several theoretical works predict N-doped graphene as a promising material suitable for a variety of applications, to the best of our knowledge, just few experimental works are reported in literature on this topic. In this context, the results presented and discussed in this thesis attempt to address some of the open questions, in particular concerning the interaction with gases, providing experimental evidences and trying to make a step forward in the investigation of this topic.

Chapter 3

Experimental Methods

3.1 Why Ultra High Vacuum (UHV)

In order to be able to investigate a solid surface at the atomic scale, the interaction between the surface and any reactive species from the environment should be minimized to avoid contaminations. This means that in order to reach such condition, we have to work in vacuum conditions.

According to the kinetic theory of gases [119], the flux I of molecules that arrive on a surface from the surrounding environment can be written as:

$$I = \frac{p}{\sqrt{2\pi mk_B T}},$$

where p is the pressure, m is the molecule mass, k_B is the Boltzmann constant, and T is the temperature. From this, we can consider:

$$n = \frac{p}{k_B T}, \text{ molecular density in the gas above the surface,}$$

$$\lambda = \frac{f}{n\sigma^2}, \text{ mean free path of a molecule in the gas phase above the surface,}$$

$$\tau = \frac{n_o}{I} = \frac{n_o \sqrt{2\pi mk_B T}}{p}, \text{ time required to form a monolayer,}$$

where f is the collisional frequency, σ^2 is the molecular cross-section, and n_o is the number of atoms in a monolayer (one monolayer corresponds to the number of surface atoms of the investigated surface). These parameters can be used to define the pressure conditions needed for typical surface science experiments. Table 3.1 displays how these parameters vary with pressure. If the experiment requires that the number of atoms or molecules adsorbed on the surface from the gas environment in almost one hour should not exceed a few per cent of a monolayer, a vacuum of the order of 10^{-10} mbar or better is required to satisfy such condition.

Several units are used for measuring vacuum pressures, the most common being Pascal (SI unit, $1 \text{ Pa} = 1 \text{ N/m}^2$), millibar ($1 \text{ mbar} = 100 \text{ Pa}$) and Torr (or millimeters of mercury, mmHg, $1 \text{ Torr} = 133 \text{ Pa}$). In this thesis, we will use mbar as unit of pressure.

3.2 Scanning Tunneling Microscopy

Scanning tunneling microscopy (STM) is a surface sensitive technique that allows imaging surfaces at the atomic scale, thus representing a turning point in the field of nanotechnology. Based on the quantum tunneling effect, STM senses the surface by using an extremely

Pressure, p , Torr	Molecular density, n , cm^{-3}	Arrival rate, I , $\text{cm}^{-2}\text{s}^{-1}$	Mean free path, λ	Monolayer arrival time, τ
760	2×10^{19}	3×10^{23}	700 Å	3 ns
1	3×10^{16}	4×10^{20}	50 μm	2 μs
10^{-3}	3×10^{13}	4×10^{17}	5 cm	2 ms
10^{-6}	3×10^{10}	4×10^{14}	50 m	2 s
10^{-9}	3×10^7	4×10^{11}	50 km	1 hour

Figure 3.1: Molecular density n , arrival rate I , mean free path λ , and the time constant to form a monolayer τ for nitrogen molecules at room temperature, $T=293$ K. The sticking coefficient is assumed to be unity and the density of one monoatomic layer is defined to be $n_0 = 10^{15} \text{ cm}^{-2}$. From Ref. [119]

sharp conducting tip that can distinguish features with the Å resolution.

In this chapter, the physical principles and the instrument setup of the scanning tunneling microscope will be described in detail, in order to properly understand the experimental STM results presented in the following chapter.

3.2.1 STM Theory

The scanning tunneling microscope (STM) was invented and first implemented in 1981 by Gerd Binnig and Heinrich Rohrer. They received the Nobel Prize in 1986 for this invention, which allowed scientists to open a new window on the fascinating nano-world and visualizing for the first time atoms on a surface.

The physical principle on which the STM is based is the quantum mechanical phenomenon of the *tunneling effect*, where a particle is able to overcome a potential barrier that classically can not be surmounted. Indeed, in quantum mechanics, an electron is described by a wave-function $\psi(z)$ satisfying the Schrödinger's equation:

$$-\frac{\hbar^2}{2m} \frac{d^2}{dz^2} \psi(z) + U(z)\psi(z) = E\psi(z)$$

where m is the electron mass (9.1×10^{-31} kg). Let's consider now the case of a piecewise-constant potential barrier, as sketched in Figure 3.2.

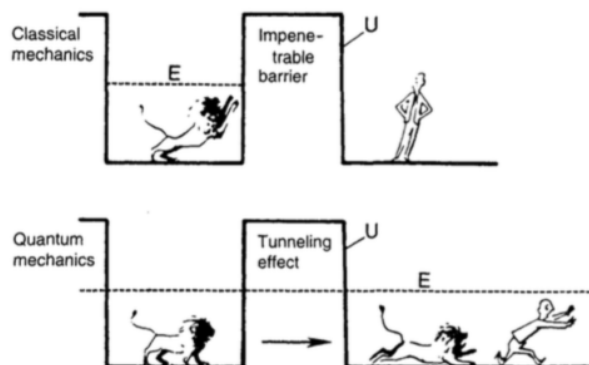


Figure 3.2: Difference between classical and quantum theory. In quantum mechanics, an electron has a nonzero probability of tunneling through a potential barrier. From Ref. [120].

In the classically allowed region, where $E > U$, the solutions of the Schrödinger's equation are:

$$\psi(z) = \psi(0)e^{\pm ikz}, \text{ where } k = \frac{\sqrt{2m(E-U)}}{\hbar} \text{ is the wave vector.}$$

While in the classical forbidden region, where $E < U$ the solution is:

$$\psi(z) = \psi(0)e^{\kappa z}, \text{ where } \kappa = \frac{\sqrt{2m(U-E)}}{\hbar} \text{ is the decay constant.}$$

In this case, the probability density for an electron to be at position z is proportional to $|\psi(0)|^2 e^{-2\kappa z}$, which represents a nonzero probability for the electron to penetrate the barrier.

Using this elementary model, we can explain the metal-vacuum-metal tunneling, as shown in Figure 3.3.

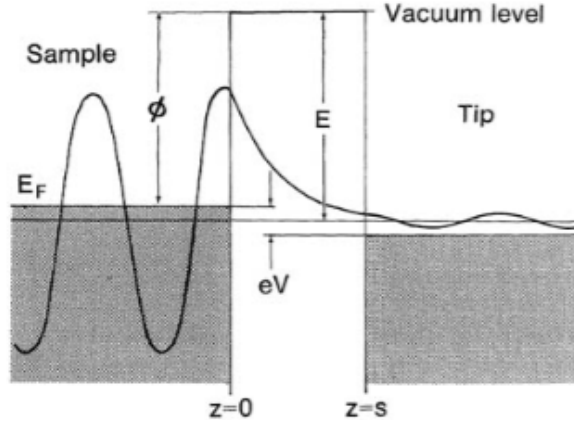


Figure 3.3: A one-dimensional metal-vacuum-metal tunneling junction. From Ref. [120].

If a positive bias is applied to a sample with respect to the tip, the electrons will tunnel from the tip into the sample empty states, while for a negative bias, they will tunnel from the sample occupied states to the tip. The potential barrier can be approximated to the work function ϕ of the sample surface, defined as the energy required to remove an electron from the Fermi level E_F to the vacuum level.

Thus for electron levels close to E_F , neglecting the thermal energy contribution:

$$I \propto |\psi_n(0)|^2 e^{-2\kappa s}, \text{ where } \kappa = \frac{\sqrt{2m\phi}}{\hbar} \text{ and } s \text{ is the tip-sample distance.}$$

Considering a typical metal work function $\phi \approx 4eV$, a typical value of the decay constant is about 1 \AA^{-1} is obtained. This gives an estimation of the current decay with distance of about one order of magnitude with a distance increase of 1 \AA .

In order to extend the one-dimensional tunneling problem to the three-dimensional case, we will follow the formalism introduced by Bardeen [121]. The tunneling probability from a state ψ , on one side of the barrier, to a state χ , on the other side, can be expressed by the matrix element as:

$$M = \frac{\hbar}{2m} \int_{z=z_0} (\chi^* \frac{\partial \psi}{\partial z} - \psi \frac{\partial \chi^*}{\partial z}) dS,$$

where $z = z_0$ is any separation surface lying entirely between the sample surface and the tip. Then, the tunneling current can be expressed through the Fermi golden rule as:

$$I = \frac{4\pi e}{\hbar} \int_{-\infty}^{+\infty} [f(E_F - eV + \epsilon) - f(E_F + \epsilon)] \cdot \rho_S(E_F - eV + \epsilon) \rho_T(E_F + \epsilon) |M|^2 d\epsilon$$

Assuming that $k_B T$ is small enough to approximate the Fermi distribution with a step function, and the M matrix is almost constant within the energy range of interest, the last equation is simplified as:

$$I \propto \int_0^{eV} d\epsilon \rho_S(E_F - eV + \epsilon) \rho_T(E_F + \epsilon).$$

Within the Bardeen's formalism, the tunneling current is then expressed as a convolution of the density of states of the sample and the tip. Considering now the Tersoff-Hamann approximation, in which the tip has only one s -like orbital in the apex atom [122], the tunneling current can be expressed as:

$$I \propto \int_0^{eV} d\epsilon \rho_S(\vec{r}_T, \epsilon),$$

where $\rho_S(\vec{r}_T, \epsilon)$ is the local density of states of the sample at energy ϵ and at the position of the tip apex.

In STM the sample surface is scanned by the tip, and an image is created by recording the tunneling current I , or the distance between the tip and the sample d at each position.

In the so-called *constant height mode* the absolute z position of the tip is kept constant with respect to the sample surface, and the image is given by the variation of the recorded tunneling current. On the other hand, if the tunneling current is kept constant by a feedback mechanism able to change the tip-surface distance, a topographic image is obtained in the so-called *constant current mode*. In this case the image represents a convolution between the topography of the surface and the local density of the states at the energy defined by the bias voltage. All the images that we will show in this thesis are obtained using the constant current mode.

3.2.2 Scanning Tunneling Spectroscopy

As discussed in the previous section, the tunneling current is directly proportional to the local density of states of the sample surface, thus allowing to perform spectroscopic measurements with STM. This technique is generally referred as Scanning Tunneling Spectroscopy (STS) [123, 124] and will be briefly described in the following.

According to the Bardeen's formalism and assuming a tip with a constant density of states (DOS), from the equation of the tunneling current, its first derivative can be written as:

$$\frac{dI}{dV} \propto \rho_S(E_F - eV)$$

Thus, the DOS of the sample close to the Fermi level can be directly probed through the first derivative of the tunneling current. Since the tunneling current exhibits a dramatic dependence on the tip-sample separation ($I = I_0 e^{-2\kappa z}$), which means that the tunneling

current varies approximately one order of magnitude per Å, STS data need to be adequately normalized. The commonly used normalization is the one proposed by Feenstra and Stroscio [125], in which the *normalized dynamic conductance* is given by:

$$g_N(V) \equiv \frac{d \ln I}{d \ln V} = \frac{dI}{dV} \cdot \frac{V}{I}$$

In order to experimentally acquire dI/dV spectra, the lock-in technique is used to extrapolate the signal of interest, the first derivative of the tunneling current. Usually, to perform STS measurements, the tip is placed above a site of interest on the surface, then the feedback loop is switched off and the voltage is ramped while recording the signal from the lock-in amplifier.

The resolution achieved in the dI/dV spectra is strongly dependent on the temperature and, in order to perform STS with high energy resolution, it is then necessary to work at low temperatures. Moreover, working in low temperature conditions ensures a higher stability of the tip and a higher precision on its relative position, since the thermal drift is drastically reduced.

In the point spectroscopy described so far, the dI/dV signal is recorded as a function of voltage at one specific point above the surface. More information related to the variation of the electronic structure across the surface can be obtained by the spatial mapping at a specific energy. A spectroscopic image yielding the map of the local density of states (LDOS) at a given energy eV can be obtained by performing a scan at a given bias voltage V and simultaneously recording the (normalized) dI/dV signal at each position. An image of the differential conductance (or LDOS map) is then acquired for a specific bias voltage.

3.2.3 STM setup

The STM instruments used to obtain the results presented in this thesis are two commercial Omicron scanning tunneling microscopes, one operating at variable temperature (VT-STM) and the other operating at low temperature (LT-STM) (see Figure 3.4), located at the STRAS (Surface sTructure and Reactivity at the Atomic Scale) laboratory at CNR-IOM laboratories in Trieste.

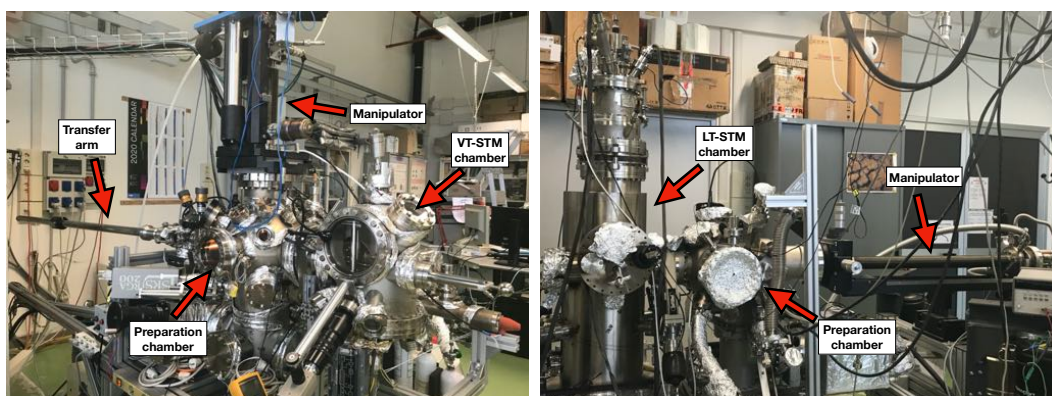


Figure 3.4: The experimental setup: commercial Omicron VT-STM (on the left) and LT-STM (on the right).

Variable Temperature STM (VT-STM)

The VT-STM is adapted in order to improve the mechanical stability and to work under reaction conditions, such as during gas exposure, in a wide range of sample temperatures. The system is formed by a preparation chamber connected to the STM chamber, where the microscope is housed. The background pressure is maintained in the low 10^{-10} mbar range through a magnetic levitation turbo molecular pump and an ion pump. The turbo molecular pump has been decoupled from the chamber, in order to avoid any vibrations that could affect the STM measurements.

Preparation Chamber : the preparation chamber is equipped with a manipulator able to move in the three spatial directions (x, y, and z) and to rotate in the polar direction (polar angle in the x-y plane). On the manipulator, the sample can be cool down to -183 °C by fluxing liquid nitrogen, or heated up to 1000 °C by means of graphite heating element supported by a pyrolytic boron nitride (PBN) plate directly hosted inside the sample holder. The manipulator head consists of a copper-aluminum alloy (GLIDCOP) block, thermally coupled but electrically isolated from the rest of the chamber by a sapphire plate. The manipulator head is provided with two sample stages that host the electrical connections for the temperature read-out (through a K-type thermocouple) and the sample heating. One of them is thermally decoupled from the remaining part of the manipulator, allowing to reach high temperatures, while the other is characterized by a good contact between the back of the sample holder and the manipulator head, providing the possibility to cool down the sample. A magnetic arm allows transferring the sample from the manipulator to a carousel hosted in the STM chamber.

The preparation chamber is also equipped with:

- a sputter gun for sample cleaning by ion bombardment (Ar^+);
- a residual gas analyzer (RGA), useful for process control and contamination monitoring and for leak testing;
- Low-Energy Electron Diffraction (LEED) optics, for long-range structural characterization of the samples;
- a gas line, allowing to dose various gases in the chamber background;
- a metal evaporator;
- an hot filament ion gauge, to measure the pressure in the chamber;
- a load lock system, providing a quick way to insert and extract samples and STM tips in the preparation chamber without breaking the vacuum. The chamber also host an home-made high pressure cell composed by a sample stage equipped with connectors able to measure the temperature of the sample, and inlet and outlet gas lines. Once the cell is closed, the sample can be exposed to gases *in situ* at pressures up to 20 mbar. After exposure, the sample can be then transferred in the main chamber for the characterization without breaking the vacuum.

STM Chamber : In our setup, the VT-STM can be operated in a temperature range between RT to 600 °C, by means of the PBN supported heating element inside the sample holder. The STM tip (made from a chemically etched tungsten wire) is mounted on a magnetic stage fixed on a single tube scanner with a maximum scan range of about $15 \times 15 \mu\text{m}^2$ and a z-travel of about $1 \mu\text{m}$. A small radiation shield is fitted on top of the scanner tube to limit

thermal drift. In order to obtain a precise temperature read-out, the sample holder and the STM wiring have been modified to measure the temperature directly on the sample. The coarse approach is monitored by a CCD camera, up to some tens of microns, whereas the fine approach is performed automatically through the control electronics.

A spring system, which suspends the heavy base platform of the STM, ensures a full mechanical isolation, while the base platform suspension is damped by an eddy current system. The platform, indeed, is surrounded by copper plates, centered between permanent magnets fixed on the chamber.

Low Temperature STM (LT-STM)

The LT-STM is basically an STM designed for working at very low temperatures, allowing to carry out stable imaging and spectroscopy of the sample surface. The system is formed by a preparation chamber separated from the STM chamber by a gate valve. The preparation chamber is pumped by a turbo pump together with an ion pump equipped with a titanium sublimation cartridge and a liquid nitrogen cooled cryopanel, keeping the vacuum in the low 10^{-10} mbar range. The vacuum in the STM chamber is maintained in the range of 10^{-11} mbar through an ion pump.

Preparation Chamber : the sample preparation chamber is designed around a horizontal manipulator used to position the sample and the STM tip in front of the various instruments. On the manipulator, the sample can be heated up to ~ 1000 °C through filament heating and electron bombardment, or cooled down till ~ -200 °C (~ 75 K) by fluxing LN₂.

The preparation chamber is equipped with:

- a sputter gun, for samples cleaning by bombardment with noble gases (Ar⁺);
- a residual gas analyzer (RGA);
- Low-Energy Electron Diffraction (LEED) optics;
- a gas line;
- a metals evaporator;
- a hot filament ion gauge;
- a fast-entry lock.

STM Chamber : our experimental system is based on a commercial Omicron LT-STM with a dedicated UHV chamber equipped with a carousel where tips and samples can be stored, retrieved and inserted into the LT-STM by means of a wobble-stick. To prevent stray radiation from increasing the sample temperature, the windows for optical access of the chamber are infrared filtered. The Omicron LT-STM head hosts a single-tube piezoelectric hollow cylinder, with the tip fixed at the top, and covered with four electrodes which split the cylinder in four quadrants. By applying suitable voltage difference between the quadrants and the inner electrode, the piezoelectric cylinder can be bent in order to scan the tip laterally onto the sample (x-y plane) with sub-angstrom resolution. Moreover, the tip can be moved orthogonally to the sample surface (z direction) with a voltage difference applied between the inner and the outer surface of the cylinder. For mechanical isolation purposes, the STM head can be suspended by means of three springs. Moreover, an eddy current damping system, provides effective, smooth damping of possible low frequency

instabilities.

The operating temperature range of our LT-STM is between 2.5 K and room temperature (RT). To reach temperatures below RT a cooling system made up of two concentric cylindrical cryostats is used (the STM head is fixed below them) which are filled with cryogenic liquids: liquid nitrogen (LN₂: boiling point at 77 K) and liquid helium (LHe: boiling point at 4.2 K). The external cryostat is always filled with LN₂, while the inner cryostat can be filled with LN₂ or LHe according to the desired temperature.

3.3 Photoemission Spectroscopy

Photoemission spectroscopy (PES) is the most commonly used experimental technique to probe the electronic properties of the materials, providing information on the bands structure of the occupied states and on the bond states of atoms which compose the material under investigation. PES is based on the photoelectric effect and, in its simpler version, it measures the kinetic energy distribution of photoelectrons emitted from a sample, when it is irradiated with monochromatic light [126].

In this thesis, PES has been performed to chemically characterize the pristine and N-doped graphene layers and their reactivity, providing important information about the nature and the role of the N dopants in interaction with gases.

In this chapter, the elementary concepts of the experimental technique are briefly reported, limiting the description to the basics, useful to the understanding of the experimental data discussed. A more detailed and complete discussion can be found in Ref.[127, 128].

Then, the experimental setup used to carry out measurements is described.

3.3.1 PES: fundamental basis

The phenomenon of the photoemission was observed for the first time by Hertz in 1887 and it was subsequently theorized by Einstein in 1905, for which he won the Nobel Prize in 1921.

In a first approximation, within a single particle picture, when a photoemission takes place (see Figure 3.5), the photon transfers its energy $h\nu$ to the photoelectron which leaves the sample with a kinetic energy E_{kin} given from the relation:

$$E_{kin} = h\nu - E_b - \phi_S$$

where ϕ_S is the work function of the material. In order to detect the photoelectron ejected from a surface, the following conditions have to be satisfied:

- the photon energy $h\nu \geq E_b + \phi_S$
- the photoelectron velocity must be directed toward the outer surface
- the photoelectron does not lose energy in collision with other particles.

Moreover, the photoelectron must overcome the potential barrier $\phi = \phi_A - \phi_S$, where ϕ_A is the work function of the electron analyzer. As a consequence, the kinetic energy of the photoelectron becomes:

$$E_{kin} = h\nu - E_b - \phi_A$$

which is independent from the sample's work function.

In general, photons can penetrate into a solid for several μm , but the sampling depth in the photoemission process is determined by the mean free path of the photoelectrons in

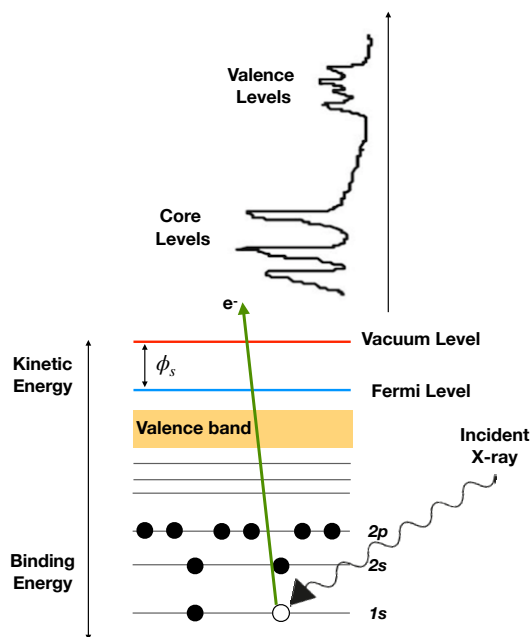


Figure 3.5: Sketch of the photoemission process.

the solid, which follows the universal curve of the energy-dependent inelastic mean free path of electrons in solids, and it changes as a function of the electron kinetic energy from about 4 Å to about 50 Å (see Figure 3.6).

However, even if photons penetrate for several μm the solid sample, photoelectrons coming out from the sample strongly interact with matter and easily de-excite because of multiple scattering. This means that only the electrons excited in the first atomic layers are ejected from the sample maintaining their original kinetic energy. This is the reason why PES is a surface sensitive technique, commonly used to investigate surfaces and thin films.

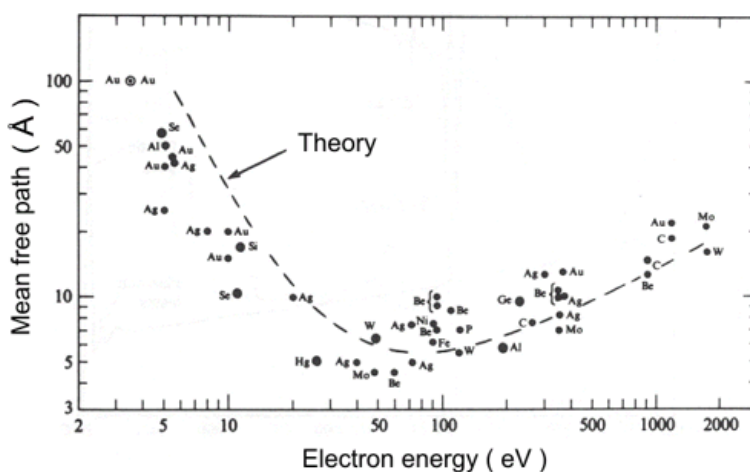


Figure 3.6: Universal curve of electron mean free path in solid.

3.3.2 PES setup

Generally, the photoemission experiments are performed in high vacuum chambers, in order to minimize the photoelectron energy loss by collision with other particles (see section 3.1). The setup includes a monochromatic photons source and an electron energy analyzer to record the spectra of the photoelectrons ejected from the sample under investigation.

Depending on the photon energy used for electron excitation, PES is usually divided in:

- **X-ray photoemission spectroscopy (XPS)**, if X-ray radiation is employed in the range between 100 eV and 10 KeV (corresponding to wavelengths from 100 to 1 Å). As a consequence, using XPS, deep core levels are probed.
- **Ultraviolet photoelectron spectroscopy (UPS)**, if ultraviolet radiation is employed in the range between 10 and 100 eV (corresponding to wavelengths from 1000 to 250 Å), having as a consequence the investigation of valence and conduction bands.

The photon sources can be of two types: *laboratory source*, specific for UPS and XPS, or *synchrotron radiation source*, covering the whole photoemission energy range.

The X-ray flux for XPS using laboratory sources is created by bombarding a target with high-energy electrons. Common target materials used for this aims are magnesium (Mg) and aluminum (Al), for which the photoemission spectrum is dominated by the unresolved doublet $K_{\alpha_{1,2}}$ ($2p_{1/2} \rightarrow 1s$ and $2p_{3/2} \rightarrow 1s$ transitions) at 1253.6 eV (Mg $K_{\alpha_{1,2}}$) and 1486.6 eV (Al $K_{\alpha_{1,2}}$). The line-width of the $K_{\alpha_{1,2}}$ doublet amount to ~ 0.7 - 0.8 eV for both materials. The alternative to use laboratory sources is synchrotron radiation source in which photons are emitted from the accelerated beam of charged particles running in bunch in a ring. The spectrum of the synchrotron radiation is essentially a continuum from few eV to several KeV. The photon energy selection is obtained by using appropriate monochromators.

The majority of the spectroscopical data presented in this thesis have been collected at the INSPECT laboratory (IN-situ Synthesis and PhotoEmission CharacTerization) at the CNR-IOM in Trieste, by means of a X-ray source.

The INSPECT experimental setup, schematically shown in Figure 3.7, consists in two aligned vacuum chambers: a preparation chamber and an analysis chamber. These chambers are kept in a UHV atmosphere by turbomolecular pumps, which are set in series with scroll pumps, maintaining the vacuum in the 10^{-10} mbar range.

Preparation Chamber : Along the common axis of the chambers, a manipulator is mounted, allowing the sample to move in the three spatial directions (x, y and z) and to rotate around the chamber axis. On the manipulator, the sample can be heated up to ~ 800 °C through a direct heating. Indeed, tantalum wires, put in direct contact with the sample, are heated and thus the sample temperature is increased. Several instruments to prepare and analyze the samples are also available into the chamber: LEED optics for long-range structures investigation, and molecule evaporators, where small crucibles, filled with the molecules powder, are rolled up with a filament. The latter is passed through by a current, which warms up the molecules allowing their evaporation in the experimental chamber. Moreover, a fast-entry lock system is mounted to rapidly insert and extract the samples into the chamber, without break the vacuum.

Analysis Chamber : In the analysis chamber, a X-ray source, an UV discharge lamp, an electron energy analyzer for photoemission spectroscopy, a residual gas analyzer (RGA) and an ion gun to clean the samples are located. This configuration allows to characterize the prepared sample *in situ*.

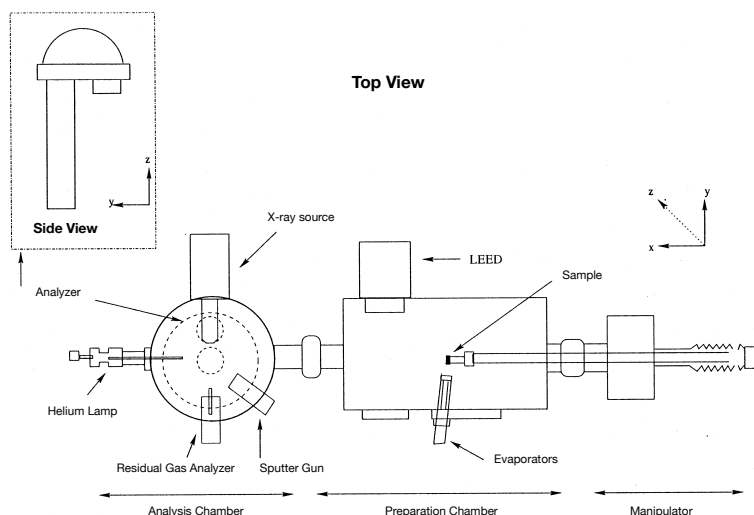


Figure 3.7: Schematic representation in top view of the experimental chamber at the INSPECT laboratory at the CNR-IOM in Trieste.

X-ray source : The source consists of a copper anode which is magnesium-covered on one side and aluminium-covered on the other side. Electrons are accelerated by a filament (one per side, so that the target and the emitted radiation can be chosen) through thermionic emission at a voltage of about 10 kV. The electrons collide against the anode, which acts as a target, and generate holes in core levels. Valence electrons fill these so-formed holes and consequently soft X-ray photons are emitted. These photons, impinging on the sample surface, produce photoelectrons which are collected in an hemispherical electrostatic analyzer. In general, more than one X-ray line is emitted from the anode, where the energy and line-width values depend on the particular material used.

Helium Lamp : For ultraviolet photoemission spectroscopy (UPS), a discharge helium lamp is available in the analysis chamber. Similarly to a X-ray source, this lamp also works thanks to spontaneous emission of radiation at a well-defined energy, and the emission lines are obtained by de-exciting an electron which was previously promoted from the highest occupied molecular orbital (HOMO) to the lowest unoccupied molecular orbital (LUMO).

Gaseous helium is inlet in a cylindrical pipe where, at the end of the latter is applied a voltage of some kV, in order to produce a direct electric discharge. This discharge causes a continuous transition of helium atoms from the ground level to a higher one, which de-exciting spontaneously emit photons.

There are two main spectral lines, usually called He I and He II: He I corresponds to the photon energy 21.22 eV, while the corresponding photon energy for He II line is 40.82 eV.

Analyzer : The analyzer in operation at the INSPECT laboratory at CNR-IOM is a PSP RESOLVE₁₂₀ Hemispherical Electron Energy Analyzer, and it is mounted on the analysis chamber so that its axis is aligned with the sample. The analyzer provides a kinetic energy distribution of the electrons, selecting them by deflecting their trajectories via an electrostatic field. Before the analyzer, a set of grids slows down the electrons, which then have a lower energy. The energy E_0 detected by the ana-

Besides the sharp peaks due to elastic photoelectrons, usually called primary structures, a continuous background is visible ascribed to the almost continuum distribution of the secondary electrons produced after the inelastic scattering within the solid. However, the analysis of the XPS spectra is not so trivial. Indeed, a core level binding energy strongly depends on the chemical bonds and the local environment of a specific atomic site. These interactions result in the so-called *core level shifts*, typically in the range from 1 to 10 eV. Therefore, an in depth analysis of the core level shifts provides important information on the chemical state of the investigated atomic species, making possible the identification of the chemical state of an atom in an unknown solid system.

The broad structure at the higher kinetic energies of the photoemission spectrum is related to the energy distribution of the valence band states. Their delocalized character, compared to the local nature of the core levels, induces a markedly change of their distribution in energy as the chemical bonds are changed.

In the photoemission spectra other structure are visible, such as Auger peaks, shake up losses and correlation satellites due to relaxation processes, like excitation and de-excitation of the system after the creation of the hole. Moreover, the cross-section for excitation is different for different electron levels, affecting the spectra shape.

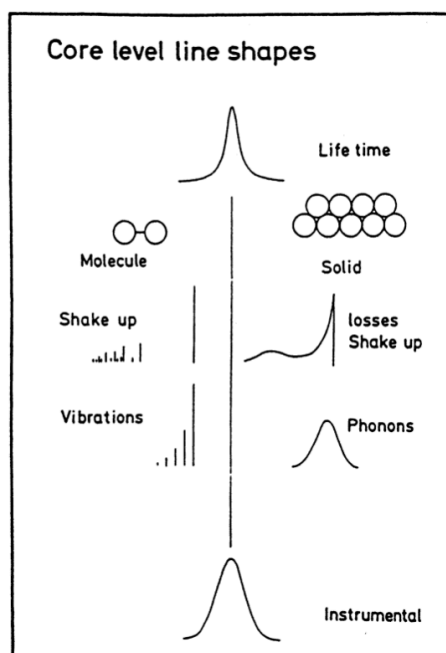


Figure 3.9: Schematic representation of the different photoemission lineshape contributions in an isolated molecule and a solid.

The width of a photoemitted peak depend on several factors, schematically indicated in Figure 3.9 and listed in the following points:

- **mean lifetime** of a hole created in the photoelectric process, whose typical de-excitation time is of the order of 10^{-14} - 10^{-15} s and goes by means of radiative or Auger processes, contributing to the photoemission peak width with a Lorentzian line-shape;
- **electronic excitations**, due to the electronic states of the system modified by the creation of the hole. This perturbation induces in metallic systems, where infinitesi-

mal excitations are possible across the Fermi level, a characteristic asymmetric line-shape of the photoemission peak toward lower kinetic energies [129];

- **phonon coupling**, connected to the vibrational modes of the system and caused by the excitation of electrons in a solid;
- **instrumental broadening**, due to the finite instrumental resolution of the electron energy analyzer and, often, to the non perfectly monochromatic character of the light source. These factors contribute giving a Gaussian broadening of the photoemission peaks.

Considering what just reported, in order to properly fit photoelectron line-shapes, a convolution of a Gaussian and a Lorentzian profile, known as *Voigt function*, is required. All the spectra were collected at RT in normal emission geometry using different experimental apparatuses, X-ray sources ($h\nu = 1486.7$ eV and $h\nu = 1253.6$ eV for Elettra and CNR-IOM apparatuses, respectively) and hemispherical electron energy analysers, with an overall experimental resolution of ~ 0.8 eV. All binding energies were calibrated by measuring the Fermi level. The spectra were normalized to the incident photon flux and analyzed by performing a non-linear mean square fit of the data.

3.4 Low-Energy Electron Diffraction

Low-energy electron diffraction is a powerful technique for surface structural investigations, which allows identifying the symmetry of an ordered crystal surface [127, 119]. In particular, LEED is based on the interference of beam of low energy (20-200 eV) collimated monochromatic electrons impinging normally on the sample surface. These electrons are diffracted and accelerated towards a fluorescent screen, forming a diffraction pattern, and thus providing structural information on the crystal surface.

Three are the main LEED operation modes. The simplest one, described and used in this thesis, consist in the determination of the surface lattice geometry through the analysis of the arrangement of the diffracted beams. In the second one, called LEED-IV, the intensities of diffracted beams are recorded as a function of the incident electron beam energy to generate the so-called I-V curves; by comparison with theoretical curves, these provide accurate information on the atomic positions on the surface. The third one, named Spot Profile Analysis Low-Energy Electron Diffraction (SPA-LEED), gives information on the surface order through the analysis of the shape of the diffraction peaks, as the sharper are the spots, the more ordered the surface is expected.

In the following sections, the geometrical theory and the experimental setup of this technique are briefly described.

3.4.1 LEED geometrical theory

According to the wave/particle duality, a monochromatic electron beam can be considered as a plane wave, whose wavelength is given by the de Broglie relation:

$$\lambda = \frac{h}{p} \Rightarrow \lambda = \frac{h}{\sqrt{2mE_k}}$$

where h is the Planck constant, and p is the electron momentum defined as $p = mv = \sqrt{2mE_k}$, where m is the electron mass (9.1×10^{-31} kg), v is the velocity (in ms^{-1}), and E_k is the kinetic energy (in eV).

This electron beam, impinging on a periodic structure such as a crystal surface, is scattered by the surface atoms which, being regions of high localized electron density, act as scattering points, giving rise to diffracted spherical waves. In order to obtain a diffraction pattern, the electrons wavelength has to be comparable to the lattice distances (\sim few Å), therefore the typical energies used in LEED range between 20 and 200 eV. This is a necessary condition to observe the diffraction effects associated with the atomic structure. Moreover, the mean free path of these low-energy electrons is very short inside materials, of the order of few atomic layers, and most elastic collisions occurs on the very top layers of the sample. Thus, LEED provides mainly information about the 2D atomic structure of the sample surface.

In more detail, considering a monochromatic electron beam impinging on a crystal surface with an incident angle θ , as sketched in Figure 3.10a, in order to have *constructive* interference between the scattered waves, these have to remain in phase and the difference between the path lengths of the incident and scattered waves ($2d\sin\theta$, see Figure 3.10a) has to be equal to an integer multiple of the wavelength. Therefore, the condition for the constructive interference, known as the *Bragg's law*, is:

$$2d\sin\theta = n\lambda$$

where n is a positive integer and λ is the wavelength of the scattered (and incident) wave. A diffraction pattern is obtained by measuring the intensity of scattered waves as a function of scattering angle. Very strong intensities known as "Bragg peaks" are obtained in the diffraction pattern at the points where the scattering angles satisfy the Bragg condition.

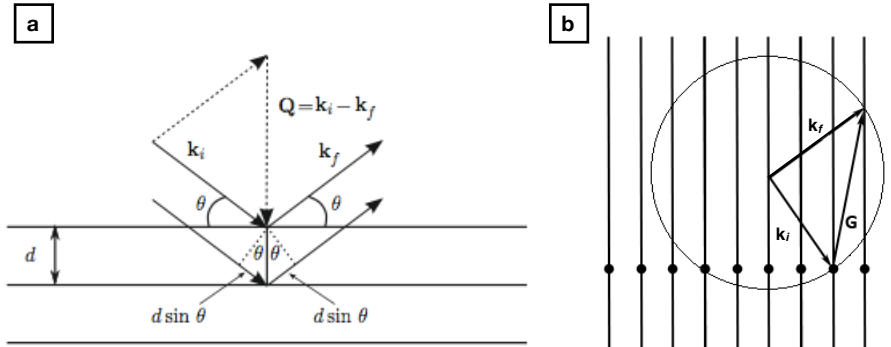


Figure 3.10: (a) Bragg diffraction. Two beams with identical wavelength and phase approach a crystal surface and are scattered off by two atomic planes. The lower beam crosses an extra length of $2d\sin\theta$. Constructive interference occurs when this length is equal to an integer multiple of the wavelength of the radiation. The geometrical construction of $\mathbf{Q} = \mathbf{k}_i - \mathbf{k}_f$ is also provided. From Ref. [130]. (b) Ewald construction for diffraction on a 2D surface lattice.

In a periodic system such as a crystal, the condition for elastic scattering is [130]:

$$\mathbf{Q} = \mathbf{k}_i - \mathbf{k}_f \equiv \mathbf{G}$$

where \mathbf{k}_i is the incident wave vector, \mathbf{k}_f is the scattered wave vector, and \mathbf{G} is the reciprocal lattice vector. Thus a necessary condition for diffraction is that the difference between the incident and scattered wavevectors equals a reciprocal lattice vector. The previous equation represents the law of conservation of momentum. Since for elastic scattering $|\mathbf{k}_i| = |\mathbf{k}_f| = 2\pi/\lambda$, then:

$$|\mathbf{Q}| = 2|\mathbf{k}_i|\sin\theta = 2\frac{2\pi}{\lambda}\sin\theta = n\frac{2\pi}{d}$$

where the previous equality follows from Bragg's law, and $|\mathbf{Q}|$ is an integer multiple of the quantity $2\pi/d$.

For the case of diffraction from a 2D surface, the law of conservation of the momentum becomes:

$$k_i^{\parallel} - k_f^{\parallel} = G_{hk}$$

Indeed, only the components parallel to the surface are involved in the law of conservation of the momentum and therefore, the scattering vectors parallel to the surface ($k_i^{\parallel} - k_f^{\parallel}$) must be equal to the vector of the 2D surface reciprocal lattice, G_{hk} . In order to easily determine the occurrence of elastic diffraction peaks, the geometrical construction due to Ewald can be considered, known as the *Ewald construction* for diffraction on a 2D lattice, reported in Figure 3.10b.

The reciprocal lattice rods perpendicular to the surface are related to every 2D reciprocal lattice point. To explain this, a 2D lattice can be imagined as a 3D lattice with infinite periodicity in the normal direction. Therefore, along the normal direction, the reciprocal periodicity tends to zero, and the reciprocal lattice points are infinitely dense, forming rods. The incident wave vector \mathbf{k}_i terminates at a reciprocal lattice rod. With its center at the origin of the vector \mathbf{k}_i , a circle of radius k_i is drawn, the *Ewald circle*. The intercepts of the rods with this circle define the scattered wave vectors \mathbf{k}_f for diffracted beams.

3.4.2 LEED instrumental setup

In order to detect the diffracted electron beams, LEED measurements are performed in UHV (see section 3.1) and the experimental setup, schematically represented in Figure 3.11, is composed by:

- an *electron gun*, which produces the low-energy electrons in a collimated beam;
- the *sample* under investigation,
- an hemispherical *fluorescent screen* with a set of four grids to observe the diffraction pattern of the elastically scattered electrons. It is important to note that the sample is placed at the center of curvature of the grids and screen;
- a camera connected to a PC in order to observe directly on the screen the diffraction pattern.

The electron gun unit consists of a cathode filament with a Wehnelt cylinder followed by electrostatic lenses. The cathode is at negative potential, $-V$, while the last aperture of the lens, the sample, and the first grid are grounded. The electrons emitted by the cathode are accelerated to an energy of eV within the gun and then propagate and scatter from the sample surface in the field-free space. The second and third grids have the purpose to reject the electrons not elastically scattered. The fourth grid is grounded and screens the other grids from the field of the fluorescent screen, which is biased to a high voltage of few kV, so that the elastically scattered, diffracted electrons are reaccelerated to the fluorescent screen, so that the diffraction pattern can be observed.

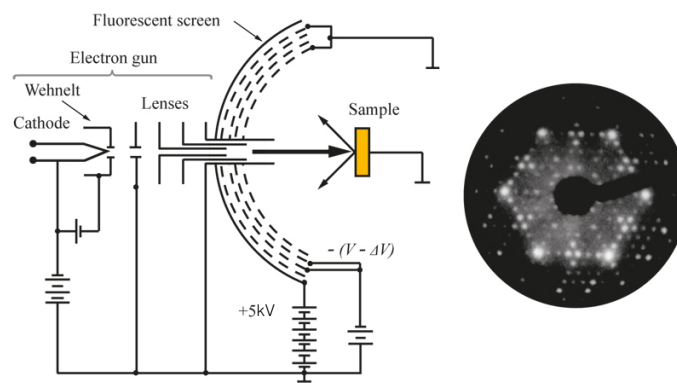


Figure 3.11: Schematic diagram of a standard four-grid LEED setup and LEED pattern of a Si(111)- 7×7 surface. From Ref. [119].

Chapter 4

N-doped Graphene on Ni(111)

In this chapter, the alternative and reproducible growth method we developed to obtain N-doped graphene on Ni(111) is described in detail.

The as-grown doped layer was thoroughly characterized by means of STM/STS and XPS. The experimental evidences, reported in the following sections, were corroborated and confirmed by Density Functional Theory (DFT) calculations and STM simulated images, allowing to unambiguously identify different N dopant configurations trapped in the graphene network [131].

4.1 Growth

As previously discussed in chapter 2, section 2.3.2, N-doped graphene on Ni is usually grown by a direct synthesis approach, such as CVD using N- and C- containing precursors, or by a post-synthesis approach, bombarding a previously grown pristine graphene layer with nitrogen atoms. However, in the first case the high pressure and temperature required for the growth process and the dangerous precursors needed, make the production troublesome, while in the second case the morphological quality of the resulting graphene film is drastically reduced.

In order to overcome these limitations, we developed an alternative method, structured in two steps: (i) N doping of a Ni substrate and (ii) standard low pressure (LP) CVD graphene growth. In this way, we introduce N in the graphene production process directly from the substrate itself, while performing the standard CVD growth, thus obtaining flat and continuous N-doped graphene layers.

The Ni(111) substrate was first cleaned by several cycles of Ar⁺ sputtering (1.5 KeV) and annealing (700 °C) in UHV. The cleanliness of the sample was checked by XPS (laboratory source), in order to assess the presence of core level peaks related to possible contaminants present in the crystal. In Figure 4.1, a typical wide scan of the Ni substrate is reported, where only peaks from Ni core levels and Auger excitations are visible and no detectable signals of other chemical species are noticeable.

The Ni substrate was N doped *via* its exposure to Tetraphenylporphyrin (zH-TPP) molecules which, decomposing on the surface, act as nitrogen source. zH-TPP (schematically represented in Figure 4.2a), a synthetic heterocyclic compound that resembles natural porphyrins, can be easily synthesized and appears as a dark purple powder. It is formed by a core porphyrin macrocycle, in which are present four nitrogen atoms, two iminic and two pyrrolic, attached to four phenyl rings, rotated with respect to the macrocycle plane. The behavior of these molecules when deposited in several experimental conditions on different metal surfaces was widely investigated and reported in literature, demonstrat-

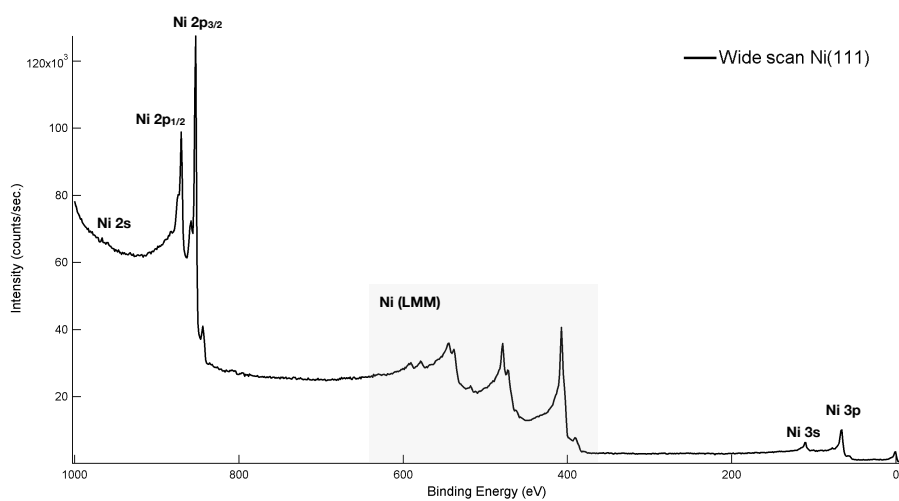


Figure 4.1: XPS wide scan of the Ni(111) substrate where core levels and Auger (Ni(LMM)) peaks of Ni are visible. A gray filled window highlights the Auger region in between 390 eV and 600 eV. Photon energy $h\nu = 1253.6$ eV.

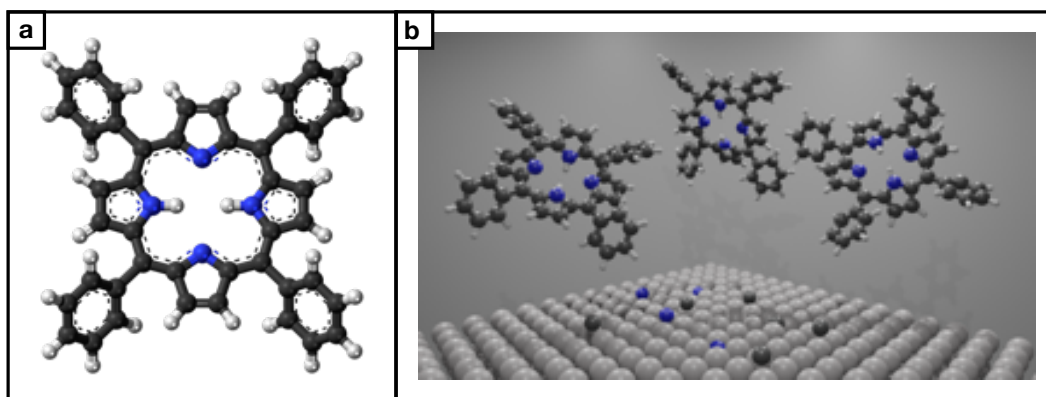


Figure 4.2: (a) Schematic representation of the Tetraphenylporphyrin (2H-TPP) formed by carbon (dark gray), nitrogen (blue) and hydrogen (white) atoms. (b) Sketch of the N doping procedure: the hot Ni substrate is exposed to a flux of 2H-TPP.

ing the strong effect of the substrate on their properties [132, 133, 134, 135, 136, 137, 138]. For example, by depositing these molecules at room temperature on Au [139, 140] and Ag [132] substrates, it was demonstrated that it is possible to obtain a single molecular layer without any modification of the macrocycle, which was shown to be adsorbed parallel to the substrate surface, whereas its phenyl legs exhibit a tilt angle of $\sim 50^\circ$ with respect to the surface plane [141]. On the other hand, after annealing at 250°C , Di Santo *et al.* predicted and observed a temperature-induced conformational adaptation of the porphyrin molecules on the surface [142]. The thermal stability of these molecules was also investigated. For example, Chen *et al.* reported that the NiTPP molecules on Au(111) are stable up to at least 300°C , while above 360°C , thermal decomposition of the molecules occurs [137].

Transition metals like Fe [143], Co [135], Ni [137] can be easily inserted in the 2H-TPP macrocycle to form metallo-porphyrins by in-situ metal evaporation on substrates like Ag(111) and Au(111). Alternatively, the metals can be directly coordinated by evaporation of the 2H-TPP monolayer on suitable metal substrates. Indeed, it was theoretically and experimentally reported that on reactive substrates, like Cu [144, 145, 146], Fe and Ni [138], single layers of 2H-TPP molecules metalate simply by picking-up substrate atoms or ad-atoms and the direct evidence of this metal coordination comes from the N 1s XPS spectrum [138]. In particular, in the N 1s spectrum of the 2H-TPP molecules two easily resolved components are expected, about 2 eV apart, due to the two N species: the one at higher binding energy is assigned to the two pyrrolic N atoms, while the lower binding energy peak corresponds to the two iminic ones. For example, in the case of 2H-TPP on Ag(111) these two peaks are centered at 399.6 eV and 397.6 eV, respectively [138]. In the metallo-porphyrin, instead, just one peak is observed with a binding energy in between the iminic and pyrrolic peaks, confirming that the four nitrogen atoms become equivalent and coordinated with a metal atom. This is the case of 2H-TPP adsorbed on Ni(111) at RT, for which just one peak at 398.5 eV was reported, clearly confirming the self-metalation of the molecule [138].

Our approach to N dope the Ni substrate takes advantage from its high catalytic activity, which allows cracking 2H-TPP molecules on the surface at relatively low temperatures, and exploits the well-known property of Ni to act as a "sponge" for several heterospecies. Indeed, theoretical calculations demonstrated that, besides carbon [99], also nitrogen and boron are easily diluted in the Ni crystal [147] and, in particular, the nitrogen solubility is nearly comparable to that of carbon. As for C atoms [56], N atoms are expected to dissolve into the Ni bulk and segregate to the surface, activated by the temperature (see the sketch reported in Figure 4.2b).

Following this strategy, a clean Ni(111) substrate was heated to $400\text{--}450^\circ\text{C}$, while thermalizing the 2H-TPP molecules for few minutes at a temperature slightly below the evaporation condition, in order to have a constant and reasonable flux of molecules impinging on the Ni surface during the exposure. Then, the Ni(111) substrate was exposed to the 2H-TPP flux for few minutes. The effectiveness of the doping procedure was checked by XPS.

As it is shown in Figure 4.3, the N 1s spectrum is dominated by the Ni(L₃VV) Auger tail, due to the photon energy of the Mg source used. However, a small shoulder is clearly visible in the N 1s core level region, in between 396 eV and 398 eV and we can unambiguously identify the main component of the nitrogen spectrum centered at ~ 397 eV.

Based on the existing literature, we would expect two peaks at 399.6 eV and 397.6 eV, if the 2H-TPPs were intact on the Ni surface and not metalated, or just one peak at 398.5 eV, if they were metalated [138]. In our case, we observe that there is a single main component

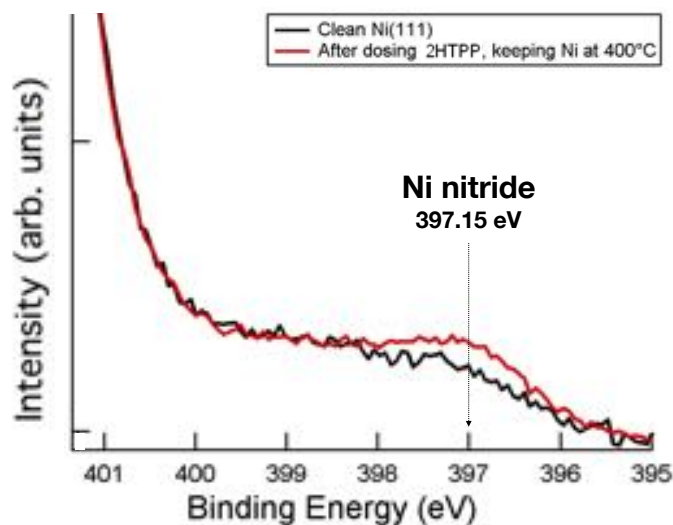


Figure 4.3: N $1s$ core level spectra of Ni clean (black spectrum) and Ni nitride (red spectrum) surfaces. The black arrow indicates the Ni nitride binding energy. Photon energy $h\nu = 1253.6$ eV.

centered at 397.15 eV, which is the binding energy assigned in the literature to N atoms in a nitride-like coordination with the Ni surface atoms [27, 109].

In order to rule out the possibility that the molecules are still intact on the surface, we performed UPS measurements. The UV light, probing the valence bands, is more sensitive to the sample surface, thus unambiguously detecting the presence of molecular states on the Ni surface. As it is reported in Figure 4.4, no molecular states were detected on the surface after several doping cycles with different exposure times. Indeed, the spectra after exposure do not show significant changes with respect to the clean Ni spectrum, confirming the absence of intact molecules on the surface and the cracking of the 2H-TTP molecules.

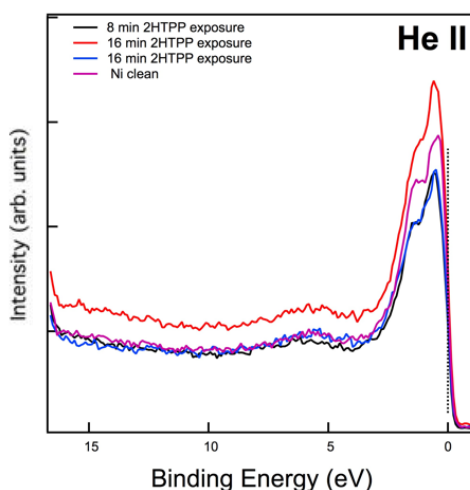


Figure 4.4: UPS spectra of Ni clean and several cycles of exposure to 2H-TTP.

In order to increase the amount of nitrogen in the bulk and to assess its capability to withstand several cleaning cycles, we repeated the doping procedure many times, observing a progressive increase in the intensity of the Ni nitride peak in the N $1s$ spectra [131].

Finally, in order to confirm the presence of a N reservoir in the Ni bulk and to investigate the effect of a standard cleaning procedure, several cycles of sputtering and annealing were performed. After these cycles, no detectable signal of Ni nitride was visible in the spectra, which resemble the clean profile in black of Figure 4.3, confirming the cleanliness of the Ni surface. However, we did not remove all nitrogen from the Ni crystal because nitrogen was detected again after graphene growths. It segregates back to the surface and it is trapped as pyridinic or graphitic species in the graphene mesh, confirming the successful N doping procedure of the Ni crystal.

In a second step, the standard LP-CVD graphene growth was carried out, as sketched in Figure 4.5.

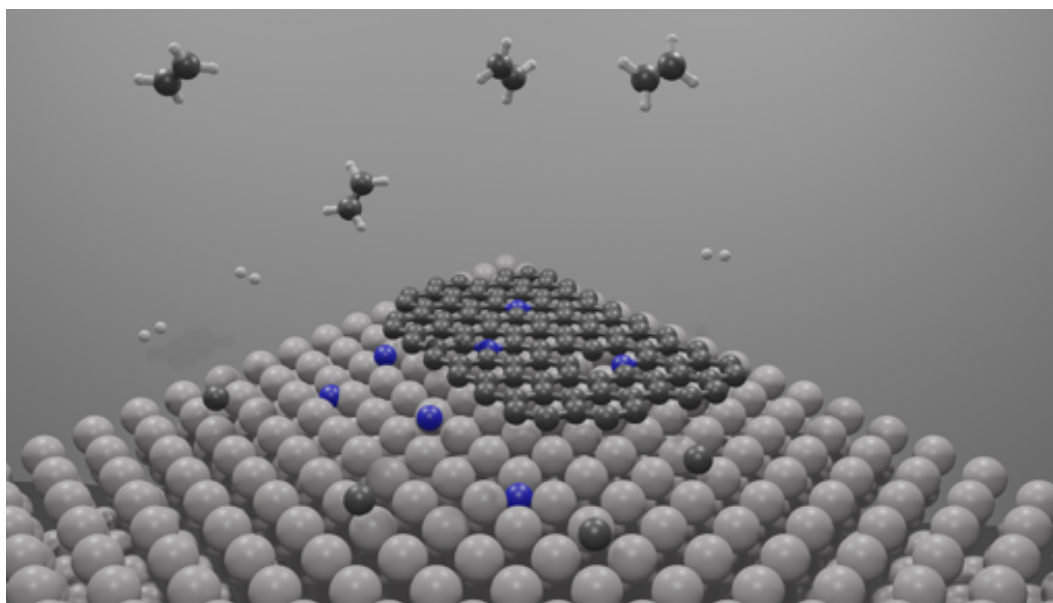


Figure 4.5: Schematic representation of the N-doped Gr growth: the previously N contaminated Ni substrate was exposed to ethylene, obtaining N-doped Gr.

In order to obtain high-quality graphene, ethylene (C_2H_4) was used as C-containing precursor. The recipe adopted was the same reported in chapter 2, section 2.5.1 aimed at obtaining a complete, flat and homogeneous monolayer of graphene on the Ni(111) substrate.

XPS and STM measurements, performed after the first CVD cycles, revealed a significant amount of nitride below the graphene layer (see section 4.5). Only after several cycles of cleaning and growth, the presence of Ni nitride was reduced, thus having N mainly in the graphene network.

4.2 N-doped Graphene: epitaxial domains

The chemical and morphological characterization of the N-doped graphene layer was carried out by means of LEED, XPS and STM/STS measurements, corroborated by a detailed DFT investigation and simulations of STM images and STS maps. LEED and XPS measurements were performed at room temperature (RT), while STM experiments were carried out at both room and cryogenic (liquid nitrogen temperature, 77 K) temperatures. The electronic states and the surface morphology of N-doped graphene will be described in detail

in the following sections.

After the growth, performed as reported in the previous section, LEED measurements allowed us to investigate the long-range order of the surface structure, comparing it with that obtained for pristine graphene on Ni(111). In Figure 4.6a, a typical LEED pattern of a pristine graphene is reported, where a (1×1) structure is well-defined, indicating the growth of mainly epitaxial graphene domains on the Ni surface (see chapter 2, section 2.5.1).

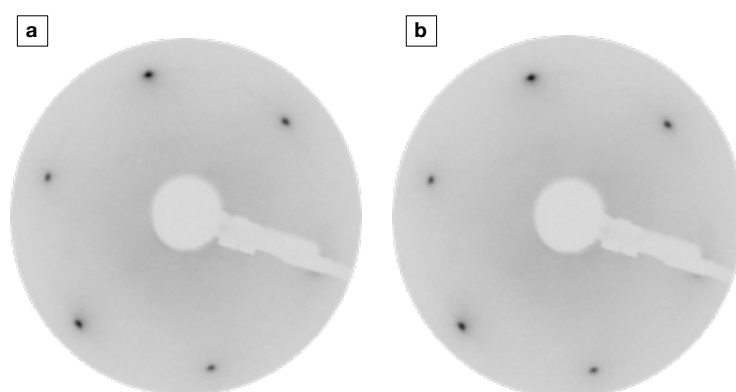


Figure 4.6: LEED patterns of (a) pristine graphene and (b) N-doped graphene on Ni(111). ($E=70$ eV).

The LEED pattern reported in Figure 4.6b, was instead acquired after the growth of N-doped graphene on Ni(111). As clearly visible, the same structure observed in the pristine case was detected. Furthermore, the shape and the intensity of the diffraction spots and the lack of additional extra spots indicate that the quality of the graphene layer is unchanged with respect to the pristine case. This experimental evidence provides a first hint that the adopted growth protocol does not affect the configuration of the resulting layer, leading in both cases to well-ordered epitaxial graphene.

In order to investigate the quality of the graphene layer and the potential presence of N dopants trapped in the network, XPS measurements were performed. Indeed, this technique allows confirming the presence of N atoms on the surface and identifying their chemical configuration. In Figure 4.7, XPS spectra of C $1s$ and N $1s$ core levels regions are reported.

The C $1s$ spectrum reported in Figure 4.7a shows a peak centered at 284.6 eV. The data fitting indicates that there is mainly one C configuration present on the surface. In particular, the binding energy at which the main component is centered (284.6 eV) is very close to that assigned in literature to graphene strongly interacting with the Ni substrate (284.8 eV) [56, 100]; two other components were added to the fit in order to reproduce properly the experimental data: C of weakly interacting rotated graphene (284.4 eV) and Ni carbide underneath (283.2 eV). However, as expected from the LEED pattern in Figure 4.6b, their contribution is very small.

In Figure 4.7b, the typical XPS spectrum measured in the N $1s$ region after several CVD cycles is reported. The presence of several components indicates the co-existence of different chemical N configurations. The best fit of the experimental XPS data in the N $1s$ region was obtained using a Shirley background and two Doniach-Sunjic peaks, with binding energies converging to 398.6 ± 0.15 eV and 400.6 ± 0.15 eV.

A complex picture regarding the binding energies of N defects in a graphene overlayer

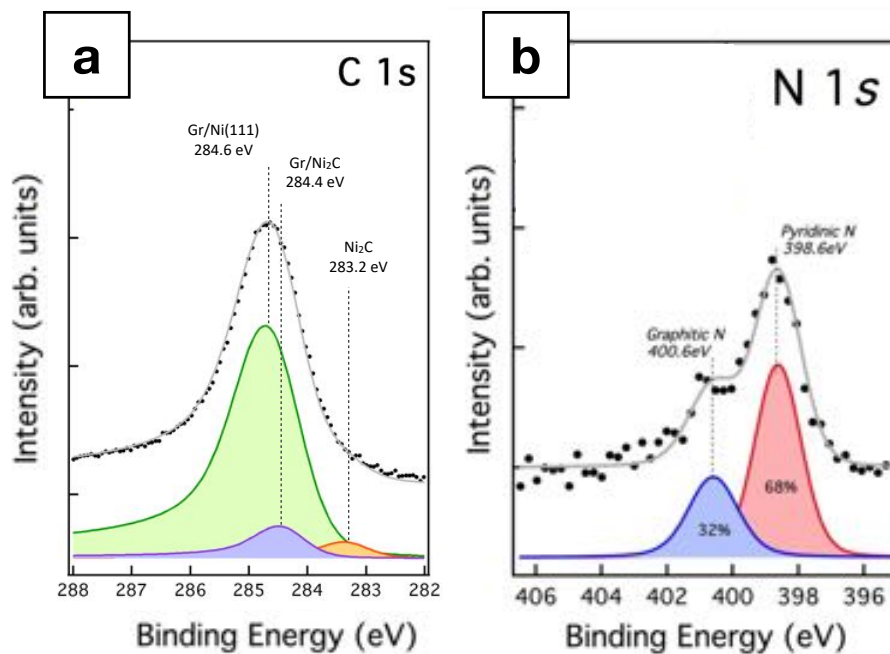


Figure 4.7: XPS spectra of (a) C $1s$ and (b) N $1s$. The C $1s$ main peak is centered at 284.6 eV, slightly lower than the reference value reported in literature for graphene on Ni (284.8 eV). Two other components related to Ni carbide and graphene on Ni carbide were added to fit properly the experimental data. The N $1s$ peak appears formed by two components centered at different binding energies: (i) 398.6 eV, associated to the pyridinic N configuration, and (ii) 400.6 eV, associated to the graphitic N structure. Photon energy: (a) $h\nu = 1253.6$ eV, (b) $h\nu = 1486.7$ eV.

exists in the literature: the pyridinic defects are found in the 397.8 eV - 401.8 eV binding energy range (depending on the N coordination and the possible presence of adsorbates), while the graphitic defects are found in the 400.2 eV - 401.8 eV energy range [27, 148, 109]. Pyrrolic defects are generally found in the energy range 400.1 eV - 400.5 eV [27], lying in the same energy region of the graphitic ones. However, on the basis of an in-depth STM analysis - presented in detail in the following sections - we rule out the presence of the pyrrolic nitrogen configuration.

Based on literature binding energies and the STM analysis, the data fitting allowed distinguishing these two N species in our spectrum:

- (i) pyridinic defects (398.6 eV), where N is placed at the edge of a C vacancy and bonds to two C atoms as part of a six-membered ring;
- (ii) graphitic defects (400.6 eV), where N atom is substituting a C atom in the graphene network and bonds to three neighbouring carbon atoms.

The two components are a clear indication that N atoms are trapped in the graphene mesh.

This assignment is confirmed by DFT calculations: the spectral separation calculated between the graphitic and pyridinic defects in graphene on Ni(111) is about 2.1 eV, in very good agreement with the experimental value of 2.0 eV [131].

The ratio between the intensities of the pyridinic and graphitic N components, obtained from the spectrum reported in Figure 4.7b, is roughly 2:1, indicating an higher amount of pyridinic N dopants with respect to the graphitic ones.

Finally, the intensity of the total N *1s* peak compared to the C signal intensity suggests that the amount of nitrogen trapped in the network is very small (few percent, ~1-2%), thus comparable to that obtained with other growth methods [27, 109, 110]. Therefore, a small doping effect on the graphene electronic bands is expected.

Nitrogen is predicted to dope graphene inducing n-type doping when N is in a graphitic configuration, or p-type doping when pyridinic N defects are formed, thus shifting the C *1s* peak toward higher or lower binding energies, respectively (see chapter 2, section 2.3.1). In our case, we have a mixture of the two N dopant structures and probably this prevents a clear predominance of one kind of doping.

Based on the XPS ratio between the two nitrogen configuration components (~2:1) and thus the higher abundance of pyridinic N with respect to graphitic defects, we expect a p-doping effect. Indeed, the C *1s* spectrum reported in Figure 4.7a appears slightly shifted towards lower binding energies (284.6 eV) with respect to the reference value reported in literature for graphene on Ni(111) (284.8 eV). Due to the high stability of the experimental apparatus formed by stable components (electron energy analyzer and photon source, Mg K_{α}), we rule out the possibility that the shift is related to an artifact. Moreover, it is important to note that the experimental resolution of 0.8 eV can introduce mainly an enlargement of the peaks but not a shift. Furthermore, the error bar of the data fitting of 0.05 eV allows us to validate the hypothesis of a real shift of the peak due to the presence of N doping in the graphene network.

The surface morphology was investigated by means of STM, performed at room and cryogenic temperature. The atomic resolution achieved allowed us to identify several structures embedded in the graphene network, each one characterized in detail, both experimentally and theoretically.

In Figure 4.8, a 15×15 nm² overview of the graphene layer acquired at 77 K is reported. The STM image confirms that a graphene layer of good morphological quality was obtained: the surface appears flat and regular, as normally observed for graphene grown epitaxially on the Ni(111) substrate. Not all the atoms of the hexagon are visible, due to the strong interaction at the interface between graphene and its substrate. Indeed, by

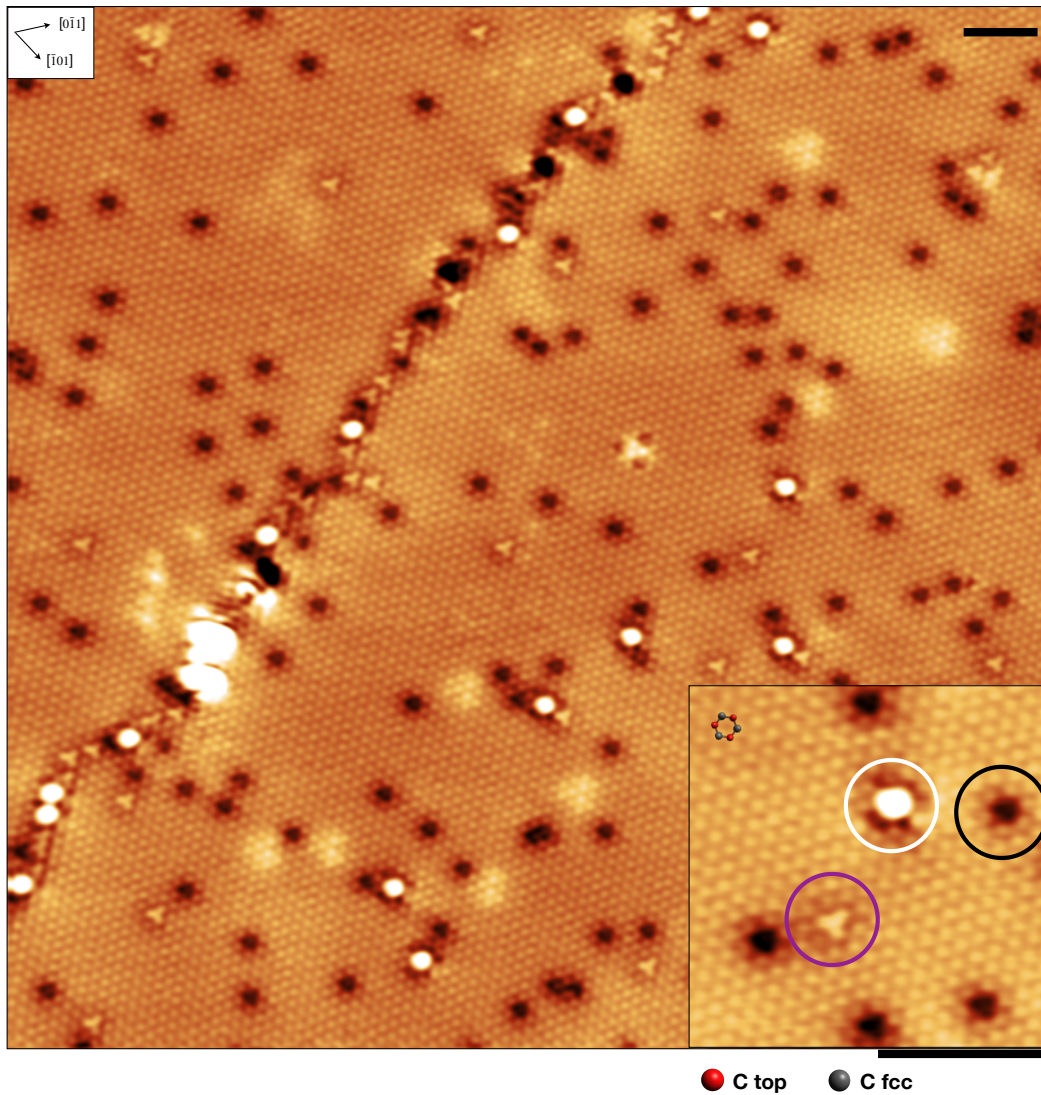


Figure 4.8: LT-STM image acquired at 77 K. Several defects are present on the surface. In the inset, the three most abundant types of defects are visualized. Ni adatoms, also present in pristine graphene, are encircled in white. New kinds of defect, not present in the pristine case, are visible (encircled in black and purple), tentatively associated to N atoms trapped in the graphene mesh. Scale bars: 2 nm, $I = 2.0$ nA, $V_{\text{bias}} = -0.2$ V.

STM, under typical imaging conditions, only one graphene sublattice is visible for epitaxial graphene on Ni(111) [107]. This means that, instead of visualizing a honeycomb structure, a prominent triangular lattice is imaged. This symmetry breaking is due to the two different adsorption sites of the carbon atoms on the Ni(111) substrate, namely hollow and top sites, as explained in chapter 2, section 2.5.1. In particular, the carbon atoms located above hollow sites (Ni fcc sites) are imaged brighter while the carbon atoms on top sites are less bright. Based on the Ni crystal orientation as revealed by LEED and STM, we assigned this arrangement to the top-fcc registry, on which we based all our experimental and theoretical analysis.

In Figure 4.8, a grain boundary is visible, separating two regions that have the same top-fcc geometry. This confirms that the graphene layer was formed on the surface starting from different seeds that, during the growth, have given rise to distinct graphene domains. This is totally analogous to the case of pristine graphene, thus validating that the N doping method presented in this thesis does not affect significantly the standard epitaxial graphene growth process, as suggested by LEED and XPS measurements.

The graphene surface appears sprinkled by a huge number of defects with diverse appearance. The large white spots, clearly visible in Figure 4.8 and in its inset (white circle), are observed also in the pristine case and were previously assigned to Ni atoms trapped in the graphene network during the growth process [65, 149]. Indeed, it was experimentally and theoretically demonstrated that Ni surface adatoms actively participate in the LP-CVD graphene growth process, catalyzing the C-C bond formation [65] and remaining at times trapped into the graphene network [149]. Besides the trapped Ni adatoms, new kinds of defects were observed in the large scale high-resolution images, not present in the pristine graphene case, that can be tentatively linked to N atoms trapped in the graphene mesh. The inset reported in Figure 4.8 shows a magnification of two of the most abundant features of this kind, appearing as clover-like defects (purple circle) and dark triangles (black circles).

The high-resolution STM measurements allowed for a detailed investigation of the different types of defects, characterized by peculiar appearance, shape and size. DFT calculations revealed that these features are clearly reproduced by embedding N atoms inside the graphene lattice, arranged in different configurations.

4.2.1 Most abundant N defects

Atomically resolved images of the most abundant N defects observed are reported in the top row of Figure 4.9. For the defects in panels 4.9a and 4.9b, the graphene network appears to be complete, with no vacancies in the mesh. This points to the presence of N atoms fully embedded in the graphene network, where they replace C atoms in a graphitic configuration, in line with the XPS results discussed above. The clover-like defect (Figure 4.9a) is centered in a top site, with the first fcc neighbouring C atoms appearing brighter than the other C atoms of the mesh, thus suggesting a localized increase in the density of states. Instead, in the case of the defect centered in a fcc position (Figure 4.9b), a localized intensity decrease is present at the position of the first neighbors of the central atom, accompanied by the appearance of brighter clovers formed by second and fourth neighbor C atoms in symmetric positions. Considering their registry, we assign these two defects to top (4.9a) and fcc (4.9b) graphitic N configurations, respectively. This identification is confirmed by DFT calculations and simulated STM images of the proposed models (Figure 4.9, second row in the top panel), which nicely reproduce the appearance of these defects. At variance with Figure 4.9a and b, Figure 4.9c and d show images characterized by a dark core, suggesting that the corresponding defects involve one or more atomic vacancies in the network.

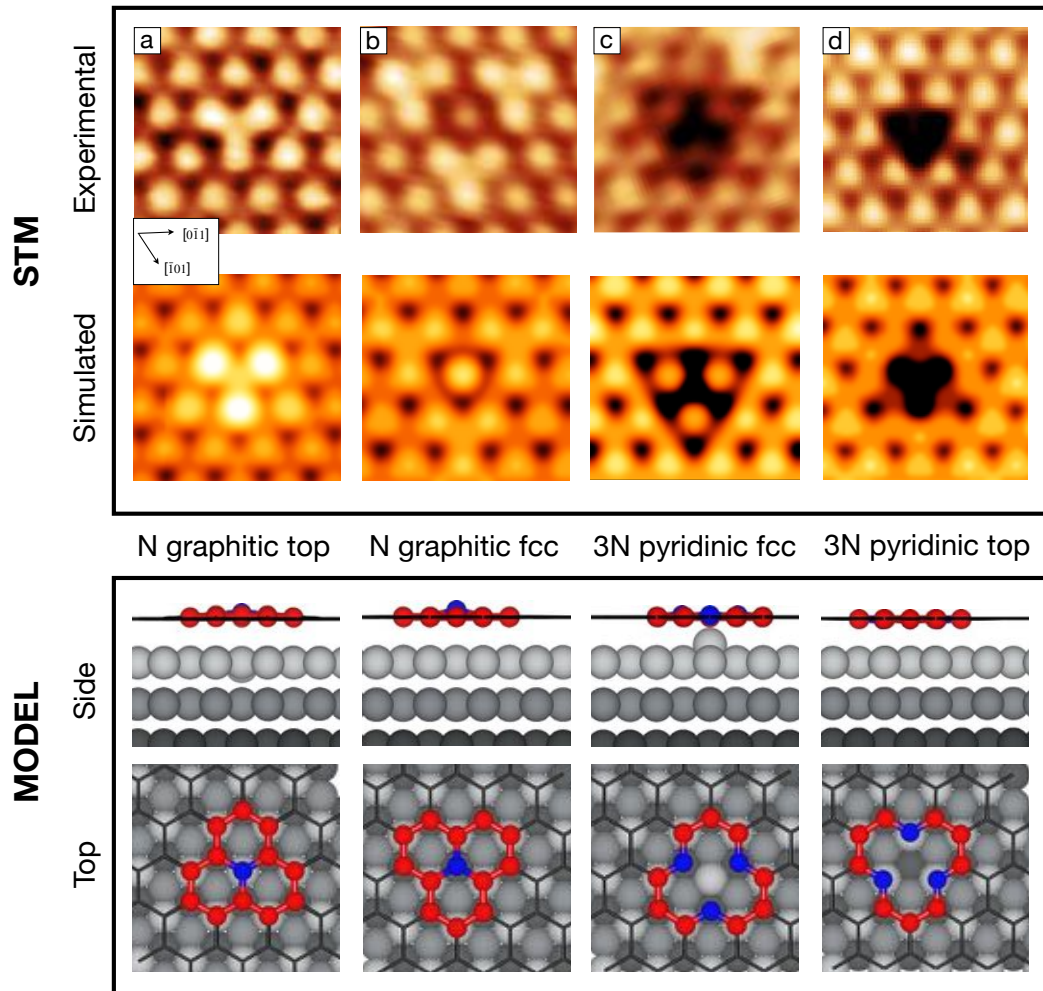


Figure 4.9: N defect configurations in Gr on Ni(111). Top panel: Experimental and simulated STM images for various defects. Image size: $1 \times 1 \text{ nm}^2$. Structures are classified according to number of N atoms, configuration type and position. Experimental parameters: (a) N graphitic top, $I = 3 \text{ nA}$, $V_{\text{bias}} = -0.2 \text{ V}$, (b) N graphitic fcc, $I = 4 \text{ nA}$, $V_{\text{bias}} = -0.2 \text{ V}$, (c) 3 N pyridinic fcc, $I = 0.6 \text{ nA}$, $V_{\text{bias}} = -0.2 \text{ V}$ and (d) 3 N pyridinic top, $I = 0.6 \text{ nA}$, $V_{\text{bias}} = -0.2 \text{ V}$. Computational parameters: $V_{\text{bias}} = -0.2 \text{ V}$; ILDOS isosurface lying $\approx 2 \text{ \AA}$ above graphene and with ILDOS value of $5 \times 10^{-5} |e|/a_0^3$. Bottom panel: ball-and-stick model of DFT relaxed structures (side and top view).

More specifically, the defects imaged in Figure 4.9c and d display a threefold symmetric shape, centered in top and fcc positions, respectively. In Figure 4.9c, the down-pointing black triangle shows three protrusions in fcc position close to the corners, with a slightly less bright appearance than C atoms in the network; conversely, the triangular defect in Figure 4.9d displays a completely black core. Due to the likely presence of vacancies, it is reasonable to expect that these two defects involve nitrogen in pyridinic structures. The comparison between the experimental STM images and those obtained from an extensive DFT investigation leads to the following assignment: the defects in Figure 4.9c and 4.9d are compatible with a threefold symmetric pyridinic configuration of three N atoms in fcc and top positions, respectively. These 3N pyridinic models consist of three N atoms, each bound to two C atoms, at the edge of a C vacancy, as it is illustrated in the corresponding ball-and-stick model reported in the bottom panels in Figure 4.9.

The presence of pyridinic species in the N-doped graphene layer is fully consistent with the XPS measurements reported and discussed above. In particular, the 3 N pyridinic top configuration is the one that best fits the experimentally observed XPS shift with respect to the graphitic top species (calc. 2.1 eV) [131], as mentioned above.

A direct quantitative comparison between the amounts of 3 N pyridinic and graphitic defects measured by XPS and STM is not trivial, as we could not perform *in situ* XPS measurements on the same layers imaged by STM. In any case, both techniques agree in indicating that the amount of N atoms in pyridinic configuration exceeds that in graphitic configurations. However, STM on average estimates the presence of more than twice pyridinic N than XPS, but the reason of this discrepancy remains unclear and might be related to the different distribution of defects at the grain boundaries, to the influence of the different history of the measured layers and/or to effects such as photo-electron diffraction on the spectroscopic measurements.

We further characterized the electronic structure of the observed N defects by acquiring STM images at different bias voltages. This allows the empty and filled states near the Fermi level to be probed. The comparison between the experimental and the simulated STM images is reported in Figure 4.10, showing a good agreement for N graphitic top and fcc defects, as well as for the 3N pyridinic fcc defect, both at negative and positive biases. In the case of the 3N pyridinic top, the simulated image did not adequately reproduce the experimental features for positive bias polarity. Indeed, in this case simulated STM images show a dark core at all the considered biases (negative and positive), while the experimental images display a dark core only at negative biases and a bright protrusion at positive ones. We still do not have a clear explanation for this effect; it can be tentatively related to an enhancement of the inelastic scattering of tunneling electrons due to vibrational excitations of possible adsorbates on the tip, when the tip is located on specific defects, such as the 3 N pyridinic with an fcc vacancy, as previously reported in literature [150], or to the specific theoretical method, the Tersoff-Hamann approach, used for the simulations. In particular, in the Tersoff-Hamann approach [122], the shape of the simulated tip is spherical, thus only the s orbitals are considered and the possible p orbitals involved are neglected. This might affect the resulting calculations and simulations, producing unreal features, not in agreement with experiments.

To further corroborate our assignment based on the good agreement between experimental and calculated XPS shifts and STM images at negative bias, and to shed light on the discrepancy between theoretical and experimental imaging at positive bias, we have performed STS maps at cryogenic temperature (77 K) to locally probe the spatial distribution of the density of states around defects [124]. The cryogenic temperature allows the tip to be stable and sharp on a longer time, reducing artifacts due to atoms rearrangement

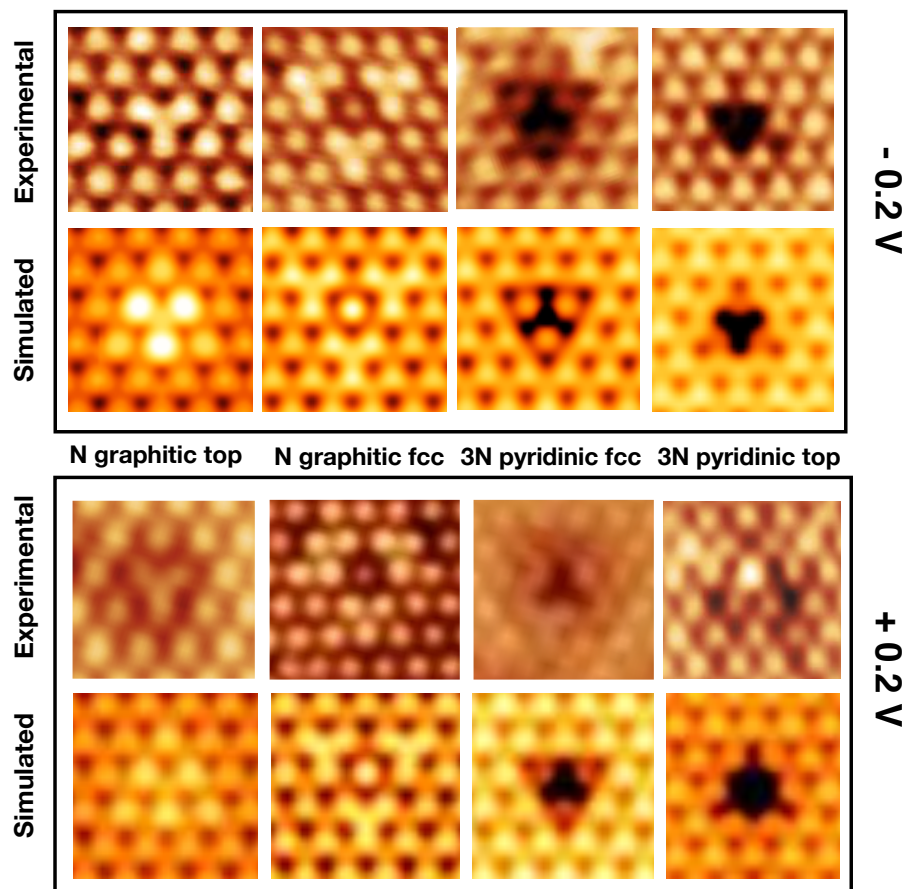


Figure 4.10: Experimental and simulated STM images of the N graphitic and 3N pyridinic configurations in top and fcc positions at negative (-0.2 V) and positive (+0.2 V) biases.

on the tip or thermal drift.

In Figure 4.11, the experimental results at ± 0.2 V are compared to the simulated STS maps at the same biases for N graphitic (top and fcc) and 3N pyridinic top. In particular, ex-

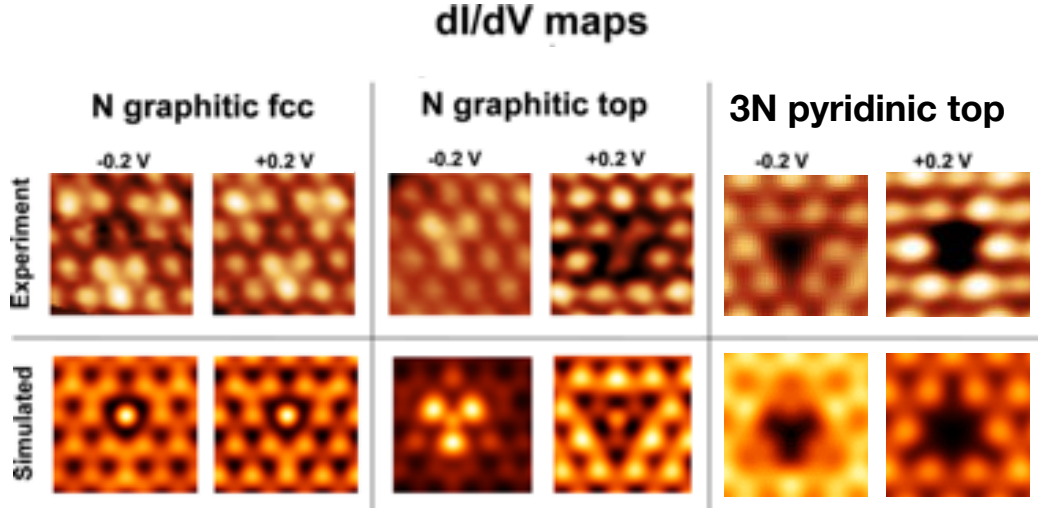


Figure 4.11: Experimental and simulated STS dI/dV conductance maps at constant height of the 1N graphitic fcc, 1N graphitic top and 3N pyridinic top defects, for two different biases, -0.2 V and $+0.2$ V. Simulation parameters: LDOS iso-surface with a constant height of 2 \AA above graphene. Experimental setpoint parameters: N graphitic fcc $I_0 = 3.0 \text{ nA}$, $V_{\text{bias}} = \pm 0.2 \text{ V}$, N graphitic top $I_0 = 4.0 \text{ nA}$, 3N pyridinic top $I_0 = 4.0 \text{ nA}$, $V_{\text{bias}} = \pm 0.2 \text{ V}$. Lock-in parameters: Modulation amplitude = 16 mV , Frequency = 971.5 Hz .

perimental constant-height dI/dV conductance maps of graphitic defects in top and fcc positions, acquired at two different biases (± 0.2 V), nicely match the corresponding maps of LDOS, providing further support to our interpretation about the nature of the observed N defects.

For the 3N pyridinic top configuration, a dark core was experimentally imaged in the dI/dV maps at both positive and negative biases (± 0.2 V), as it is shown in Figure 4.11, which in this case is in agreement with the simulated STS maps. To find a possible explanation for the discrepancy between theoretical and experimental STM imaging at positive polarity, we probed the empty and filled states very close to the Fermi level, mapping at ± 0.05 and ± 0.1 V and comparing the experimental results with the STS simulated maps at the same biases. In Figure 4.12, the obtained maps are reported, showing a good agreement at ± 0.1 V and -0.05 V. The discrepancy was observed again very close to Fermi, more clearly at positive bias values ($+0.05$ V), where it is visible an enhancement of the brightness at the center of the defect, thus suggesting the presence of a state very close to the Fermi level. Nevertheless, our statistics is not high enough to confirm this observation. It is also important to consider that the high atomic resolution might be ascribed to a functionalized tip, which can introduce artifacts in the experimental maps, causing an enhancement of inelastic scattering of electrons. It is well known [150] that at biases very low in magnitude the electron tunneling current can flow also inelastically through vibrational states of molecules that sit on the tip. Such effect, that in principle occurs everywhere on scanned surface, might be enhanced by the particular conformation of the defect: at the center, where no atom sits, the tunnelling current could flow also on the side of the tip through the N dangling bonds, thus changing the matrix element that describes the tip-sample tunnelling process and giving raise to extra features in STM images and STS maps. This effect

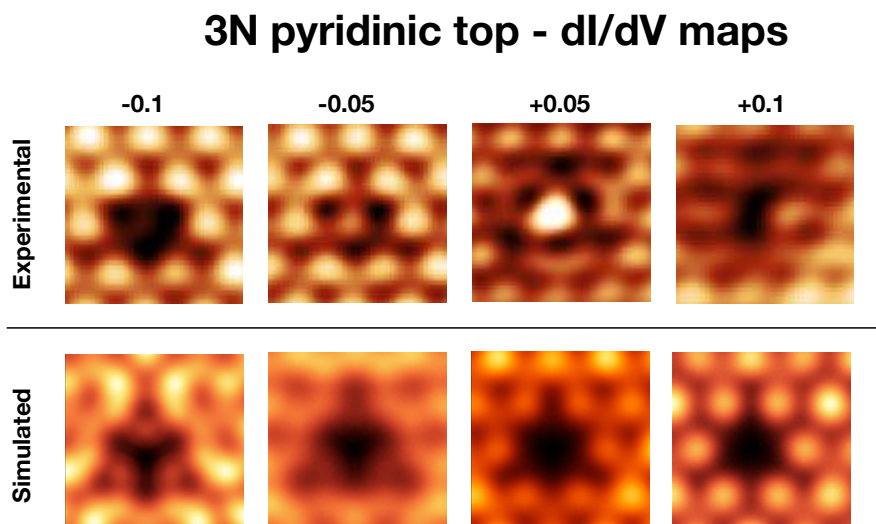


Figure 4.12: Experimental and simulated STS dI/dV conductance maps at constant height of the 3N pyridinic top defect, for several different biases near the Fermi level, ± 0.05 and ± 0.1 V. Simulation parameters: LDOS iso-surface with a constant height of 2 \AA above graphene. Experimental starting parameters: 3N pyridinic top $I_0 = 4.0 \text{ nA}$, $V_{\text{bias}} = \pm 0.05, \pm 0.1 \text{ V}$. Lock-in parameters: Modulation amplitude = 16 mV , Frequency = 971.5 Hz .

is not considered in theoretical calculations.

Finally, we demonstrated that these N dopant structures have the same appearance at a given bias and for different tip conditions and are stable at different temperatures (cryogenic, room temperature and after a flash annealing at $250 \text{ }^\circ\text{C}$), as it is reported in Figure 4.13. Indeed, the N defect structures were exactly replicated at 77 K by means of the LT-STM and at higher temperatures using the VT-STM.

It should be noted that in the above analysis we never considered pyrrolic N defects. This is due to the fact that in our STM images we never observed defects of pentagonal shape, as expected for pyrrolic N, where one N atom is part of a 5-member ring; on the other hand, the appearance of all the main N defects observed were adequately reproduced using graphitic and pyridinic configurations. On this basis we can safely assume that, although we cannot exclude the presence of some pyrrolic N defects, their coverage is not relevant.

These experimental evidences, in synergy with the DFT calculations and the simulated STM/STS data, unambiguously confirm the presence and the structure of N graphitic and 3N pyridinic defects embedded in the graphene network.

We theoretically investigated why some defects are more abundant and other more rare. In particular, the following two facts are worth noting: (i) although 3N pyridinic configurations are the most abundant in the network, pyridinic configurations with 2N top, 1N top and 1N fcc, are never observed in our experimental STM images of the N-doped graphene layer, and (ii) other defects, which we will present in the following sections, are rare or very rare.

In order to shed light on this experimental evidence, in collaboration with the University of Milano-Bicocca, we performed a set of DFT calculations aimed at evaluating the energy cost/gain of having N atoms at either pyridinic or graphitic positions in the lattice. We compared the total energy of three model configurations with the same number of N atoms (3 N) but different relative positions (see Figure 4.14).

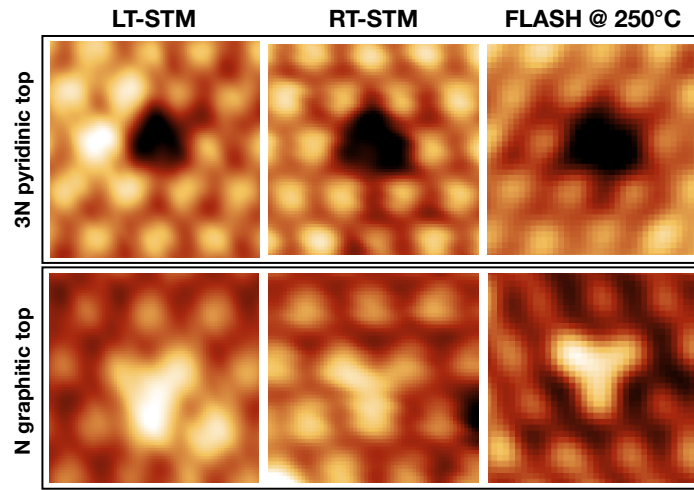


Figure 4.13: STM images of the two most abundant N defects (N graphitic top and 3N pyridinic top) at cryogenic (77K), room temperature and after a flash annealing at 250 °C. $V_{\text{bias}} = -0.2$ V.

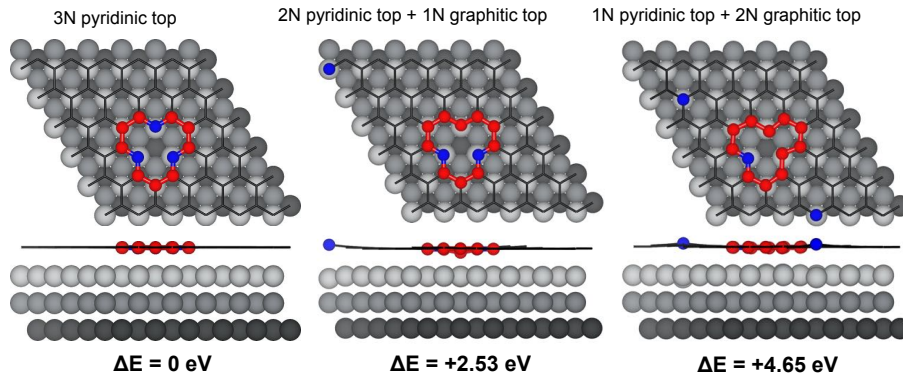


Figure 4.14: Top and side views of three different N-doped graphene models involving 3 nitrogen atoms, classified according to the configuration type and position of the N atoms. The relative energy with respect to the most stable model (3N pyridinic top) is reported below each configuration. Color coding: Ni atoms in the first, second and third layer are rendered in dark grey, grey and light grey, respectively; N atoms in blue; C atoms delimiting the defect site in red, graphene network in black.

The most stable model (3 N pyridinic top) is taken as energy reference. Both the other tested structures ("2 N pyridinic top+1 N graphitic top" and "1 N pyridinic top+2 N graphitic top") are characterized by higher total energies, +2.5 eV and +4.6 eV, respectively. This is a clear indication of the preference for the N atoms to be located at the edges of the C vacancy site rather than elsewhere, replacing a C atom within the graphene matrix, which explains the experimentally observed higher abundance of pyridinic defects with respect to graphitic ones. Such balance is likely related to the doping technique: adding N atoms during growth favors the dynamic selection of defects with lower energy, with no constraint posed by the local abundance of N atoms required. Conversely, other doping techniques such as post-growth ion implantation favour defects with a different graphitic/pyridinic ratio, as a consequence of the ballistic formation process [27, 151].

4.2.2 Rare N defects

So far, the most abundant N configurations have been analyzed in details but, as it is visible in Figure 4.8, other, more rare, kinds of defects are present on the graphene surface, thus suggesting the presence of additional possible N defect structures. For instance, in principle, the pyridinic configuration with one C vacancy can involve a number of nitrogen atoms ranging between 1 and 3, each of them located in top or fcc sites. Moreover, other exotic structures, like for example multiple vacancies or pairs of nitrogen atoms embedded in the network, cannot be *a priori* ruled out.

Based on our huge statistics obtained by a thorough STM investigation, we present here more rare experimentally observed structures, and compare them with a wide variety of possible theoretical models, involving different numbers of C vacancies and N atoms, placed in different positions of the graphene network, at the interface with the Ni substrate and/or interstitially embedded in its first layers.

In Figure 4.15, rare defects embedded in the graphene network are presented. All of the reported defects are rare or very rare and their structure is suggested on the basis of a reasonable comparison with theory. In Figure 4.15a, the imaged defect displays a mirror symmetry with a dark core, suggesting that one or more atomic vacancies are involved. On the other hand, the defect imaged in Figure 4.15b displays a complete mesh where an atom placed in fcc position appears brighter than all the others. Having already assigned the N graphitic fcc configuration with an high level of confidence, a different arrangement of the nitrogen atoms must be found for this defect. Similarly to the 3N pyridinic defect, the configuration in Figure 4.15c shows a dark core with a "shadow" in the center and two brighter atoms on one side of the dark triangle. Finally, a bigger dark triangular structure is imaged in Figure 4.15d, suggesting a multiatomic C vacancy.

The comparison between the experimental STM images and those obtained from a thorough DFT investigation results in the following assignment (see bottom panels in Figure 4.15): the defect in Figure 4.15a is compatible with a 2N pyridinic fcc configuration with mirror symmetry, whereas the one in Figure 4.15b can be ascribed to a N atom located in between the two first layers of the Ni substrate, below a graphene carbon atom in fcc position. Instead, the configuration in panel 4.15c can be classified as a N-N pair embedded in the graphene mesh. Finally, the large defect in Figure 4.15d is remarkably well reproduced by the simulated STM image of a tetra-atomic vacancy with edges decorated by six N atoms in the top positions.

It is important to note that the structures shown in Figure 4.15b and c were always experimentally imaged in groups of three defects, thus forming a bigger triangular shape, as evident in Figure 4.15e (models in Figure 4.15f and g). We do not have a precise explanation for this peculiar behavior. Based on the results presented so far, nitrogen seems to pre-

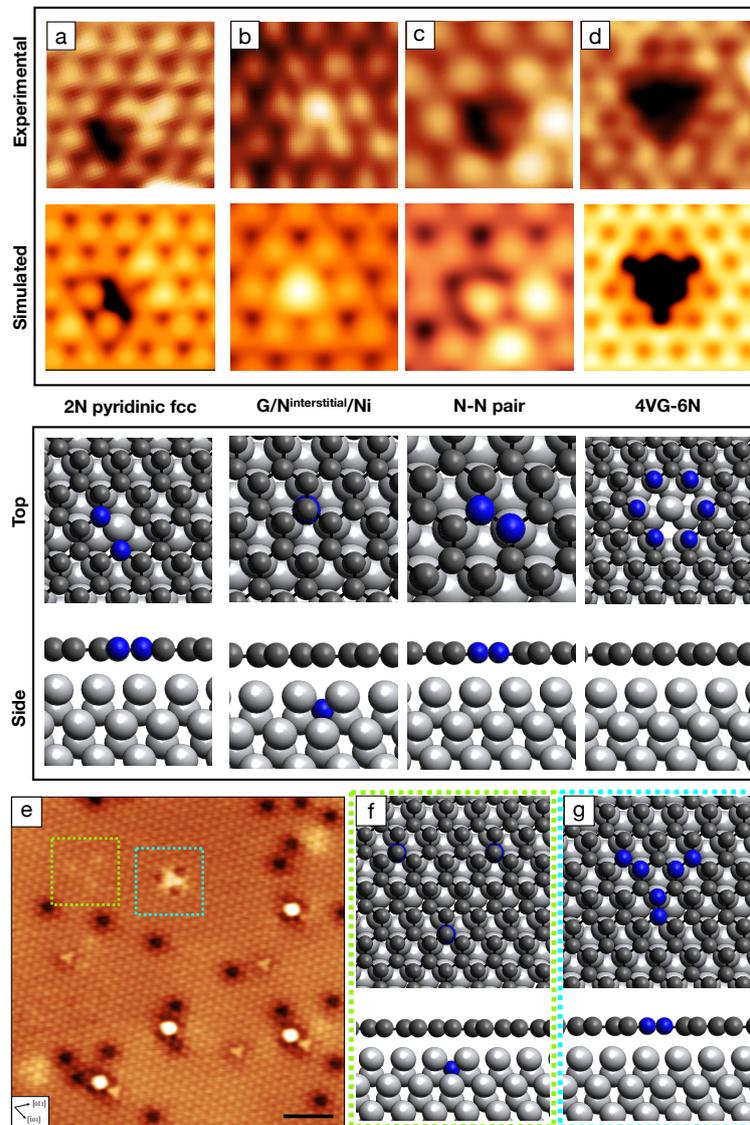


Figure 4.15: (a)-(d) Experimental and simulated STM images of N configurations rare or very rare imaged in the graphene network. $V_{\text{bias}} = -0.2$ V. (e) STM topographical image of N-doped graphene: several defects are clearly visible on the surface. Green and blue dashed circles highlight G/N^{interstitial}/Ni and N-N pair defect groups, respectively. Scale bar: 1 nm. Image parameters: $I = 8$ nA, $V_{\text{bias}} = -0.2$ V. (f), (g) Top and side view model of the group of defects inside the dashed squares in (e).

fer aggregating in groups of atoms, thus we might expect a minimization of the energy by forming groups of nitrogen atoms. However, we have to keep in mind that the final configurations observed by STM are the results of kinetic and/or thermodynamic processes, and in order to validate the previous speculations, further specific theoretical investigations should be performed.

4.3 N-doped Graphene: rotated domains

As it is well-known in literature, CVD graphene growth on a Ni(111) substrate can result into two different graphene phases: epitaxial and rotated graphene (see section 2.5.1). So far, we focused on nitrogen doping in the epitaxial graphene domains, unveiling several kinds of N defects, different in shape, size and number of N atoms involved in the structure. In this section, we will investigate the N doping sites in rotated graphene domains at the atomic level.

In a preliminary LEED characterization, comparing two diffraction patterns for pristine and N-doped graphene reported in Figure 4.16a and b respectively, no significant differences are visible in the long-range arrangement when nitrogen is added to the preparation using our protocol, as it was highlighted for the case of epitaxial graphene in the previous section (see Figure 4.6).

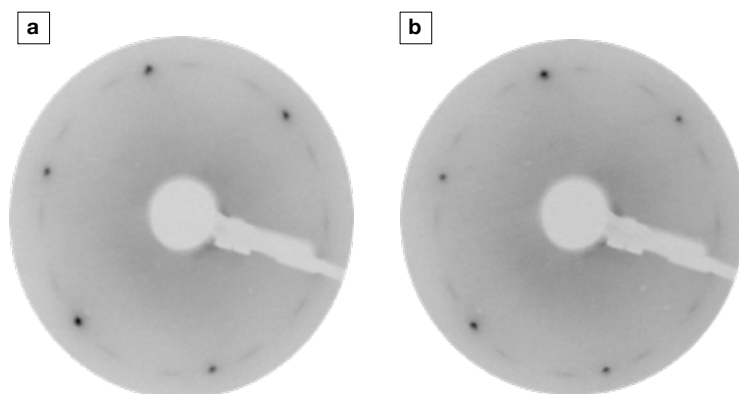


Figure 4.16: LEED patterns of (a) pristine rotated graphene and (b) N-doped rotated graphene on Ni(111). ($E=68$ eV).

The analysis of the LEED patterns allowed identifying two main features: the typical (1×1) structure of epitaxial graphene in register with the Ni substrate, and the arc-like spots expected for rotated graphene domains (more details in chapter 2, section 2.5.1). Indeed, as already reported for pristine graphene on Ni(111), the rotation angle of the graphene domains varies in a small range around 17° , creating arc-like features in the diffraction pattern.

In order to investigate the surface morphology of the sample, STM experiments at room temperature were carried out. In Figure 4.17, a 15×15 nm² overview of a rotated graphene domain is imaged. The triangular ordered arrangement of big bright spots is the typical moiré pattern originated from the superposition of two periodic layers (Ni and rotated graphene), as explained in chapter 2, section 2.5.1.

Several dark defects with different shapes and sizes are imaged in Figure 4.17, not present in the pristine rotated graphene case, which appear to be located in different moiré regions: (i) a triangular dark defect (in the black solid square) placed in a valley of the moiré

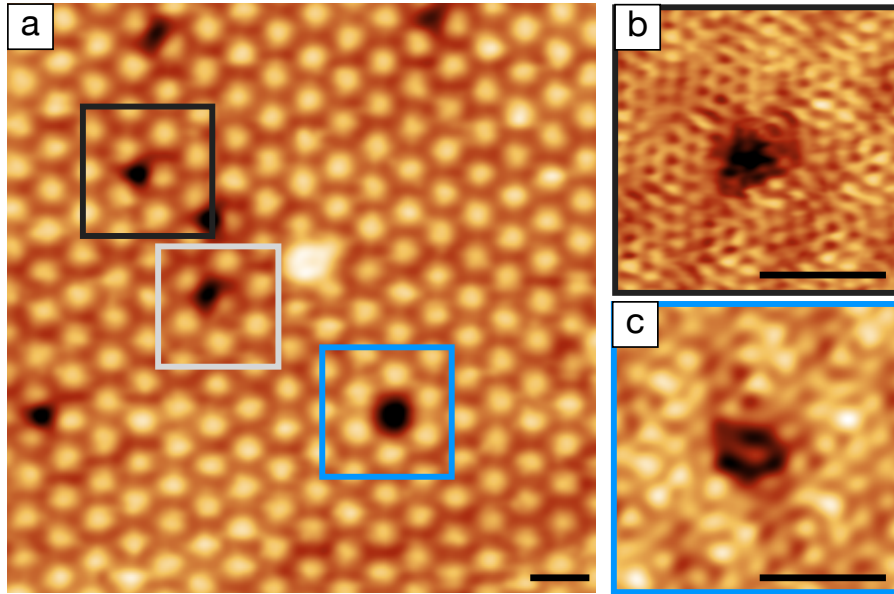


Figure 4.17: (a) VT-STM topographical image of a rotated graphene area, where the moiré pattern is clearly visible. Several dark defects are observed on the surface with different shape, size and position in the moiré pattern. Two of them are zoomed on the right, in (b) and (c). Scale bars: 2 nm. Images parameter: (a) $15 \times 15 \text{ nm}^2$, $I=0.2 \text{ nA}$, $V_{\text{bias}} = -0.4 \text{ V}$ (b) $4 \times 4 \text{ nm}^2$, $I=0.7 \text{ nA}$, $V_{\text{bias}} = -0.08 \text{ V}$ (c) $4 \times 4 \text{ nm}^2$, $I=0.09 \text{ nA}$, $V_{\text{bias}} = -0.3 \text{ V}$.

pattern, (ii) a rectangular dark defect (gray solid square) bridging two ridges, (iii) a circular dark defect (blue solid square) on a ridge. The moiré pattern determines the defects symmetry. Indeed, a threefold, mirror or hexagonal symmetry is identified for the three defects placed in different moiré positions, respectively.

From the magnifications shown in Figure 4.17b and c, the limited image resolution achieved for two of the defects do not allow to well define their configuration and thus a precise model can not be inferred. Nevertheless, by comparing the roughly triangular shape and the dark appearance of these defects in rotated domains with respect to the previously discussed 3N pyridinic configurations observed in epitaxial graphene domains, we might expect one or more vacancies in the network, tentatively assigned to pyridinic structures, also in the case of rotated graphene. Their bigger size with respect to a commonly imaged 3N pyridinic defect can be due to the presence of more than one C vacancy, as well as just one C vacancy where the three N atoms interact differently with the Ni substrate underneath, due to the rotation of the graphene domain. However, more experiments are needed to clarify the structure of these defects.

4.4 Other models for N defects

The complete characterization of the N-doped graphene layer on Ni(111) required an extensive investigation from an experimental and theoretical point of view. Despite the atomic resolution achieved and the huge statistics of the STM measurements (both at room and cryogenic temperature), the comparison between the experimental results and the simulated models was not straightforward for all defects. Indeed, in the case of N graphitic configurations, both in fcc and top position (see Figure 4.9), the agreement was actually very good, while the identification of the pyridinic defect was much more trou-

blesome.

Significant effort was dedicated to the identification of the "triangular dark defects" highlighted in Figure 4.8, and several possible models were proposed, aimed to fit the experimentally observed structure. A thorough DFT analysis, complemented by a wide number of simulated STM images, was carried out. The complete set of simulated images is reported in Figure 4.18, considering 1N pyridinic configuration both in top and fcc position (ideally, the easier structure), as well as 2N and 3N pyridinic defects. Also other models were taken into account: the possibility to have hydrogenated dangling bonds has been considered, as well as the chance of having N atoms at the interface or interstitially in the first layers of the Ni substrate. All these possibilities were evaluated, simulated and compared with the experimental results.

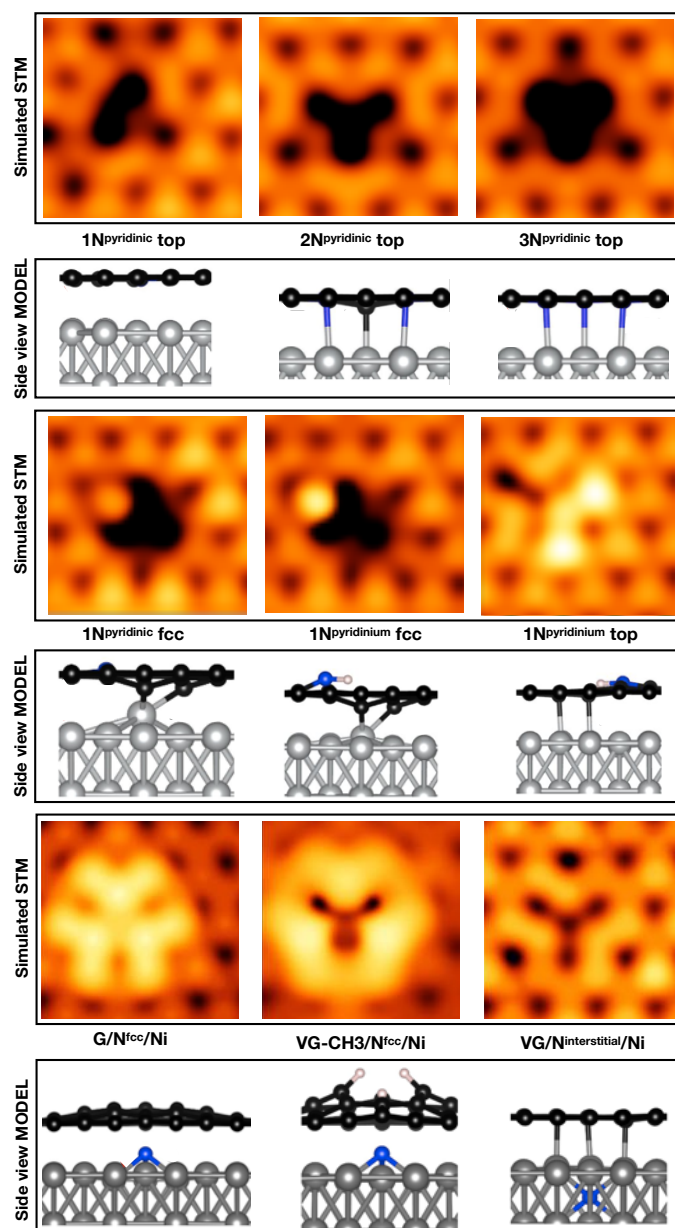


Figure 4.18: Simulated STM images and relative side view models. All the models have been simulated at $V_{\text{bias}} = -0.2$ V, corresponding to the experimental bias.

4.5 N-doped Graphene on Ni nitride

As mentioned in section 4.1, the amount of detected Ni nitride decreased after several cleaning/growth cycles. In particular, we experimentally observed a drastic reduction of nitride at the interface while keeping constant the amount and kinds of N defects trapped in the graphene network. In this section, we present the experimental LEED, XPS and STM measurements acquired just after the Ni crystal doping, showing the significant role played by nitride during the first N-doped graphene preparations.

After the standard cleaning procedure, the resulted diffraction pattern of the bare Ni substrate is shown in Figure 4.19a.

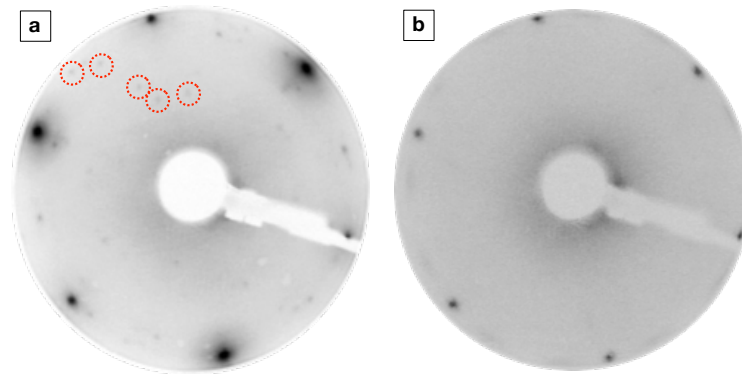


Figure 4.19: LEED patterns of (a) Ni nitride on the surface after Ni cleaning and (b) epitaxial and rotated graphene on Ni(111) after CVD. Red dotted circles indicate the extra spots. (a) $E = 68.4$ eV, (b) $E = 61.4$ eV.

Besides the expected hexagonal Ni spots, an additional complex structure is faint but visible. As reported in literature, we ascribe these extra spots to the long-range ordered structure formed by nitrogen atoms arranged in a Ni nitride-like coordination [152]. It is worth nothing that also carbon atoms in a Ni carbide coordination produce the same diffraction pattern. However, we can safely assign the diffraction pattern to Ni nitride on the basis of the XPS measurements previously discuss in section 4.1, where the main component in the N $1s$ spectrum was given by the Ni nitride-like coordination of nitrogen.

On the other hand, the LEED pattern acquired after the standard CVD graphene growth shows the typical Ni, epitaxial graphene and rotated graphene spots, without any additional complex structure (Figure 4.19b), suggesting that the majority of the nitride layer dissolved in the bulk after the graphene growth procedure.

In Figure 4.20, the reported XPS spectrum shows the measured N $1s$ signal (main plot) after just few CVD cycles; the inset at the top left shows the spectrum acquired after several cycles and already discussed in section 4.2.

Comparing the two spectra, it is possible to see the evolution of the different N configurations after few (main plot) and several (inset) CVD cycles. In both case, the presence of multiple components indicates the co-existence of different chemical N configurations and their concentrations change with CVD cycling.

At the beginning (see Figure 4.20, main spectrum), N is present in the form of (i) nickel nitride (397.1 eV), stemming from N atoms in the very first layers of the Ni substrate in a Ni nitride-like coordination, (ii) pyridinic defects (398.6 eV), where N is placed at the edge of a C vacancy and bonds to two C atoms as part of a six-membered ring, and (iii) graphitic defects (400.6 eV), where N atom is substituting a C atom in the graphene net-

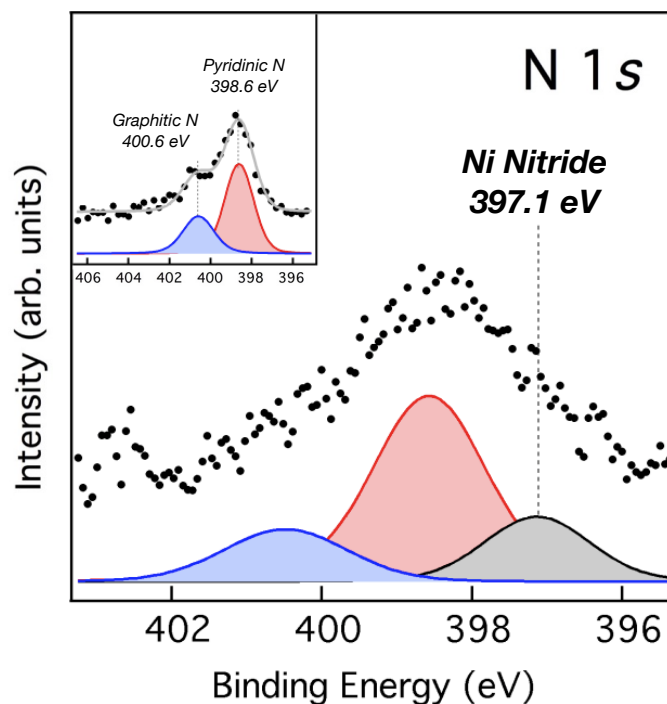


Figure 4.20: XPS spectrum of the N $1s$ core level, after few (main spectrum) and several (inset) CVD cycles. Photon energy $h\nu = 1486.7$ eV.

work and bonds to three neighboring carbon atoms. The latter two components are a clear indication that N atoms are not exclusively present in the Ni substrate, as evidenced by the lower energy component, but also trapped in the graphene mesh. However, the XPS results show that the amount of nitride in the first surface layers is significant. After several CVD cycles, the nitride-like component is not visible anymore (see inset spectrum in Figure 4.20), suggesting that the cleaning/CVD procedure has depleted the N content in the first Ni layers, while the fingerprint of N-doping of graphene is still evident (N dopants trapped in the network in form of graphitic and pyridinic defects).

Finally, STM measurements unambiguously validate the presence of nitride at the interface between N-doped graphene and the Ni substrate.

In Figure 4.21a, a 15×15 nm² image of graphene with Ni nitride underneath is imaged. The surface appears rough and irregular, completely covered by the graphene layer, as evident in the magnification shown in Figure 4.21b where the typical honeycomb lattice of graphene is visible. However, different color contrast suggests different heights on the surface, pointing out a different interaction of the graphene layer with the substrate and thus a different substrate composition at the interface. Based on XPS and LEED measurements, we speculate the presence of Ni nitride underneath graphene. Indeed, we exclude the possibility of carbide underneath graphene because graphene on top of carbide gives rise to a peculiar square moiré pattern [153], not imaged on the surface in Figure 4.21a and b.

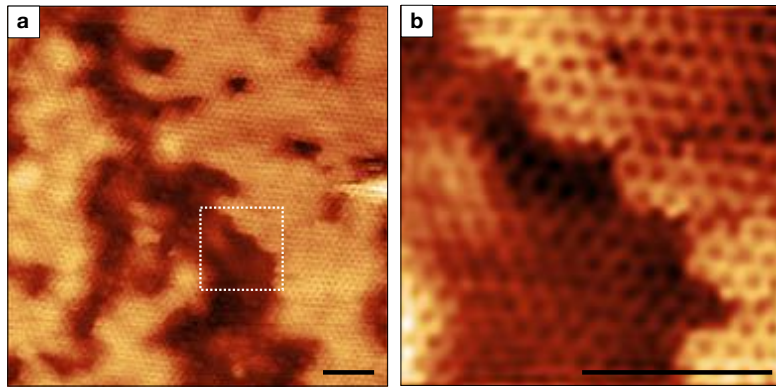


Figure 4.21: (a) STM images of graphene with Ni nitride underneath. (b) Zoom-in on the white dashed square in (a). Scale bars: 2 nm. Images parameters: (a) $I = 2$ nA, $V_{\text{bias}} = -0.2$ V; (b) $I = 0.85$ nA, $V_{\text{bias}} = -0.08$ V.

Chapter 5

Reactivity

In this chapter, a fundamental study on the interaction of one of the simplest but potentially lethal gases, namely carbon monoxide (CO), and pristine and N-doped graphene on a Ni(111) substrate is presented and discussed. The reactivity towards CO of both pristine and doped graphene is described in detail from an experimental point of view, pointing out the differences among the two systems. Numerical simulations corroborating the experimental results are also presented.

5.1 CO on pristine Graphene on Ni(111)

As discussed in chapter 2, section 2.4, the possibility to exploit graphene as gas sensor has been intensively studied in literature. In particular, CO was investigated in interaction with graphene under different experimental conditions of pressure and temperature. At low pressures ($\sim 10^{-6}/10^{-7}$ mbar of CO), graphene on Ni(111) was demonstrated to be inert at room temperature whereas at low temperature (~ 80 K) CO molecules were reported to adsorb on the graphene surface forming aligned short chains [24].

On the other hand, at pressures in the mbar regime, CO was demonstrated to intercalate at the interface between graphene and its substrate already at room temperature. For example, spectroscopic and microscopic investigations demonstrated intercalation in the confined region between graphene and Ir(111) [83] while, to the best of our knowledge, in the case of graphene on Ni(111) only spectroscopic measurements have been reported so far, where a partial intercalation was observed already at 0.1 mbar [106], as discussed in chapter 2, section 2.5.3.

In this section, we will describe and discuss our experimental results regarding the reactivity of pristine graphene on Ni(111) towards high CO pressures (in the millibar regime) at room temperature, in order to investigate the interaction process. These results will then be compared to those obtained for the reactivity of the N-doped graphene system, performed using the same experimental conditions.

5.1.1 CO intercalation at the Graphene/Ni(111) interface

As mentioned above, it is known from the literature that when pristine graphene on Ni(111) is exposed to high CO pressures, the gas molecules intercalate at the interface, reaching the confined zone between graphene and the substrate. By means of XPS measurements, this process was demonstrated to start at CO pressures around 0.1 mbar and a full intercalation was obtained at ~ 6 mbar [106]. Starting from these results, we tried to reproduce the intercalation process monitoring the spectroscopic fingerprints by XPS, in

order to then fully characterize the morphology of the sample surface by means of STM.

After the standard LP-CVD growth procedure performed as described in chapter 2, section 2.5.1, the quality, homogeneity and morphology of the graphene surface was assessed by LEED, XPS and STM.

In order to determine the pressure threshold for CO intercalation, we proceeded by exposing the sample to a gradually increasing CO pressure and characterizing it by XPS. Indeed, being sensitive to the chemical behavior of the physical system surface, this technique can quickly provide information about the interaction between CO and graphene, which induces significant modifications in the electronic structure of the graphene layer.

In Figure 5.1, the C 1s spectra of pristine graphene collected before and after exposure to 0.01 mbar and to 0.7 mbar of CO for 1 h at room temperature are reported in panels a, b and c, respectively.

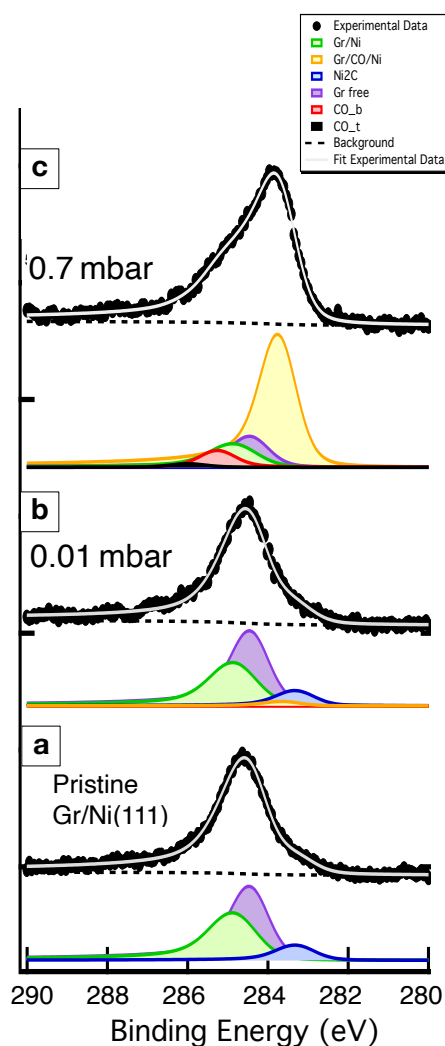


Figure 5.1: C 1s core level spectra of pristine graphene on Ni(111) (a) before the exposure to CO, (b) after the exposure to 0.01 mbar and (c) 0.7 mbar of CO for 1 h at room temperature.

In the C 1s spectrum shown in Figure 5.1a, related to pristine graphene before exposure to CO, the experimental peak appears broad, indicating different chemical environments and coordinations of C atoms on the surface. In order to properly fit the data, we used

a Shirley background and reproduced the C $1s$ photoemission peaks using asymmetric Doniach-Sunjic lineshapes (more details in section 3.3.3). Based on the data fitting and on the binding energies reported in literature for pristine graphene [100], the C $1s$ peak appears to be formed mainly by three components:

- graphene C atoms strongly interacting with the Ni substrate, whose peak is centered at 284.8 eV and labeled as "Gr/Ni" (green). This component is associated to pristine graphene on Ni(111);
- graphene C atoms belonging to the component that we label "Gr free", centered at 284.4 eV, stemming from C atoms less interacting with the substrate with respect to "Gr/Ni" and that we ascribe to rotated graphene domains with Ni₂C underneath (purple);
- C atoms coordinated with the Ni surface atoms forming nickel carbide underneath graphene, labeled "Ni₂C" and centered at 283.2 eV (blue).

After the first exposure to CO at a partial pressure of 0.01 mbar for 1 h (Figure 5.1b), the C $1s$ spectrum appears similar to the spectrum reported in Figure 5.1a, related to clean graphene before exposure to CO. This indicates that no effects have been induced on pristine graphene by CO exposure at those pressure conditions and no CO intercalation occurred.

On the other hand, in the C $1s$ spectrum measured after exposure to 0.7 mbar of CO for 1 h, a clear change was detected, as shown in panel c in Figure 5.1. In this case, two new components arise, centered at 283.6 eV (in yellow) and 285.3 eV (in red), respectively. On the basis of the data fitting and the binding energies reported in literature for CO intercalated graphene [106], the additional components were associated to:

- graphene partially decoupled from the Ni(111) surface, as indicated by the shift to lower binding energies of the graphene carbon atoms components (yellow peak at 283.6 eV),
- carbon atoms of CO adsorbed on Ni(111) in a bridge positions (red peak at 285.3 eV).

It is worth noting that, based on the literature, during the data fitting of the C $1s$ spectrum shown in Figure 5.1c, relative to the exposure to 0.7 mbar of CO, another component was introduced, ascribed to C atoms of the CO molecules adsorbed on Ni top sites. This peak, reported in black and labeled "CO_t", is almost not detectable, as was reported in Ref.[106], suggesting a preferential CO adsorption in bridge sites. The presence of CO on the Ni surface is confirmed also by the O $1s$ spectrum measured from the same preparation (see Figure 5.2). The rise of a clear peak at energy around 531.0 eV validates the hypothesis of the adsorption of CO molecules at the bridge sites of the Ni substrate [106].

By analyzing the peaks' intensity, taking into account also the attenuation due to the presence of the graphene layer, it is possible to deduce the CO coverage, obtaining an estimated coverage of 0.6 ± 0.1 ML.

LEED measurements show weak and faint additional spots in the diffraction pattern of graphene on Ni(111) after the exposure at 0.7 mbar (see Figure 5.3).

In particular, the typical hexagonally distributed (1×1) spots are related to Ni and epitaxial graphene, while the arc-like structures are due to rotated graphene domains. In addition, new extra spots are visible, forming a pattern in line with those reported in literature for CO on clean Ni(111) and compatible with the coexistence of $c(4 \times 2)$ and $(\sqrt{7} \times \sqrt{7})R19^\circ$ CO domains (nominal coverage of 0.50 ML and 0.57 ML, respectively) [118, 117]. This confirms

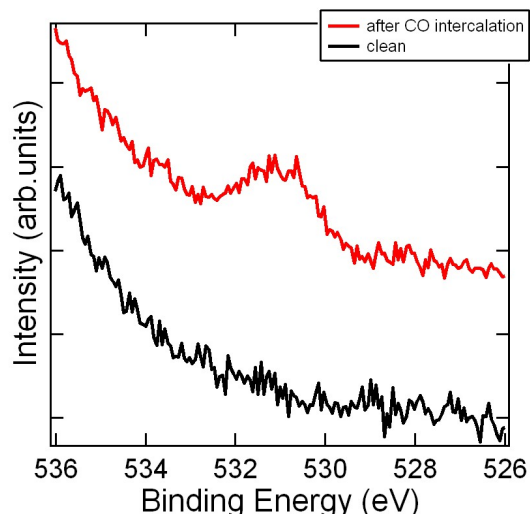


Figure 5.2: O $1s$ core level spectrum of pristine graphene on Ni(111) before (black profile) and after (red profile) CO intercalation.

that CO intercalates underneath graphene forming ordered structures with a coverage of 0.50/0.57 ML, in agreement with the estimation from the XPS data. Indeed, the possibility that in our sample CO is adsorbed on a clean Ni region (not covered by graphene) was ruled out by the experimental evidences provided by the characterization of the graphene layer before CO exposure, which confirm that the graphene layer completely covers the Ni substrate. Moreover, the weak and faint intensity of the diffraction spots suggest that CO molecules do not arrange in a single well-ordered structure all over the Ni surface. This is compatible with the coexistence of two different adsorption structures, as discussed above.

In order to rationalize the specific CO intercalation pattern and the observed effects on the electronic structure, in collaboration with a theoretical group at the University of Trieste, a systematic density functional theory investigation of pristine graphene/CO/Ni(111) was performed, relatively to the experimentally observed CO coverages of 0.50 ML and 0.57 ML. Numerical simulations demonstrated that CO intercalated molecules occupy mainly positions between hollow and bridge sites on Ni(111). For the considered coverages, stable configurations involving CO on top sites were not found, thus indicating that the graphene cover inhibits the occupation of top sites, as suggested in Ref.[106]. This validate the presence in our C $1s$ spectrum of the component we ascribed to CO in bridge positions and clarify the absence of the component related to CO on top sites.

Furthermore, to validate the spectroscopic assignment and to analyze in detail the chemical configuration of the system, the core-level shifts (CLSs) of the C $1s$ levels were calculated and compared with those computed for free-standing graphene and for graphene directly supported on Ni(111). In the case of supported graphene on Ni, an average CLS of C $1s$ of about 0.4 eV towards higher binding energies was obtained. Indeed, the calculated value of the binding energy for free-standing graphene is 284.4 eV while for graphene supported on Ni(111) is 284.8 eV, in agreement with the experimental results.

Moreover, the effect of CO intercalation on the C $1s$ core levels of graphene was studied and the CLS for C atoms in graphene and in the intercalated CO molecules were calculated, resulting strongly dependent on the CO coverage. As reported in table in Figure 5.4, a good agreement was obtained between the theoretical values and the attribution of the experimental C $1s$ peaks for graphene C atoms considered in different configurations, in

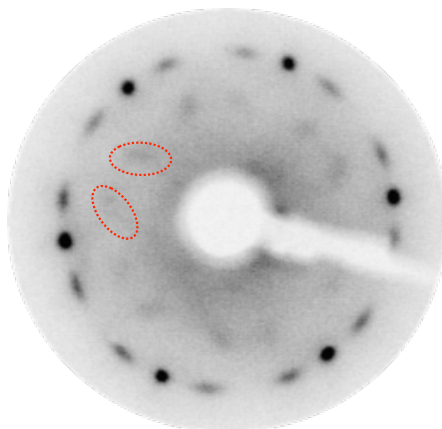


Figure 5.3: LEED patterns of pristine graphene on Ni(111) after exposure to 0.7 mbar. Red dotted shapes indicate the extra spots. ($E=102$ eV)

particular graphene C atoms directly interacting with Ni and those detached from Ni by CO intercalation. The assignment is more difficult in the binding energies region relative to CO, where the experimental spectroscopic features are broad. Here, the deconvoluted experimental peaks were tentatively assigned to CO in hollow (both fcc and hcp) and bridge sites. At even higher binding energies, where the contribution of CO in top sites is expected, no significant evidences are visible in the experimental spectrum. This is consistent with the calculations, confirming that the top sites occupation is inhibited by the graphene capping.

C 1s	Exp (eV)	DFT (eV)
		Graphene/CO/Ni(111)
Graphene decoupled by CO	283.8	283.85 [0.50 ML] 284.05 [0.57 ML]
Graphene not interacting	284.4	284.40
Graphene/Ni	284.8	284.8
CO bridge	285.3	not stable
CO hollow		284.95 [0.50/0.57 ML]
CO top	285.9	not stable

Figure 5.4: Experimental and DFT calculated C 1s XPS peaks. The calculated values have been aligned with the experimental peaks for the not-interacting (free standing) graphene. In the DFT column, for each coverage we report the value mediated over different inequivalent C atoms.

We finally investigated by STM the sample surface morphology after CO intercalation, in order to characterize it at the nanoscale.

In Figure 5.5a and b, two topographical STM images (17×17 nm² and 15×15 nm², respec-

tively) show a mainly flat surface sprinkled by bright spots. The atomic resolution achieved allowed obtaining specific information about the morphology of the intercalated graphene layer.

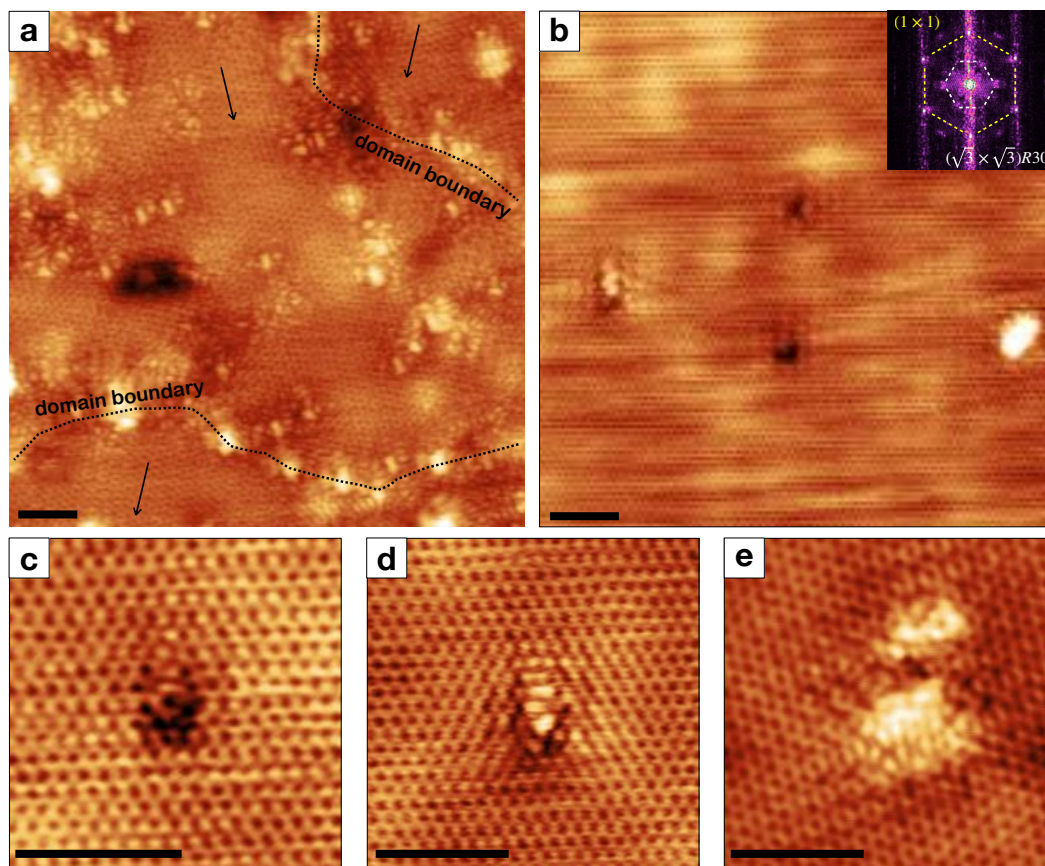


Figure 5.5: STM topographical images of: (a) region with several graphene domains. The grain boundaries separate the different patches and the scattering around these structure is clearly appreciable. Image parameters: $I = 0.22$ nA, $V_{\text{bias}} = -0.35$ V; (b) different types of defects and bubbles imaged on the surface, surrounded by the typical quantum interference pattern due to the scattering effect. In the inset, the FFT of the STM image is shown, exhibiting the (1×1) and $(\sqrt{3} \times \sqrt{3})R30^\circ$ spots. (c), (d), (e) magnifications of defects imaged in (b). In (e) a bubble is shown. Image parameters (b), (c), (d), (e) $I = 1.0$ nA, $V_{\text{bias}} = -0.08$ V. Scale bar: 2 nm.

In Figure 5.5a, several interesting features are visible. First of all, it is important to note that after CO exposure the honeycomb lattice of the graphene mesh is fully visible and all six atoms of the hexagonal structure defined, as expected because of a weaker interaction between the graphene layer and the Ni substrate due to the intercalated CO molecules. Moreover, the superperiodicity observed in the LEED patterns, presented in Figure 5.3, after CO intercalation was not imaged by STM as well as the moiré patterns formed by rotated graphene domains, confirming that graphene is completely detached from the Ni substrate, weakly interacting with the CO molecules at the interface and behaving as a quasi-free-standing graphene. For this reason, we never imaged moiré patterns, even if different graphene orientations are present (see arrow directions in Figure 5.5a). As indicated by the dotted black lines, two domain boundaries are clearly visible in this area, separating graphene patches with different orientation. Along the boundaries, several bright spots are visible, surrounded by the typical defect-induced quantum interference pattern

due to the scattering effect, leading to a $(\sqrt{3} \times \sqrt{3})R30^\circ$ superstructure with respect to the graphene (1×1) lattice [154], as visible in the 2D fast Fourier transform (FFT) shown in the inset in Figure 5.5b. This pattern was appreciable also around the other bright and dark spots randomly distributed on the surface, suggesting that they are defects in the graphene network, likely constituted by Ni adatoms or defects formed during the CO intercalation. In addition, bright protrusion of the graphene mesh were also imaged (upper right corner in Figure 5.5a). These blobs, with different sizes, visible all over the surface only after CO exposure, appear as bubble-like extended defects which might be due to CO clusters or contaminations at the interface. Indeed, the graphene mesh on top is fully visible in Figures 5.5e, compatible with an arrangement "under-cover".

Other kinds of defects have been finally imaged, as shown in Figure 5.5b. All these defects appeared with different shape and size, as dark features or bright protrusion. A zoom on two of these defects is reported in Figure 5.5c and d. Although the atomic resolution achieved allows imaging all C atoms of the graphene network far from the defects, it is not straightforward to identify the precise structure of the defects themselves, due to the remarkable scattering effect. In particular, for the defect in Figure 5.5c, the dark appearance may suggest the presence of one or more C vacancies, while for the defect in Figure 5.5d, the bright protrusion in the center might suggest the presence of a Ni trapped adatom. On this basis, we can tentatively assign them to single or multiple vacancies and Ni adatoms, respectively. Since we did not observe so many multiple C vacancies on the graphene surface before CO exposure, these kind of defects may likely be induced by the high CO pressure at which the sample was exposed.

Once the pristine graphene layer on Ni(111) after CO intercalation at the threshold pressure was fully characterized, we performed some preliminary LEED and STM studies on the effect of the exposure of pristine graphene to higher CO pressures. As mentioned above, only spectroscopic results were reported in literature after CO exposure. CO was demonstrated to intercalate at the interface already at 0.1 mbar and a complete intercalation was observed after exposure to few mbar of CO. However, how the surface appears after the exposure to such high pressure and if CO adsorbs on the Ni surface forming the same structures also in presence of the graphene capping are still questions to be addressed.

In order to investigate these aspects, we exposed pristine graphene on Ni(111) to high CO pressures, in particular to 1.3 mbar and 13.3 mbar of CO for 1 h at room temperature, performing LEED and STM characterizations after exposure. In Figure 5.6a and b, the LEED patterns obtained are shown.

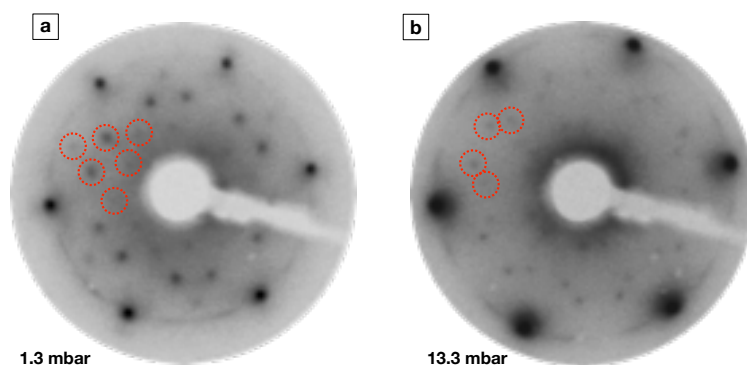


Figure 5.6: LEED patterns of pristine graphene on Ni(111) after exposure to (a) 1.3 mbar and (b) 13.3 mbar for 1 h. (a) $E= 98$ eV, (b) $E= 78$ eV. Red dotted circles indicate the extra spots.

As after exposure at the threshold CO pressure, the standard graphene/Ni(111) pattern and additional spots due to CO on Ni(111) are visible. However, after high pressure exposures, the extra spots appear sharp and clear, forming two well distinct patterns at 1.3 mbar and 13.3 mbar of CO, which clearly correspond to those reported in literature for different ordered CO superstructures on the clean Ni surface [117, 118]. In particular, the diffraction pattern in Figure 5.6a is associated to $c(4\times 2)$ (coverage of 0.50 ML) whereas the pattern in Figure 5.6b corresponds to $(\sqrt{7}\times\sqrt{7})R19^\circ$ (coverage of 0.57 ML). We can therefore conclude that CO, once intercalated, adsorbs at the interface between graphene and Ni(111), arranging in the same structures formed on bare Ni(111).

Comparing these LEED patterns to the one obtained after exposure to 0.7 mbar of CO and reported in Figure 5.3, it is important to note that at higher pressures the enhanced intensity and sharpness of the diffraction structure formed by CO on Ni(111) confirm an increase of the CO long-range order at the interface.

From a morphological point of view, no significant differences with respect to the previously presented STM data obtained at lower pressure were observed.

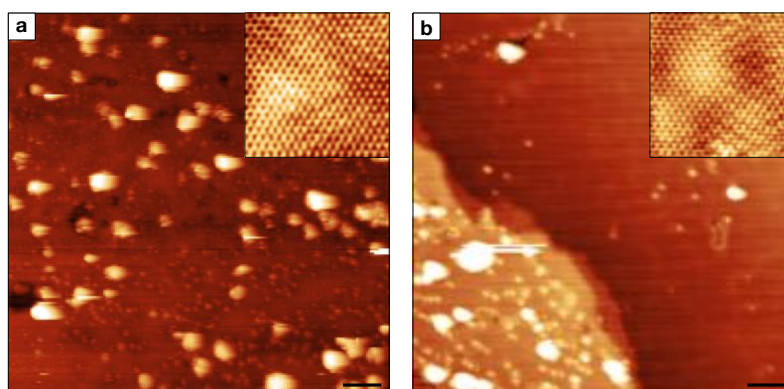


Figure 5.7: STM topographical images of the pristine graphene surface after the CO exposure at (a) 1.3 mbar and (b) 13.3 mbar for 1h at room temperature. Insets show 5×5 nm² magnifications of the surface. Images parameters: (a) $I=0.05$ nA, $V=-0.6$ V. Inset: $I=0.7$ nA, $V=-0.2$ V; (b) $I=0.3$ nA, $V=1$ V. Inset: $I=0.2$ nA, $V=0.2$ V. Scale bar= 5 nm.

The surface appears flat with bright spots of different size on top. As already discussed, we ascribe the small bright spots to defects in the graphene network, such as Ni adatoms trapped in the network and C vacancies, whereas the bigger bright spots might be attributed to contaminations deposited on or below the surface during CO exposure, due to the high pressure fluxed.

5.2 CO on N-doped Graphene on Ni(111)

So far, the reactivity of a pristine graphene layer on Ni(111) at different CO pressures was described and discussed. In this section, we present the experimental data obtained for the reactivity experiments carried out on the N-doped graphene layers grown on Ni(111) substrate, following our alternative protocol described in chapter 4, section 4.1, focusing on the comparison with the reactivity of pristine graphene. Also in this case, we investigated the pressure threshold above which the CO molecules start to intercalate at the interface between the N-doped graphene layer and the Ni substrate and the modifications of the electronic structure and the surface morphology, induced by CO intercalation.

5.2.1 CO intercalation at the N-doped Graphene/Ni(111) interface

In order to determine the pressure threshold for CO intercalation underneath N-doped graphene on Ni(111), we proceeded by exposing the sample to a gradually increasing CO pressure and characterizing it by XPS, as done for pristine graphene. To compare the N-doped graphene data with the pristine graphene case, we exposed the doped system to similar pressure conditions, while keeping the sample at room temperature.

In Figure 5.8, the XPS spectra relative to the C 1s core level region are shown, comparing the experimental results for N-doped graphene before (Figure 5.8a) and after (Figure 5.8b) exposure to 0.03 mbar of CO for 1 h at room temperature, which resulted to be the threshold pressure for intercalation under N-doped graphene.

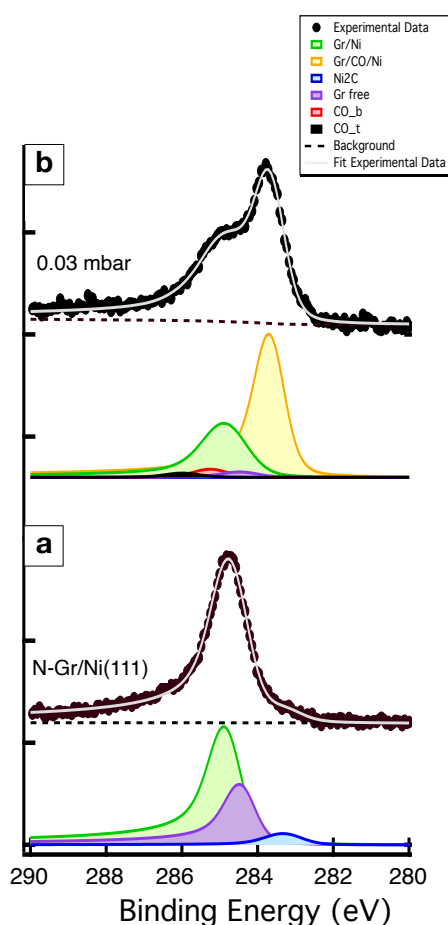


Figure 5.8: C 1s core level spectra of N-doped graphene on Ni(111) (a) before the exposure and (b) after the exposure to 0.03 mbar of CO for 1 h at room temperature.

As it is visible in panel a of Figure 5.8, the C 1s peak relative to N-doped graphene on Ni(111) before exposure can be fitted using three components, as already described in detail for the case of pristine graphene (see section 5.1):

- graphene C atoms ascribed to the graphene domains strongly interacting with the Ni substrate: "Gr/Ni" (green);
- graphene C atoms belonging to the component that we labelled "Gr free", less interacting with the substrate with respect to "Gr/Ni" and ascribed to rotated graphene

with Ni_2C underneath (purple);

- C atoms coordinated with the Ni surface atoms forming nickel carbide underneath graphene: " Ni_2C " (blue).

Small variations in the components intensity are related to different composition of the sample due to the preparation. Indeed, even if the same growth protocol is used, different ratio between epitaxial and rotated graphene phases are observed and a different amount of Ni carbide is formed at the graphene/Ni interface, depending on the specific sub-surface carbon concentration.

After exposure of N-doped graphene to 0.03 mbar of CO, the relative C $1s$ spectrum, reported in Figure 5.8b, appears clearly different. As for pristine graphene after exposure to 0.7 mbar of CO, a new component centered at 283.6 eV is clearly visible. According to the literature, this was the one we ascribed to graphene C atoms weakly interacting with the Ni substrate, due to the presence of CO at the interface. We also notice that the component associated to C atoms of CO molecules on Ni(111) at 285.3 eV is very small, probably because the sample is not completely intercalated (as suggested by the presence of a significant peak of graphene on Ni at 284.6 eV) and the C signal of CO is attenuated by the graphene layer. Nevertheless, the clear peak at 283.6 eV, ascribed to graphene weakly interacting with Ni, is a strong evidence that the intercalation took place. Furthermore, the O $1s$ core level spectrum reported in Figure 5.9 unambiguously confirms the presence of CO on Ni(111), showing a peak centered at a binding energy of 531.0 eV, in agreement with literature [106].

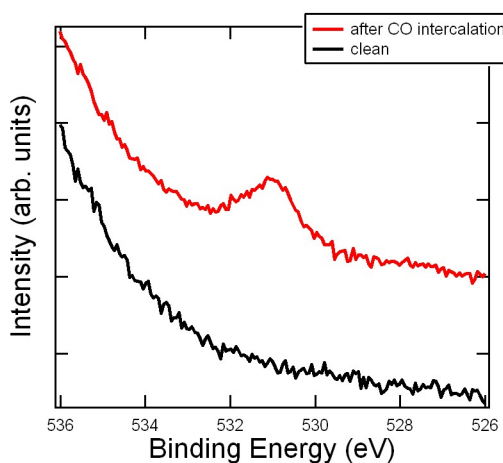


Figure 5.9: O $1s$ core level spectrum of N-doped graphene on Ni(111) before (black profile) and after (red profile) CO intercalation.

Comparing the pressure required for CO intercalation in the pristine and N-doped graphene systems, it is worth noting the significantly lower threshold pressure at which the process occurs in presence of nitrogen dopants, one order of magnitude lower with respect to pristine graphene.

In order to thoroughly investigate the process and to confirm CO intercalation, we characterized the sample surface by means of LEED and STM, obtaining long-range order structural information and a morphological analysis at the nanoscale, respectively.

In Figure 5.10, the LEED pattern of the N-doped graphene sample exposed to 0.03 mbar of CO is reported. As for pristine graphene after exposure to 0.7 mbar of CO, besides the standard spots expected for Ni(111), epitaxial graphene and rotated graphene domains,

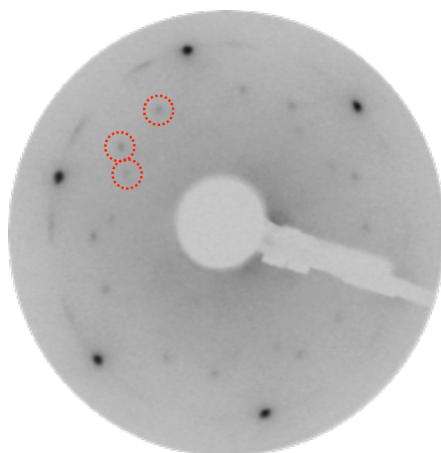


Figure 5.10: LEED patterns of N-doped graphene on Ni(111) after exposure to 0.03 mbar for 1 h at room temperature. Red dotted circles indicate the extra spots. ($E = 97.5$ eV)

new extra spots clearly appeared in the diffraction pattern.

At variance with what observed in Figure 5.3 for pristine graphene exposed to 0.7 mbar of CO, in this case the extra spots forming the superstructure appear sharp, indicating a well-ordered distribution of CO at the interface between the graphene layer and the Ni substrate. Indeed, in the case of pristine graphene, we ascribed the smearing of the diffraction spots to a not completely ordered structure, also compatible with the coexistence of two adsorption configurations. The resulting diffraction pattern for N-doped graphene is compatible with the one obtained in the pristine graphene case after exposure to 13.3 mbar of CO pressure, three orders of magnitude higher than for CO on N-doped graphene, thus pointing out an enhancement in the sensitivity for the doped system. The LEED structure corresponds to the $(\sqrt{7} \times \sqrt{7})R19^\circ$ CO superstructure on clean Ni, ascribed in literature to a CO coverage of 0.57 ML [118]. This pattern appears homogeneous on the whole sample surface, apparently in disagreement with the XPS spectrum where we observe only a partial CO intercalation, as shown in Figure 5.8b. Thus, we conclude that there are small regions not intercalated, randomly distributed on the sample surface. Therefore, we can guess that, where the intercalation occurred, the CO molecules arrange on the Ni surface in a well-ordered superstructure, maximizing their coverage in those areas, as proved by the LEED pattern in Figure 5.10.

In order to validate our interpretation, numerical simulations were performed by our collaborators at the University of Milano-Bicocca. Their computational study demonstrated that, after the first CO molecule reaches the interface, there is a significant energy cost for each additional CO to access the interface. They found a critical point, corresponding to a CO coverage of 0.14 ML, for which the energy cost to detach the graphene layer from the Ni substrate is counterbalanced and even overcome by the energy gain of establishing a certain amount of Ni-CO bonds and higher coverages, like 0.50 ML and 0.57 ML, are even more favorite [155]. This corroborates the possibility to have high CO coverage "clustered" in localized areas and not equally distributed at the whole interface.

We finally investigated the sample morphology by STM at room temperature, in order to characterize the surface at the nanoscale.

In Figure 5.11a and b, two large-scale STM topographical images show the N-doped graphene surface after CO exposure.

In Figure 5.11a, a 30×30 nm² image allows appreciating the standing waves in the

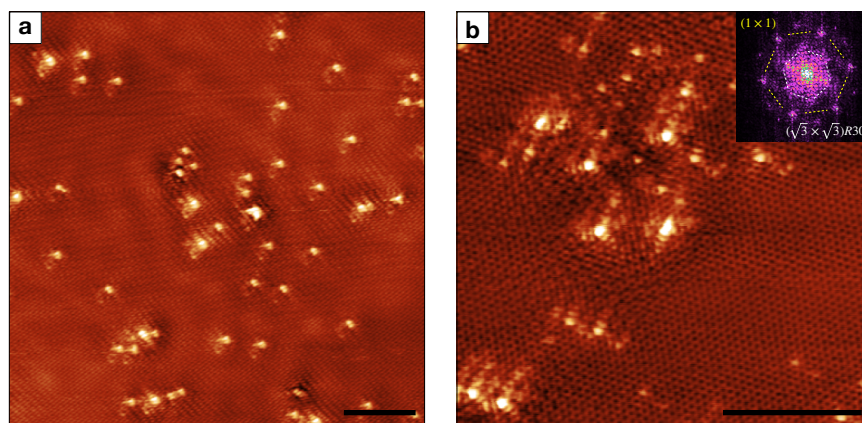


Figure 5.11: STM topographical images of two regions of the N-doped graphene layer after the exposure to CO. The surface scattering effect due to the presence of defects is clearly visible in both the STM images and confirmed in the FFT inset in (b) by the typical $(\sqrt{3} \times \sqrt{3})R30^\circ$ periodicity. Image parameters: (a) $I = 0.45$ nA, $V_{\text{bias}} = -0.09$ V; (b) $I = 0.98$ nA, $V_{\text{bias}} = -0.05$ V. Scale bar: 5 nm.

electronic structure surface originated by the presence of defects and impurities in a configuration of quasi-free-standing graphene. This is a clear evidence of the detachment of the N-doped graphene layer from the Ni substrate, unambiguously confirming CO intercalation, at lower pressure with respect to the pristine case. Another interesting feature visible in Figure 5.11a is the scattering effect around the bright defects and impurities, which is clearly imaged in the zoom shown in Figure 5.11b. More information can be extracted from the latter. First, the graphene mesh is fully visible, as C atoms in the network do not hybridize with the substrate any more, due to the presence of CO molecules at the interface. Second, the bright protrusions indicate the presence of defects or impurities trapped in the graphene mesh. Based on the characterization of the layer before exposure to CO where several defect configurations were identified, we expect these defects to be N dopants and/or Ni adatoms trapped in the network. Third, thanks to the high atomic resolution achieved, the $(\sqrt{3} \times \sqrt{3})R30^\circ$ periodicity around the defects, due to the impurity-induced quantum interference effect [154], is clearly visible in the STM topographical image and unambiguously confirmed by the 2D fast Fourier transform (FFT) shown in the inset in Figure 5.11b. However, at variance with pristine graphene, it is worth noting that in this case not all defects show a quantum interference pattern around and this might be a key factor in order to discriminate between different defect configurations. Indeed, the scattering effect is expected to be induced by the presence in the graphene network of one or more C vacancies or dislocation. Thus, this feature might help to discriminate at least between graphitic and pyridinic N defects.

In order to investigate this aspect, we imaged at high resolution two defects of different kind, shown in Figures 5.12a and b, both displaying a triangular shape but appearing differently in size and brightness, as described above.

In particular, the defect shown in Figure 5.12a appears bigger and brighter than the one imaged in Figure 5.12b. Around it, a bright pattern forming a $(\sqrt{3} \times \sqrt{3})R30^\circ$ periodicity is clearly visible, which we ascribe to the typical quantum interference pattern due to scattering effect likely induced by one or more C vacancies in a graphene weakly interacting with the substrate [154]. These markers point to a N pyridinic configuration, as nicely confirmed by the simulation reported in Figure 5.12c. On the other hand, the defect shown in Figure 5.12b is not surrounded by the same bright scattering pattern, therefore suggesting

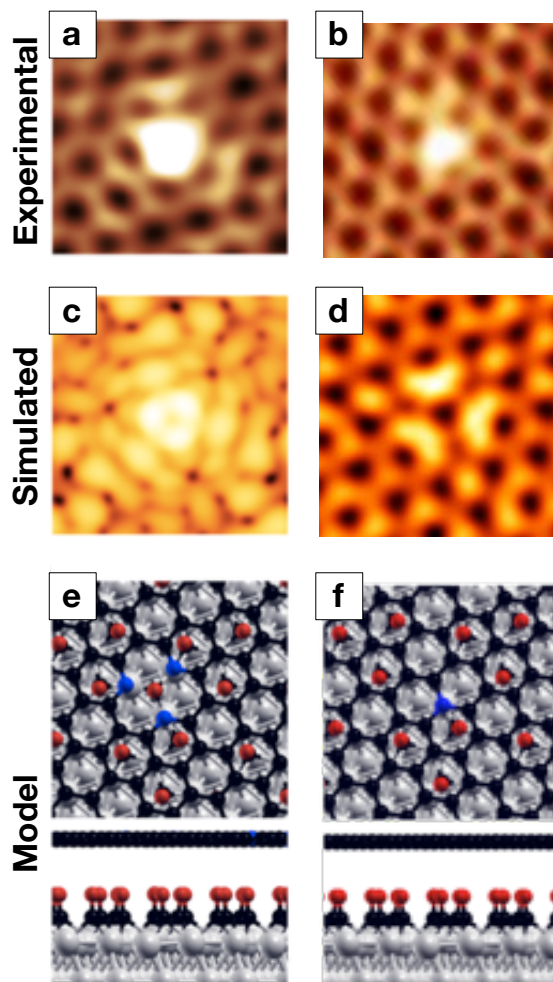


Figure 5.12: Experimental (a,b) and simulated (c,d) STM images of 3N pyridinic and 1N graphitic on the N-doped graphene layer after the exposure to CO. (e) and (f) show the model in top and side view of the N configurations in (a) and (b), respectively. Image parameters: (a), (b) $I = 0.98$ nA, $V_{bias} = -0.05$ V. Computational details: $V_{bias} = -0.05$ V, ILDOS iso-surface lying ≈ 3 Å above graphene and with ILDOS value of 1×10^{-5} $|e|/a_0^3$.

a complete graphene mesh and thus a N graphitic configuration. This hypothesis was confirmed by the simulated image reported in Figure 5.12d, where mustache-like features are theoretically reproduced, similarly to the experimental image. However, it is important to note that the center of the defect appears bright in the experimental images while it appears dark in the simulated ones. This discrepancy might be related to the theoretical approach used. The Tersoff-Hamann method [122], indeed, is a widely used theoretical approach for simulating STM images which, however, use several approximations and thus has some limitations. In particular, the tip is approximated with a spherical shape using only s orbitals and this might result in a significant discrepancy with the observed experimental features [25].

The experimental results discussed so far demonstrate that CO intercalates at the interface between the N-doped graphene layer and the Ni substrate at RT and high pressures. This process occurred at a significantly lower pressure compared to pristine graphene, thus pointing out an enhancement of the sensitivity of the N-doped graphene/Ni(111) sys-

tem towards CO molecules. As reported in the chapter 2, section 2.5.3, at RT, N-doped graphene was demonstrated to be inert to low pressure of CO [88], showing a clear signal of CO adsorption on the surface only upon exposure of the layer at low temperature (87 K). In these experimental conditions, the authors detected two chemisorbed CO species in the HREEL spectrum: the dominant one corresponds most likely to adsorption at non-doped sites; the minority species, on the contrary, is associated to CO admolecules sitting close to N-doped sites of pyridinic and/or pyrrolic nature, thus concluding that N doping enables stabilization of adsorbed CO at graphene/Ni(111).

According to literature, we did not observe interaction between CO and N-doped graphene at low CO pressures at room temperature. Only after exposure to high CO pressures, above a threshold pressure, CO was experimentally demonstrated to intercalate in the confined zone between graphene and Ni. This process drastically modified the electronic properties and the morphology of the doped system, as demonstrated by the C *1s* core level spectra and the STM images presented and discussed above, allowing us to conclude that CO intercalation is possible only at high pressures and can not be achieved at low pressure conditions.

5.3 CO intercalation mechanism

The experimental data discussed above for pristine and N-doped graphene on Ni(111) demonstrate that similar effects are induced by exposing the two systems to near-ambient pressure of CO, in the mbar regime. Indeed, CO was demonstrated to intercalate at the interface on pristine and N-doped graphene, showing analogous chemical and morphological fingerprints but at drastically different CO pressure threshold (one order of magnitude difference in the threshold pressure for the process): the N-doped graphene layer was demonstrated to react at a lower CO pressure with respect to the pristine layer, thus suggesting a possible role of the nitrogen dopants in the interaction with CO molecules.

In order to explain the large difference in the threshold pressure for the process, the CO intercalation mechanism and the role of N dopants must be unveiled. In collaboration with the theoretical group at the University of Milano-Bicocca, we performed a thorough DFT investigation aimed at proposing a possible pathway promoting CO intercalation at the interface [155]. Indeed, it is well known that defect-free graphene is impermeable to any atomic or molecular species in gas or liquid phase [156]. Even the smallest element of the periodic table, hydrogen, can not penetrate the graphene mesh. Recently, it has been reported that it seems possible to activate the permeation of atomic and molecular hydrogen by a peculiar flipping mechanism in the presence of a local curvatures of the graphene layer [157]. On the other hand, for large-sheet stacked graphene-membranes, it has been reported that gas permeation may take place through structural defects and the kinetics of the process largely depends on their size and concentration [158]. Therefore, it is reasonable to assume that structural defects may play a key role in the intercalation of gas molecules at the interface between graphene and its supporting substrate [159]. Moreover, the graphene permeability may be influenced by the presence of dopants [160].

In this chapter we will investigate the physical mechanism behind the CO intercalation at the interface between the pristine and N-doped graphene layers and the Ni substrate.

5.3.1 Pristine Graphene/Ni(111)

As previously discussed, atoms and molecules cannot penetrate defect-free pristine graphene [156] thus, in order to access the confined zone at the interface between graphene and the

supporting substrate, structural defects like carbon vacancies or large dislocations should be present in the network.

In pristine graphene on Ni(111), the most common atomic defect is reported to be a tri-atomic C vacancy trapping a Ni adatom ($1\text{Ni}@3\text{VG}$) [149]. In this kind of defect, as experimentally imaged and theoretically demonstrated, Ni partially fills the large vacancy, leaving a hole in the network which is supposed to be the door for CO intercalation. However, based on our theoretical calculations, the $1\text{Ni}@3\text{VG}$ defect is not involved in the process. Indeed, modeling a CO molecule on top of this defect, the C atom of the molecule is found to fill the C vacancy of the graphene mesh and the oxygen atom strongly binds to Ni, as shown in Figure 5.13. By adding a second CO molecule to the system, the formation of CO_2 is observed, with a C atom healing the graphene mesh. Therefore, the final state of the system results in a vacancy-free graphene layer promoting the catalysis of CO in CO_2 . Since the tri-atomic vacancy was theoretically found to be not suitable for CO intercalation, due to steric hindrance, a tetra-atomic vacancy was considered. In this case, the

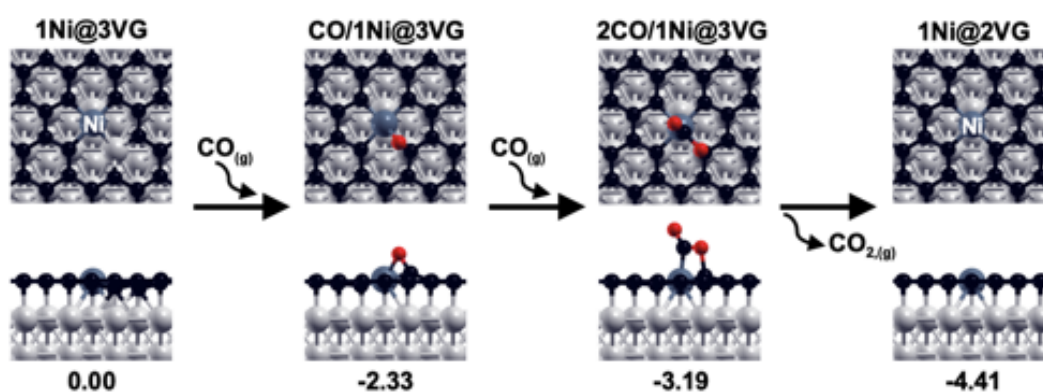


Figure 5.13: Top and side views of the intermediates along the CO reaction path on the most common defect in pristine graphene on Ni(111): a tri-atomic C vacancy with a trapped Ni adatom ($1\text{Ni}@3\text{VG}$). The reaction energies (in eV) are reported below each structure. Color coding: Ni atoms in grey, Ni adatom (labelled) in dark grey, C atoms in black, O atoms in red.

uncoordinated C atoms surrounding the vacancy appear to be very reactive, opening two scenarios: (i) they bind to the underlying Ni substrate, closing in this way the door and blocking the passage of the molecules into the confined zone between graphene and the Ni surface, or (ii) they might react with the residual hydrogen gas present in the chamber forming CH bonds or directly with the dosed CO molecules. In this second case, the physical space is drastically reduced by the bounded H atoms or CO molecules, making hard for CO molecules to pass through the gate because of steric hindrance. This results in a high energy barrier to be overcome, lowering the probability for the process to occur.

However, experimentally, such tetra-atomic vacancies were not imaged on the pristine graphene surface on the terraces. Significant distortion of the graphene network was imaged only along the domain boundaries where it is often possible to see a regular pentagons-octagon arrangement [107].

Therefore, we can conclude that CO molecules arrive at the interface passing through the dislocations at the domain boundaries or by the physical borders of the sample.

5.3.2 N-doped Graphene/Ni(111)

We demonstrated that N-doped graphene on Ni(111) is more sensitive to CO molecules than pristine graphene, and intercalation occurs at a significantly lower pressure. Therefore, N dopants are supposed to be the key factor for such enhanced CO reactivity [155]. In the case of N-doped graphene on Ni(111), the most common atomic defect is a C vacancy decorated by three pyridinic N atoms (3N pyridinic top defect discussed in chapter 4, section 4.2.1). Based on theoretical calculations, the adsorption of one CO molecule in this C vacancy is very unstable because the defect is too small to accommodate it [155].

As for the pristine case, a larger tetra-atomic C vacancy has been proposed. Observing that N atoms tend to diffuse and segregate at the defect edge, this would result in a 6 N pyridinic defect (4VG-6N). At variance with what discussed for the tetra-atomic defect in pristine graphene, where C atoms at the edge were demonstrated to be strongly reactive, N atoms in pyridinic configuration are much less bound to the underlying Ni substrate than unsaturated C atoms, resulting in a passivation of the defect towards a possible reactivity with residual H₂ or dosed CO (as supposed for the pristine case) and keeping in this way the door open for intercalation. Indeed, no steric hindrance has been observed in this case, allowing the possible entrance of the molecules through this defect.

Experimentally, the 4VG-6N defect was imaged on the N-doped graphene surface and along the domain boundaries, as shown in chapter 4 section 4.2.2 (see Figure 4.15). This experimental evidence validates this defect as possible gate for CO molecules towards the interface.

In order to investigate the CO intercalation mechanism, the approach used to simulate the kinetic process by *ab initio* calculations was to investigate the energy profile for one CO molecule to vertically enter the atomic hole, by moving the CO molecule along the z-direction and, at each different CO height, allowing all the atoms to fully relax. Numerical simulations show that a first CO molecule is favorably bound to the Ni surface (-0.6 eV), as reported in Figure 5.14a. As a further step, other CO molecules were added to the system, one at a time, and the variation in energy normalized to the number of added CO molecules was analyzed, demonstrating that the energy cost is relatively small not only for one CO molecule at a time to go through the hole, but also to intercalate at the interface between graphene and Ni [155]. This is because the N atoms are not strongly interacting with the substrate and therefore graphene can be lifted at a reasonable cost to facilitate the CO passage.

In order to investigate the whole process, an energy decomposition analysis has been performed considering the cost to decouple graphene from the substrate, the cost to distort the graphene layer and accommodate the CO molecules and the binding energy for the Ni-CO bonds. The first two terms represent an energy costs, whereas the third one is an energy gain. Then, a further investigation of the role played by the CO molecules distribution on the Ni surface was performed. Indeed, from an experimental point of view, a well ordered diffraction pattern was observed even after a partial CO intercalation, allowing to assume that in the initial phase most of the CO molecules are regularly distributed close to the multiatomic hole through which they reached the interface and then they gradually diffuse under the graphene layer, becoming more equally distributed on the Ni surface. Numerical simulations verified this scenario in two steps. In the first step, the stabilization energy at a CO coverage of 0.14 ML was compared for two different CO distribution for 4VG-6N: (a) close to the hole edges and (b) more equally distributed at the interface. Passing from (a) to (b), there is an energy gain per CO molecule of -0.044 eV, which indicates a driving force for the CO molecules to better distribute at the interface between the N-doped graphene layer and the supporting Ni substrate. In the second step, the ac-

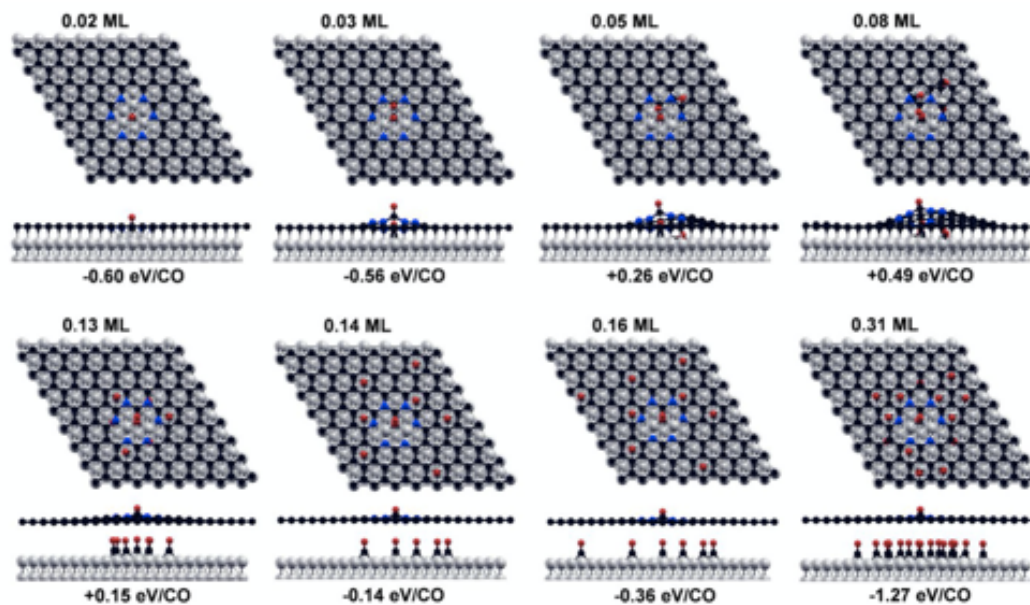


Figure 5.14: Top and side views of the intermediates of the CO intercalation process on 4VG-6N. The adsorption energies (in unit of eV), normalized to the number of CO molecules, are reported below each structure. Color coding: Ni atoms in grey, C atoms in black, O atoms in red, N atoms in blue.

tivation barrier for CO diffusion in the confined zone between Ni(111) and graphene was estimated through a nudged elastic band (NEB) calculation and it resulted to be very close to that computed for the corresponding process on the bare Ni(111) surface [161, 162], thus indicating that a regular distribution of CO on the Ni surface is favored even in presence of the graphene capping.

Chapter 6

Conclusions

In this thesis, the growth, structure and reactivity of N-doped graphene layers on Ni(111) have been investigated by means of STM, XPS and LEED in UHV conditions, and compared to the pristine graphene case. The experimental results are complemented by numerical simulations and allow unveiling, to the best of our knowledge for the first time, the structure and morphology of a N-doped graphene layer on Ni(111), as well as its enhanced sensitivity towards CO. In this regard, we presented a mechanism for CO molecules intercalation at the interface between graphene and Ni, demonstrating that the presence of N dopants in the graphene layer highly facilitates the permeation process.

In chapter 4, we presented a new growth method, alternative to those already reported in literature, to obtain high-quality nitrogen-doped graphene on Ni. We illustrated our protocol, which allows introducing nitrogen dopants in the graphene network *via* standard LP-CVD growth by exposing a Ni crystal, previously doped with nitrogen, to a common carbon-containing precursor, ethylene. This clean and highly reproducible growth method, based on a simple and controlled preparation procedure, ensures the formation of layers of high morphological quality. The resulting N-doped graphene layers were thoroughly characterized by STM and XPS, in synergy with an in-depth Density Functional Theory (DFT) investigation, including simulated STM images for a wide set of models for the N centers. XPS measurements unambiguously confirmed the presence of N dopants trapped in the graphene network in the form of graphitic and pyridinic N defects. Their configurations at the nanoscale were imaged by STM and their atomic structure unveiled. N dopants were found to be located in different graphene sublattices and thus in different sites with respect to the Ni substrate, resulting in different defect configurations: graphitic N in top and fcc sites, as well as three pyridinic N atoms decorating the edges of a C vacancy, in top and fcc position. Other structures involving different numbers of N atoms, imaged and described in chapter 4, were also found although more rarely, pointing out a lower stability of such structures which is reflected also in the ratio between pyridinic and graphitic defects imaged on the surface. On the basis of our experimental evidences and of the numerical simulations performed, we concluded that the higher abundance of 3N pyridinic defects with respect to graphitic ones is a clear indication of the preference for the N atoms to be located at the edges of a C vacancy rather than replacing a C atom within the graphene matrix, thus explaining the pyridinic/graphitic ratio. Moreover, the higher stability of N atoms in a pyridinic configuration leads to the formation of a fully N-decorated C vacancy, thus excluding the possibility to have 1N pyridinic defects. We finally tentatively related such pyridinic/graphitic balance to the doping technique: adding N atoms during growth conditions favors the dynamic selection of defects with lower energy, with no constraint posed by the local abundance of N atoms required. Conversely,

other doping techniques such as post-growth ion implantation may favor a distribution of defects with a different pyridinic/graphitic ratio, as a consequence of the ballistic formation process.

In chapter 5, the reactivity towards CO molecules of N-doped graphene on Ni(111) was investigated and compared to pristine graphene. By means of spectroscopic and microscopic measurements, we confirmed that, by exposing pristine graphene to CO pressures in the mbar regime at room temperature, CO molecules intercalate at the interface between pristine graphene and the supporting Ni substrate. The presented LEED patterns show, in presence of the graphene capping, the same typical structures formed by CO on bare Ni(111) at different coverages. Combining the XPS and LEED experimental proof with the theoretical results, we shed light on the CO adsorption sites on the Ni surface, confirming that intercalated CO molecules occupy mainly positions between hollow and bridge sites, while the graphene cover inhibits the occupation of top sites.

As for the pristine case, by exposing N-doped graphene on Ni to high pressures of CO, we demonstrated that the intercalation process took place. However, for the doped system, CO intercalation was demonstrated to occur at a threshold pressure one order of magnitude lower with respect to pristine graphene. Moreover, the diffraction pattern visible in this case was the same observed for pristine graphene after exposure to three orders of magnitude higher CO pressure, thus pointing to a significant enhancement of the sensitivity towards CO molecules of the N-doped graphene/Ni(111) system.

We finally tried to combine the results we obtained for the morphology and the reactivity towards CO for pristine and N-doped graphene layers, in order to rationalize the huge difference in the threshold pressures for the two systems, explaining the role played by N atoms in the enhancement of the sensitivity. Since, in general, defects and dislocations are supposed to be the door towards the interface, from the N-doped graphene characterization, we expected that the huge amount of 3N pyridinic defects were responsible for the enhanced intercalation. However, we demonstrated they are too small to accommodate CO molecules at the interface, thus suggesting the presence of larger defects. Therefore, we proposed a CO intercalation mechanism where the doors to the bidimensional nanospace at the interface are multiatomic vacancy defects, as the 4VG-6N configurations imaged on the N-doped graphene surface and along the grain and domain boundaries. The N atoms decorating the edges of the large defects facilitate the permeation process, lowering the intercalation barrier due to a reduced interaction between the graphene layer and the underlying substrate, thus keeping open the doors to the confined zone at the graphene/Ni interface.

Summarizing, the work presented in this thesis addresses the open questions reported in the introduction, developing a new growth method which allows producing N-doped graphene on Ni of high morphological quality in a easy, reproducible and scalable way, thus avoiding the often troublesome production methods reported so far in literature. The resulting layers were fully characterized from a chemical and morphological point of view and the N dopant structures at the nanoscale revealed. Finally, it was demonstrated a significant enhancement towards CO reactivity in presence of N dopants trapped in the network with respect to pristine graphene, as it was predicted in literature. Thanks to a joint approach between theory and experiment, we propose a CO intercalation mechanism, capable to explain why the process can occur for pristine and doped graphene, even if it is impermeable to any atomic and molecular species in gas and liquid phase as well as a reasonable explanation of the role played by N dopants in the intercalation and of the large difference in the threshold pressure between the doped and pristine systems. Similar mechanisms are likely to apply to other cases of molecular intercalation at the

graphene/metal interface, where the process has been observed but not yet explained.

These results can have crucial implications in several fields, for example, in gas sensors and storage. Indeed, CO intercalation at the interface between graphene and Ni produces a double effect. First, CO molecules are successfully trapped below graphene, obtaining stable CO configurations on Ni at room temperature. This results in an efficient storage of CO molecules, durable in time, making this promising as a storage system. Second, since the electronic properties of graphene have been significantly modified by the interaction with CO molecules, as demonstrated by XPS measurements, we may expect it to be suitable as prototype of a graphene-based gas sensor. The enhancement of the sensitivity towards CO demonstrated for the N-doped system, makes N-doped graphene one of the most promising candidates for this kinds of technological applications.

Besides these two implications, CO trapped in the confined bidimensional nanospace might participate in processes of catalysis under-cover, due to the high catalytic activity of the Ni substrate, thus pointing to a possible key performance of pristine and N-doped graphene on Ni for nanoreactors. Combining this to the predicted properties of N-doped graphene as efficient metal-free electrocatalyst for oxygen reduction, the system may result in interesting and unexpected applications, for example as nanoreactor for the oxygen reduction reaction in fuel cells.

The next challenge is now to assess to what extent the mechanism we have proposed is a general one, which will require a systematic investigation considering other gases and different dopants. A clear solution to this puzzle is a crucial step toward the graphene/metal interface engineering in order to design and realize systems with tailored properties for practical applications.

Appendix A

DFT calculation details

Density Functional Theory (DFT) calculations were performed by the group of Prof. Maria Peressi (University of Trieste) [163] and the group of Prof. Cristiana di Valentin (University of Milano-Bicocca) [155, 131], using the plane-wave-based Quantum ESPRESSO package (QE) [164, 165]. All the details can be found in the PhD thesis of Dr. Daniele Perilli of the University of Milano-Bicocca. The ultrasoft pseudopotentials [166] were adopted to describe the electron-ion interaction with Ni (3d, 4s), C (2s, 2p), O (2s, 2p), N (2s, 2p), and H (1s), treated as valence electrons. Energy cutoffs of 30 Ry and 240 Ry (for kinetic energy and charge density expansion, respectively) were adopted for all calculations. The Perdew-Burke-Ernzerhof functional (PBE) was used for electron exchange-correlation [167]. To properly describe the graphene/Ni interaction, semiempirical corrections accounting for the van der Waals interactions were included with the DFT-D2 formalism [168]. Spin polarization was always included. The Ni(111) surface was modeled by a three-layer slab with a bottom layer fixed to the bulk positions during the geometry relaxation to mimic a semi-infinite solid. To avoid interactions between adjacent periodic images, a vacuum space of about 15 Å in the direction perpendicular to the surface was used. Epitaxial graphene, i.e., aligned with respect to the substrate, was always considered and in particular in the top-fcc registry as initial configuration, motivated by the higher abundance of such domains as experimentally detected [107]. In the top-fcc registry, $(2\sqrt{7} \times 2\sqrt{7})$ and (8×8) supercells were used for pristine and defective graphene, respectively. The geometry relaxation of all considered systems was performed only at Γ point, followed by a single self-consistent field (SCF) cycle calculation with a $2 \times 2 \times 1$ Monkhorst-Pack k-points mesh [169] to get more accurate total energies. The Climbing Image-Nudged Elastic Band (CI-NEB) method [170] was employed to simulate the CO diffusion process at the graphene/Ni interface, generating the minimum energy path of the reaction step and an evaluation of the energy barrier. STM simulations were performed using the Tersoff-Hamann approach [122], according to which the tunneling current is proportional to the energy-integrated Local Density of States (ILDOS). Ball-and-stick models and STM images were rendered with XCrySDen [171] and Gwyddion [172] software, respectively.

Bibliography

- [1] K. S. Novoselov, A. K. Geim, S. V. Morozov, D. Jiang, Y. Zhang, S. V. Dubonos, I. V. Grigorieva, and A. A. Firsov. Electric field effect in atomically thin carbon films. *science*, 306(5696):666–669, 2004.
- [2] F. Bonaccorso, Z. Sun, T. A. Hasan, and A. C. Ferrari. Graphene photonics and optoelectronics. *Nature photonics*, 4(9):611, 2010.
- [3] L. Vicarelli, M. S. Vitiello, D. Coquillat, A. Lombardo, A. C. Ferrari, W. Knap, M. Polini, V. Pellegrini, and A. Tredicucci. Graphene field-effect transistors as room-temperature terahertz detectors. *Nature materials*, 11(10):865–871, 2012.
- [4] T. Mueller, F. Xia, and P. Avouris. Graphene photodetectors for high-speed optical communications. *Nature photonics*, 4(5):297, 2010.
- [5] K. Kostarelos and K. S. Novoselov. Exploring the interface of graphene and biology. *Science*, 344(6181):261–263, 2014.
- [6] L. Schlapbach and A. Züttel. Hydrogen-storage materials for mobile applications. In *Materials for sustainable energy: a collection of peer-reviewed research and review articles from nature publishing group*, pages 265–270. World Scientific, 2011.
- [7] F. Schedin, A. K. Geim, S. V. Morozov, E. W. Hill, P. Blake, M. I. Katsnelson, and K. S. Novoselov. Detection of individual gas molecules adsorbed on graphene. *Nature materials*, 6(9):652–655, 2007.
- [8] M. Farjam and H. Rafii-Tabar. Energy gap opening in submonolayer lithium on graphene: Local density functional and tight-binding calculations. *Physical Review B*, 79(4):045417, 2009.
- [9] T. Mashoff, M. Takamura, S. Tanabe, H. Hibino, F. Beltram, and S. Heun. Hydrogen storage with titanium-functionalized graphene. *Applied Physics Letters*, 103(1):013903, 2013.
- [10] L. S. Panchakarla, K. S. Subrahmanyam, S. K. Saha, A. Govindaraj, H. R. Krishnamurthy, U. V. Waghmare, and C. N. R. Rao. Synthesis, structure, and properties of boron-and nitrogen-doped graphene. *Advanced Materials*, 21(46):4726–4730, 2009.
- [11] Y. Jiao, Y. Zheng, M. Jaroniec, and S. Z. Qiao. Origin of the electrocatalytic oxygen reduction activity of graphene-based catalysts: a roadmap to achieve the best performance. *Journal of the American Chemical Society*, 136(11):4394–4403, 2014.
- [12] C. H. Choi, S. H. Park, and S. I. Woo. Binary and ternary doping of nitrogen, boron, and phosphorus into carbon for enhancing electrochemical oxygen reduction activity. *ACS nano*, 6(8):7084–7091, 2012.

- [13] Z. S. Wu, W. Ren, L. Xu, F. Li, and H. M. Cheng. Doped graphene sheets as anode materials with superhigh rate and large capacity for lithium ion batteries. *ACS nano*, 5(7):5463–5471, 2011.
- [14] S. Nachimuthu, P. J. Lai, and J. C. Jiang. Efficient hydrogen storage in boron doped graphene decorated by transition metals—A first-principles study. *Carbon*, 73:132–140, 2014.
- [15] B. P. Vinayan, R. Nagar, and S. Ramaprabhu. Solar light assisted green synthesis of palladium nanoparticle decorated nitrogen doped graphene for hydrogen storage application. *Journal of Materials Chemistry A*, 1(37):11192–11199, 2013.
- [16] M. Inagaki, M. Toyoda, Y. Soneda, and T. Morishita. Nitrogen-doped carbon materials. *Carbon*, 132:104–140, 2018.
- [17] A. Ambrosetti and P. L. Silvestrelli. Toward Tunable CO Adsorption on Defected Graphene: The Chemical Role of Ni (111) and Cu (111) Substrates. *The Journal of Physical Chemistry C*, 121(36):19828–19835, 2017.
- [18] E. Celasco, G. Carraro, A. Lusuan, M. Smerieri, J. Pal, M. Rocca, L. Savio, and L. Vattuone. CO chemisorption at vacancies of supported graphene films: a candidate for a sensor? *Physical Chemistry Chemical Physics*, 18(28):18692–18696, 2016.
- [19] S. Oida, F. R. McFeely, J. B. Hannon, R. M. Tromp, M. Copel, Z. Chen, Y. Sun, D. B. Farmer, and J. Yurkas. Decoupling graphene from SiC(0001) via oxidation. *Physical Review B*, 82(4):041411, 2010.
- [20] P. Sutter, J. T. Sadowski, and E. A. Sutter. Chemistry under cover: tuning metal-graphene interaction by reactive intercalation. *Journal of the American Chemical Society*, 132(23):8175–8179, 2010.
- [21] C. Riedl, C. Coletti, T. Iwasaki, A. A. Zakharov, and U. Starke. Quasi-free-standing epitaxial graphene on SiC obtained by hydrogen intercalation. *Physical review letters*, 103(24):246804, 2009.
- [22] A. Ghosh, K. S. Subrahmanyam, K. S. Krishna, S. Datta, A. Govindaraj, S. K. Pati, and C. N. R. Rao. Uptake of H₂ and CO₂ by graphene. *The Journal of Physical Chemistry C*, 112(40):15704–15707, 2008.
- [23] Y. Yao, Q. Fu, Y. Y. Zhang, X. Weng, H. Li, M. Chen, L. Jin, A. Dong, R. Mu, P. Jiang, L. Liu, H. Bluhm, Z. Liu, S. B. Zhang, and X. Bao. Graphene cover-promoted metal-catalyzed reactions. *Proceedings of the National Academy of Sciences*, 111(48):17023–17028, 2014.
- [24] M. Smerieri, E. Celasco, G. Carraro, A. Lusuan, J. Pal, G. Bracco, M. Rocca, L. Savio, and L. Vattuone. Enhanced chemical reactivity of pristine graphene interacting strongly with a substrate: chemisorbed carbon monoxide on graphene/nickel (111). *ChemCatChem*, 7(15):2328–2331, 2015.
- [25] L. Zhao, R. He, K. T. Rim, T. Schiros, K. S. Kim, H. Zhou, C. Gutiérrez, S. P. Chockalingam, C. J. Arguello, L. Pálková, D. Nordlund, M. S. Hybertsen, D. R. Reichman, T. F. Heinz, P. Kim, A. Pinczuk, G. W. Flynn, and A. N. Pasupathy. Visualizing individual nitrogen dopants in monolayer graphene. *Science*, 333(6045):999–1003, 2011.

- [26] R. Lv, Q. Li, A. R. Botello-Méndez, T. Hayashi, B. Wang, A. Berkdemir, Q. Hao, A. L. Elías, R. Cruz-Silva, H. R. Gutiérrez, Y. A. Kim, H. Muramatsu, J. Zhu, M. Endo, H. Terrones, J. C. Charlier, M. Pan, and M. Terrones. Nitrogen-doped graphene: beyond single substitution and enhanced molecular sensing. *Scientific reports*, 2:586, 2012.
- [27] D. Usachov, O. Vilkov, A. Gruneis, D. Haberer, A. Fedorov, V. K. Adamchuk, A. B. Preobrajenski, P. Dudin, A. Barinov, M. Oehzelt, C. Laubschat, and D. V. Vyalikh. Nitrogen-doped graphene: efficient growth, structure, and electronic properties. *Nano letters*, 11(12):5401–5407, 2011.
- [28] A. Martín-Recio, C. Romero-Muñoz, P. Pou, R. Pérez, and J. Gómez-Rodríguez. Purely substitutional nitrogen on graphene/Pt (111) unveiled by STM and first principles calculations. *Nanoscale*, 8(40):17686–17693, 2016.
- [29] F. Orlando, P. Lacovig, M. Dalmiglio, A. Baraldi, R. Larciprete, and S. Lizzit. Synthesis of nitrogen-doped epitaxial graphene via plasma-assisted method: Role of the graphene–substrate interaction. *Surface Science*, 643:214–221, 2016.
- [30] R. Costantini, M. Stredansky, D. Cvetko, G. Kladnik, A. Verdini, P. Sigalotti, F. Cilento, F. Salvador, A. De Luisa, D. Benedetti, L. Floreano, A. Morgante, A. Cosaro, and M. Dell’Angela. ANCHOR-SUNDYN: A novel endstation for time resolved spectroscopy at the ALOISA beamline. *Journal of Electron Spectroscopy and Related Phenomena*, 229:7–12, 2018.
- [31] A. K. Geim and K. S. Novoselov. The rise of graphene. In *Nanoscience and technology: a collection of reviews from nature journals*, pages 11–19. World Scientific, 2010.
- [32] S. Forti and U. Starke. Epitaxial graphene on SiC: from carrier density engineering to quasi-free standing graphene by atomic intercalation. *Journal of Physics D: Applied Physics*, 47(9):094013, 2014.
- [33] W. Norimatsu and M. Kusunoki. Epitaxial graphene on SiC {0001}: advances and perspectives. *Physical Chemistry Chemical Physics*, 16(8):3501–3511, 2014.
- [34] A. H. C. Neto, F. Guinea, N. M. R. Peres, K. S. Novoselov, and A. K. Geim. The electronic properties of graphene. *Reviews of modern physics*, 81(1):109, 2009.
- [35] P. R. Wallace. The band theory of graphite. *Physical review*, 71(9):622, 1947.
- [36] K. S. Novoselov, A. K. Geim, S. V. Morozov, D. Jiang, M. I. Katsnelson, I. V. Grigorieva, S. V. Dubonos, and A. A. Firsov. Two-dimensional gas of massless Dirac fermions in graphene. *nature*, 438(7065):197–200, 2005.
- [37] A. S. Mayorov, R. V. Gorbachev, S. V. Morozov, L. Britnell, R. Jalil, L. A. Ponomarenko, P. Blake, K. S. Novoselov, K. Watanabe, T. Taniguchi, and A. K. Geim. Micrometer-scale ballistic transport in encapsulated graphene at room temperature. *Nano letters*, 11(6):2396–2399, 2011.
- [38] C. Lee, X. Wei, J. W. Kysar, and J. Hone. Measurement of the elastic properties and intrinsic strength of monolayer graphene. *science*, 321(5887):385–388, 2008.
- [39] A.A. Balandin, S. Ghosh, I. Bao, W. and Calizo, D. Teweldebrhan, F. Miao, and C.N. Lau. Extremely High Thermal Conductivity of Graphene: Experimental Study. *Nature materials*, 10:569–581, 2011.

- [40] R. R. Nair, P. Blake, A. N. Grigorenko, K. S. Novoselov, T. J. Booth, T. Stauber, N. M. R. Peres, and A. K. Geim. Fine structure constant defines visual transparency of graphene. *Science*, 320(5881):1308–1308, 2008.
- [41] K. S. Novoselov, V. I. Fal’ko, L. Colombo, P. R. Gellert, M. G. Schwab, and K. Kim. A roadmap for graphene. *nature*, 490(7419):192–200, 2012.
- [42] L. Ci, L. Song, D. Jariwala, A. L. Elias, W. Gao, M. Terrones, and P. M. Ajayan. Graphene shape control by multistage cutting and transfer. *Advanced Materials*, 21(44):4487–4491, 2009.
- [43] X. Liang, A. S. P. Chang, Y. Zhang, B. D Harteneck, H. Choo, D. L. Olynick, and S. Cabrini. Electrostatic force assisted exfoliation of prepatterned few-layer graphenes into device sites. *Nano letters*, 9(1):467–472, 2009.
- [44] L. Yuan, J. Ge, X. Peng, Q. Zhang, Z. Wu, Y. Jian, X. Xiong, H. Yin, and J. Han. A reliable way of mechanical exfoliation of large scale two dimensional materials with high quality. *AIP Advances*, 6(12):125201, 2016.
- [45] D. R. Dreyer, R. S. Ruoff, and C. W. Bielawski. From conception to realization: an historical account of graphene and some perspectives for its future. *Angewandte Chemie International Edition*, 49(49):9336–9344, 2010.
- [46] Structural and electronic properties of epitaxial graphene on SiC (0001): a review of growth, characterization, transfer doping and hydrogen intercalation.
- [47] U. Starke and C. Riedl. Epitaxial graphene on SiC (0001) and: from surface reconstructions to carbon electronics. *Journal of Physics: Condensed Matter*, 21(13):134016, 2009.
- [48] A. Kumar, K. Banerjee, and P. Liljeroth. Molecular assembly on two-dimensional materials. *Nanotechnology*, 28(8):082001, 2017.
- [49] J. Cai, P. Ruffieux, R. Jaafar, M. Bieri, T. Braun, S. Blankenburg, M. Muoth, A. P. Seitsonen, M. Saleh, X. Feng, K. Müllen, and R. Fasel. Atomically precise bottom-up fabrication of graphene nanoribbons. *Nature*, 466(7305):470–473, 2010.
- [50] L. Talirz, P. Ruffieux, and R. Fasel. On-surface synthesis of atomically precise graphene nanoribbons. *Advanced materials*, 28(29):6222–6231, 2016.
- [51] A. Fairbrother, J.-R. Sanchez-Valencia, B. Lauber, I. Shorubalko, P. Ruffieux, T. Hintermann, and R. Fasel. High vacuum synthesis and ambient stability of bottom-up graphene nanoribbons. *Nanoscale*, 9(8):2785–2792, 2017.
- [52] H. Sakaguchi, S. Song, T. Kojima, and T. Nakae. Homochiral polymerization-driven selective growth of graphene nanoribbons. *Nature chemistry*, 9(1):57, 2017.
- [53] L. Lafferentz, V. Eberhardt, C. Dri, C. Africh, G. Comelli, F. Esch, S. Hecht, and L. Grill. Controlling on-surface polymerization by hierarchical and substrate-directed growth. *Nature chemistry*, 4(3):215–220, 2012.
- [54] M. Bieri, M. Treier, J. Cai, K. Ait-Mansour, P. Ruffieux, O. Gröning, P. Gröning, M. Kastler, R. Rieger, X. Feng, , K. Müllen, and R. Fasel. Porous graphenes: two-dimensional polymer synthesis with atomic precision. *Chemical communications*, (45):6919–6921, 2009.

- [55] C. Moreno, M. Vilas-Varela, B. Kretz, A. Garcia-Lekue, M. V. Costache, M. Paradinas, M. Panighel, G. Ceballos, S. O Valenzuela, D. Peña, and A. Mugarza. Bottom-up synthesis of multifunctional nanoporous graphene. *Science*, 360(6385):199–203, 2018.
- [56] L. L. Patera, C. Africh, R. S. Weatherup, R. Blume, S. Bhardwaj, C. Castellarin-Cudia, A. Knop-Gericke, R. Schloegl, G. Comelli, S. Hofmann, and C. Cepek. In situ observations of the atomistic mechanisms of Ni catalyzed low temperature graphene growth. *ACS nano*, 7(9):7901–7912, 2013.
- [57] L. Zhao, K. T. Rim, H. Zhou, R. He, T. F. Heinz, A. Pinczuk, G. W. Flynn, and A. N. Pasupathy. Influence of copper crystal surface on the CVD growth of large area monolayer graphene. *Solid State Communications*, 151(7):509–513, 2011.
- [58] J. Coraux, A. T. N’Diaye, C. Busse, and T. Michely. Structural coherency of graphene on Ir (111). *Nano letters*, 8(2):565–570, 2008.
- [59] P. W. Sutter, J.-I. Flege, and E. A. Sutter. Epitaxial graphene on ruthenium. *Nature materials*, 7(5):406–411, 2008.
- [60] N. Liu, L. Fu, B. Dai, K. Yan, X. Liu, R. Zhao, Y. Zhang, and Z. Liu. Universal segregation growth approach to wafer-size graphene from non-noble metals. *Nano letters*, 11(1):297–303, 2011.
- [61] P. Sutter, J. T. Sadowski, and E. Sutter. Graphene on Pt (111): Growth and substrate interaction. *Physical Review B*, 80(24):245411, 2009.
- [62] K. F. McCarty, P. J. Feibelman, E. Loginova, and N. C. Bartelt. Kinetics and thermodynamics of carbon segregation and graphene growth on Ru (0 0 0 1). *Carbon*, 47(7):1806–1813, 2009.
- [63] J. C. Shelton, H. R. Patil, and J. M. Blakely. Equilibrium segregation of carbon to a nickel (111) surface: A surface phase transition. *Surface Science*, 43(2):493–520, 1974.
- [64] A. Grüneis, K. Kummer, and D. V. Vyalikh. Dynamics of graphene growth on a metal surface: a time-dependent photoemission study. *New Journal of Physics*, 11(7):073050, 2009.
- [65] L. L. Patera, F. Bianchini, C. Africh, C. Dri, G. Soldano, M. M. Mariscal, M. Peressi, and G. Comelli. Real-time imaging of adatom-promoted graphene growth on nickel. *Science*, 359(6381):1243–1246, 2018.
- [66] A. Dahal and M. Batzill. Graphene–nickel interfaces: a review. *Nanoscale*, 6(5):2548–2562, 2014.
- [67] A. Varykhalov, J. Sánchez-Barriga, A. M. Shikin, C. Biswas, E. Vescovo, A. Rybkin, D. Marchenko, and O. Rader. Electronic and magnetic properties of quasifreestanding graphene on Ni. *Physical review letters*, 101(15):157601, 2008.
- [68] B. Guo, L. Fang, B. Zhang, and J. R. Gong. Graphene doping: a review. *Insciences J*, 1(2):80–89, 2011.
- [69] S. M. Shinde, E. Kano, G. Kalita, M. Takeguchi, A. Hashimoto, and M. Tanemura. Grain structures of nitrogen-doped graphene synthesized by solid source-based chemical vapor deposition. *Carbon*, 96:448–453, 2016.

- [70] A. Zabet-Khosousi, L. Zhao, L. Pálová, M. S. Hybertsen, D. R. Reichman, A. N. Papaty, and G. W. Flynn. Segregation of sublattice domains in nitrogen-doped graphene. *Journal of the American Chemical Society*, 136(4):1391–1397, 2014.
- [71] N. Li, Z. Wang, K. Zhao, Z. Shi, Z. Gu, and S. Xu. Large scale synthesis of n-doped multi-layered graphene sheets by simple arc-discharge method. *Carbon*, 48(1):255–259, 2010.
- [72] X. Wang, X. Li, L. Zhang, Y. Yoon, P. K. Weber, H. Wang, J. Guo, and H. Dai. N-doping of graphene through electrothermal reactions with ammonia. *Science*, 324(5928):768–771, 2009.
- [73] M. Telychko, P. Mutombo, M. Ondracek, P. Hapala, F. C. Bocquet, J. Kolorenc, M. Vondracek, P. Jelinek, and M. Svec. Achieving high-quality single-atom nitrogen doping of graphene/SiC (0001) by ion implantation and subsequent thermal stabilization. *ACS nano*, 8(7):7318–7324, 2014.
- [74] U. Bangert, W. Pierce, D. M. Kepaptsoglou, Q. Ramasse, R. Zan, M. H. Gass, J. A. Van den Berg, C. B. Boothroyd, J. Amani, and H. Hofsass. Ion Implantation of Graphene- Toward IC Compatible Technologies. *Nano Letters*, 13(10):4902–4907, 2013.
- [75] Y.-P. Lin, Y. Ksari, J. Prakash, L. Giovannelli, J.-C. Valmalette, and J.-M. Themlin. Nitrogen-doping processes of graphene by a versatile plasma-based method. *Carbon*, 73:216–224, 2014.
- [76] D. Golberg, Y. Bando, L. Bourgeois, K. Kurashima, and T. Sato. Large-scale synthesis and HRTEM analysis of single-walled B-and N-doped carbon nanotube bundles. *Carbon*, 38(14):2017–2027, 2000.
- [77] T. O. Wehling, M. I. Katsnelson, and A. I. Lichtenstein. Adsorbates on graphene: Impurity states and electron scattering. *Chemical Physics Letters*, 476(4-6):125–134, 2009.
- [78] L. Gomez De Arco, Y. Zhang, C. W. Schlenker, K. Ryu, M. E. Thompson, and C. Zhou. Continuous, highly flexible, and transparent graphene films by chemical vapor deposition for organic photovoltaics. *ACS nano*, 4(5):2865–2873, 2010.
- [79] G. Ko, H.-Y. Kim, J. Ahn, Y.-M. Park, K.-Y. Lee, and J. Kim. Graphene-based nitrogen dioxide gas sensors. *Current Applied Physics*, 10(4):1002–1004, 2010.
- [80] O. Leenaerts, B. Partoens, and F. M. Peeters. Adsorption of H₂O, NH₃, CO, NO₂, and NO on graphene: A first-principles study. *Physical Review B*, 77(12):125416, 2008.
- [81] Jun Zhang, Xianghong Liu, Giovanni Neri, and Nicola Pinna. Nanostructured materials for room-temperature gas sensors. *Advanced Materials*, 28(5):795–831, 2016.
- [82] Y.-H. Zhang, Y.-B. Chen, K.-G. Zhou, C.-H. Liu, J. Zeng, H.-L. Zhang, and Y. Peng. Improving gas sensing properties of graphene by introducing dopants and defects: a first-principles study. *Nanotechnology*, 20(18):185504, 2009.
- [83] E. Grånäs, M. Andersen, M. A. Arman, T. Gerber, B. Hammer, J. Schnadt, J. N. Andersen, T. Michely, and J. Knudsen. Co intercalation of graphene on Ir(111) in the millibar regime. *The Journal of Physical Chemistry C*, 117(32):16438–16447, 2013.

- [84] L. Jin, Q. Fu, A. Dong, Y. Ning, Z. Wang, H. Bluhm, and X. Bao. Surface chemistry of CO on Ru (0001) under the confinement of graphene cover. *The Journal of Physical Chemistry C*, 118(23):12391–12398, 2014.
- [85] R. Mu, Q. Fu, L. Jin, L. Yu, G. Fang, D. Tan, and X. Bao. Visualizing chemical reactions confined under graphene. *Angewandte Chemie International Edition*, 51(20):4856–4859, 2012.
- [86] S. L. Kovalenko, B. V. Andryushechkin, and K. N. Eltsov. STM study of oxygen intercalation at the graphene/Ni (111) interface. *Carbon*, 164:198–206, 2020.
- [87] V. D. Pham, J. Lagoute, O. Mouhoub, F. Joucken, V. Repain, C. Chacon, A. Bellec, Y. Girard, and S. Rousset. Electronic interaction between nitrogen-doped graphene and porphyrin molecules. *ACS nano*, 8(9):9403–9409, 2014.
- [88] G. Carraro, E. Celasco, M. Smerieri, L. Savio, G. Bracco, M. Rocca, and L. Vattuone. Chemisorption of CO on N-doped graphene on Ni (111). *Applied Surface Science*, 428:775–780, 2018.
- [89] W. Wang, Y. Zhang, C. Shen, and Y. Chai. Adsorption of CO molecules on doped graphene: A first-principles study. *AIP advances*, 6(2):025317, 2016.
- [90] S. Agnoli and M. Favaro. Doping graphene with boron: a review of synthesis methods, physicochemical characterization, and emerging applications. *Journal of Materials Chemistry A*, 4(14):5002–5025, 2016.
- [91] J. Dai, J. Yuan, and P. Giannozzi. Gas adsorption on graphene doped with B, N, Al, and S: A theoretical study. *Applied Physics Letters*, 95(23):232105, 2009.
- [92] Z. M. Ao, J. Yang, S. Li, and Q. Jiang. Enhancement of CO detection in Al doped graphene. *Chemical Physics Letters*, 461(4-6):276–279, 2008.
- [93] C. C. Ma, X. H. Shao, and D. P. Cao. Nitrogen-doped graphene as an excellent candidate for selective gas sensing. *Science China Chemistry*, 57(6):911–917, 2014.
- [94] Y. Gamo, A. Nagashima, M. Wakabayashi, M. Terai, and C. Oshima. Atomic structure of monolayer graphite formed on Ni (111). *Surface Science*, 374(1-3):61–64, 1997.
- [95] Z. Zou, V. Carnevali, M. Jugovac, L. L. Patera, A. Sala, M. Panighel, C. Cepek, G. Soldano, M. M. Mariscal, M. Peressi, G. Comelli, and C. Africh. Graphene on nickel (100) micrograins: Modulating the interface interaction by extended moiré superstructures. *Carbon*, 130:441–447, 2018.
- [96] D. A. Pudikov, E. V. Zhizhin, A. G. Rybkin, A. A. Rybkina, Y. M. Zhukov, O. Y. Vilkov, and A. M. Shikin. Electronic structure of graphene on Ni (111) and Ni (100) surfaces. *Physics of the Solid State*, 58(12):2550–2554, 2016.
- [97] Y. S. Dedkov, M. Fonin, and C. Laubschat. A possible source of spin-polarized electrons: The inert graphene/Ni (111) system. *Applied Physics Letters*, 92(5):052506, 2008.
- [98] A. Dahal, H. Coy-Diaz, R. Addou, J. Lallo, E. Sutter, and M. Batzill. Preparation and characterization of Ni (111)/graphene/Y₂O₃ (111) heterostructures. *Journal of Applied Physics*, 113(19):194305, 2013.

- [99] R. S. Weatherup, B. Dlubak, and S. Hofmann. Kinetic control of catalytic CVD for high-quality graphene at low temperatures. *ACS nano*, 6(11):9996–10003, 2012.
- [100] C. Africh, C. Cepek, L. L. Patera, G. Zamborlini, P. Genoni, T. O. Menteş, A. Sala, A. Locatelli, and G. Comelli. Switchable graphene-substrate coupling through formation/dissolution of an intercalated Ni-carbide layer. *Scientific reports*, 6:19734, 2016.
- [101] S. Achilli, S. Tognolini, E. Fava, S. Ponzoni, G. Drera, C. Cepek, L. L. Patera, C. Africh, E. del Castillo, M. I. Trioni, and S. Pagliara. Surface states characterization in the strongly interacting graphene/Ni (111) system. *New Journal of Physics*, 20(10):103039, 2018.
- [102] A. Garcia-Lekue, T. Balashov, M. Olle, G. Ceballos, A. Arnau, P. Gambardella, D. Sanchez-Portal, and A. Mugarza. Spin-dependent electron scattering at graphene edges on Ni (111). *Physical review letters*, 112(6):066802, 2014.
- [103] J. Song, M. Bernien, C. B. Wu, and W. Kuch. Tuning the Electronic Properties of Rotated Graphene on Ni (111) by Nickel Carbide Intercalation. *The Journal of Physical Chemistry C*, 120(3):1546–1555, 2016.
- [104] R. Rameshan, V. Vonk, D. Franz, J. Drnec, S. Penner, A. Garhofer, F. Mittendorfer, A. Stierle, and B. Klötzer. Role of precursor carbides for graphene growth on Ni (111). *Scientific reports*, 8(1):1–13, 2018.
- [105] Y. Nishijima and G. Oster. Moiré patterns: their application to refractive index and refractive index gradient measurements. *JOSA*, 54(1):1–5, 1964.
- [106] M. Wei, Q. Fu, Y. Yang, W. Wei, E. Crumlin, H. Bluhm, and X. Bao. Modulation of surface chemistry of CO on Ni (111) by surface graphene and carbidic carbon. *The Journal of Physical Chemistry C*, 119(24):13590–13597, 2015.
- [107] F. Bianchini, L. L. Patera, M. Peressi, C. Africh, and G. Comelli. Atomic scale identification of coexisting graphene structures on Ni(111). *The journal of physical chemistry letters*, 5(3):467–473, 2014.
- [108] W. Zhao, S. M. Kozlov, O. Höfert, K. Gotterbarm, M. P. A. Lorenz, F. Vines, C. Papp, A. Görling, and H. P. Steinrück. Graphene on Ni (111): Coexistence of different surface structures. *The Journal of Physical Chemistry Letters*, 2(7):759–764, 2011.
- [109] R. J. Koch, M. Weser, W. Zhao, F. Viñes, K. Gotterbarm, S. M. Kozlov, O. Höfert, M. Ostler, C. Papp, J. Gebhardt, H. P. Steinrück, A. Görling, and T. Seyller. Growth and electronic structure of nitrogen-doped graphene on Ni (111). *Physical Review B*, 86(7):075401, 2012.
- [110] W. Zhao, O. Hofert, K. Gotterbarm, J. F. Zhu, C. Papp, and H. P. Steinrück. Production of nitrogen-doped graphene by low-energy nitrogen implantation. *The Journal of Physical Chemistry C*, 116(8):5062–5066, 2012.
- [111] F. Joucken, Y. Tison, J. Lagoute, J. Dumont, D. Cabosart, B. Zheng, V. Repain, C. Chacon, Y. Girard, A. R. Botello-Méndez, S. Rousset, R. Sporcken, J-C Charlier, and L. Henrard. Localized state and charge transfer in nitrogen-doped graphene. *Physical Review B*, 85(16):161408, 2012.

- [112] D. Usachov, A. Fedorov, O. Vilkov, B. Senkovskiy, V. K. Adamchuk, L. V. Yashina, A. A. Volykhov, M. Farjam, N. I. Verbitskiy, A. Grüneis, C. Laubschat, and D. V. Vyalikh. The chemistry of imperfections in N-graphene. *Nano letters*, 14(9):4982–4988, 2014.
- [113] H. Conrad, G. Ertl, J. Küppers, and E. E. Latta. Adsorption of CO on clean and oxygen covered Ni (111) surfaces. *Surface Science*, 57(2):475–484, 1976.
- [114] J. C. Bertolini and B. Tardy. Vibrational EELS studies of CO chemisorption on clean and carbided (111),(100) and (110) nickel surfaces. *Surface Science*, 102(1):131–150, 1981.
- [115] N. Ikemiya, T. Suzuki, and M. Ito. Adlayer structures of CO adsorbed on Ni (111) electrode surfaces studied by in situ STM combined with IRAS. *Surface science*, 466(1-3):119–126, 2000.
- [116] A. Eichler. CO adsorption on Ni (111) - a density functional theory study. *Surface Science*, 526(3):332–340, 2003.
- [117] W. Erley, K. Besocke, and H. Wagner. Absolute coverage determination of CO on Ni (111). *The Journal of Chemical Physics*, 66(12):5269–5273, 1977.
- [118] J. C. Campuzano, R. Dus, and R. G. Greenler. The sticking probability, dipole moment, and absolute coverage of CO on Ni (111). *Surface Science*, 102(1):172–184, 1981.
- [119] K. Oura, V. G. Lifshits, A. A. Saranin, A. V. Zotov, and M. Katayama. *Surface science: an introduction*. Springer Science & Business Media, 2013.
- [120] C. J. Chen. *Introduction to Scanning Tunneling Microscopy*, volume 4. Oxford University Press, 1993.
- [121] J. Bardeen. Tunnelling from a many-particle point of view. *Physical Review Letters*, 6(2):57, 1961.
- [122] J. Tersoff and D. R. Hamann. Theory of the scanning tunneling microscope. *Physical Review B*, 31(2):805, 1985.
- [123] R. J. Hamers. Atomic-resolution surface spectroscopy with the scanning tunneling microscope. *Annual Review of Physical Chemistry*, 40(1):531–559, 1989.
- [124] R. M. Feenstra. Scanning tunneling spectroscopy. *Surface science*, 299:965–979, 1994.
- [125] RM Feenstra and Joseph A Stroscio. Real-space determination of surface structure by scanning tunneling microscopy. *Physica Scripta*, 1987(T19A):55, 1987.
- [126] D. Briggs. Practical Surface Analysis, Auger and X-ray Photoelectron Spectroscopy. *J. Wiley & Sons*, 1990.
- [127] H Lüth. Morphology and Structure of Surfaces and interfaces. In *Surfaces and Interfaces of Solid Materials*, pages 72–135. Springer, 1995.
- [128] C. S. Fadley. Electron Spectroscopy: Theory, Techniques and Applications, volume 2, chapter Basic concepts of XPS, 1978.

- [129] S. Doniach and M. Sunjic. Many-electron singularity in X-ray photoemission and X-ray line spectra from metals. *Journal of Physics C: Solid State Physics*, 3(2):285, 1970.
- [130] Giuseppe Grosso and Giuseppe Pastori Parravicini. *Solid State Physics, Second Edition*. Academic Press, 2014.
- [131] S. Fiori, D. Perilli, M. Panighel, C. Cepek, A. Ugolotti, A. Sala, H. Liu, G. Comelli, C. Di Valentin, and C. Africh. "Inside Out" Growth Method for High-Quality Nitrogen-Doped Graphene. *Carbon*, 171:704–710, 2021.
- [132] W. Auwärter, A. Weber-Bargioni, S. Brink, A. Riemann, A. Schiffrin, M. Ruben, and J. V. Barth. Controlled metalation of self-assembled porphyrin nanoarrays in two dimensions. *ChemPhysChem*, 8(2):250–254, 2007.
- [133] F. Buchner, V. Schwald, K. Comanici, H.-P. Steinrück, and H. Marbach. Microscopic Evidence of the Metalation of a Free-Base Porphyrin Monolayer with Iron. *ChemPhysChem*, 8(2):241–243, 2007.
- [134] A. Kretschmann, M.-M. Walz, K. Flechtner, H.-P. Steinrück, and J. M. Gottfried. Tetraphenylporphyrin picks up zinc atoms from a silver surface. *Chemical communications*, (6):568–570, 2007.
- [135] J. M. Gottfried, K. Flechtner, A. Kretschmann, T. Lukasczyk, and H.-P. Steinrück. Direct synthesis of a metalloporphyrin complex on a surface. *Journal of the American Chemical Society*, 128(17):5644–5645, 2006.
- [136] M. Panighel, G. Di Santo, M. Caputo, C. Lal, B. Taleatu, and A. Goldoni. Review of 2H-tetraphenylporphyrins metalation in ultra-high vacuum on metal surfaces. In *Journal of Physics: Conference Series*, volume 470, page 012012. IOP Publishing, 2013.
- [137] M. Chen, X. Feng, L. Zhang, H. Ju, Q. Xu, J. Zhu, J. M. Gottfried, K. Ibrahim, H. Qian, and J. Wang. Direct synthesis of nickel (ii) tetraphenylporphyrin and its interaction with a Au (111) surface: a comprehensive study. *The Journal of Physical Chemistry C*, 114(21):9908–9916, 2010.
- [138] A. Goldoni, C. A. Pignedoli, G. Di Santo, C. Castellarin-Cudia, E. Magnano, F. Bondino, A. Verdini, and D. Passerone. Room temperature metalation of 2H-TPP monolayer on iron and nickel surfaces by picking up substrate metal atoms. *ACS nano*, 6(12):10800–10807, 2012.
- [139] L. G. Teugels, L. G. Avila-Bront, and S. J. Sibener. Chiral domains achieved by surface adsorption of achiral nickel tetraphenyl- or octaethylporphyrin on smooth and locally kinked Au (111). *The Journal of Physical Chemistry C*, 115(6):2826–2834, 2011.
- [140] T. Yokoyama, S. Yokoyama, T. Kamikado, and S. Mashiko. Nonplanar adsorption and orientational ordering of porphyrin molecules on Au (111). *The Journal of Chemical Physics*, 115(8):3814–3818, 2001.
- [141] J. Brede, M. Linares, S. Kuck, J. Schwöbel, A. Scarfato, S.-H. Chang, G. Hoffmann, R. Wiesendanger, R. Lensen, P. H. J. Kouwer, J. Hoogboom, A. E. Rowan, M. Bröring, M. Funk, S. Stafström, F. Zerbetto, and R. Lazzaroni. Dynamics of molecular self-ordering in tetraphenyl porphyrin monolayers on metallic substrates. *Nanotechnology*, 20(27):275602, 2009.

- [142] G. Di Santo, S. Blankenburg, C. Castellarin-Cudia, M. Fanetti, P. Borghetti, L. Sangaletti, L. Floreano, A. Verdini, E. Magnano, F. Bondino, C. A. Pignedoli, M.-T. Nguyen, R. Gaspari, D. Passerone, and A. Goldoni. Supramolecular Engineering through Temperature-Induced Chemical Modification of 2H-Tetraphenylporphyrin on Ag (111): Flat Phenyl Conformation and Possible Dehydrogenation Reactions. *Chemistry—A European Journal*, 17(51):14354–14359, 2011.
- [143] F. Buchner, K. Flechtner, Y. Bai, E. Zillner, I. Kellner, H.-P. Steinrück, H. Marbach, and J. M. Gottfried. Coordination of iron atoms by tetraphenylporphyrin monolayers and multilayers on Ag (111) and formation of iron-tetraphenylporphyrin. *The Journal of Physical Chemistry C*, 112(39):15458–15465, 2008.
- [144] R. González-Moreno, C. Sánchez-Sánchez, M. Trelka, R. Otero, A. Cossaro, A. Verdini, L. Floreano, M. Ruiz-Bermejo, A. García-Lekue, J. Á. Martín-Gago, and C. Rogero. Following the metalation process of protoporphyrin IX with metal substrate atoms at room temperature. *The Journal of Physical Chemistry C*, 115(14):6849–6854, 2011.
- [145] M. S. Dyer, A. Robin, S. Haq, R. Raval, M. Persson, and J. Klimes. Understanding the interaction of the porphyrin macrocycle to reactive metal substrates: structure, bonding, and adatom capture. *ACS nano*, 5(3):1831–1838, 2011.
- [146] K. Diller, F. Klappenberger, M. Marschall, K. Hermann, A. Nefedov, C. Wöll, and J. V. Barth. Self-metalation of 2H-tetraphenylporphyrin on Cu (111): An x-ray spectroscopy study. *The Journal of chemical physics*, 136(1):014705, 2012.
- [147] X. Hu, T. Björkman, H. Lipsanen, L. Sun, and A. V. Krasheninnikov. Solubility of boron, carbon, and nitrogen in transition metals: getting insight into trends from first-principles calculations. *The Journal of Physical Chemistry Letters*, 6(16):3263–3268, 2015.
- [148] C. Zhang, L. Fu, N. Liu, M. Liu, Y. Wang, and Z. Liu. Synthesis of nitrogen-doped graphene using embedded carbon and nitrogen sources. *Advanced materials*, 23(8):1020–1024, 2011.
- [149] V. Carnevali, L. L. Patera, G. Prandini, M. Jugovac, S. Modesti, G. Comelli, M. Persessi, and C. Africh. Doping of epitaxial graphene by direct incorporation of nickel adatoms. *Nanoscale*, 11(21):10358–10364, 2019.
- [150] W. Ho. Single-molecule chemistry. *The Journal of chemical physics*, 117(24):11033–11061, 2002.
- [151] M. Scardamaglia, B. Aleman, M. Amati, C. Ewels, P. Pochet, N. Reckinger, J.-F. Colomer, T. Skaltsas, N. Tagmatarchis, R. Snyders, L. Gregoratti, and C. Bittencourt. Nitrogen implantation of suspended graphene flakes: Annealing effects and selectivity of sp² nitrogen species. *Carbon*, 73:371–381, 2014.
- [152] D. E. Gardin, J. D. Batteas, M. A. Van Hove, and G. A. Somorjai. Carbon, nitrogen, and sulfur on Ni (111): formation of complex structures and consequences for molecular decomposition. *Surface science*, 296(1):25–35, 1993.
- [153] P. Jacobson, B. Stöger, A. Garhofer, G. S. Parkinson, M. Schmid, R. Caudillo, F. Mittendorfer, J. Redinger, and U. Diebold. Nickel carbide as a source of grain rotation in epitaxial graphene. *ACS nano*, 6(4):3564–3572, 2012.

- [154] P. Mallet, F. Varchon, C. Naud, L. Magaud, C. Berger, and J.-Y. Veuillen. Electron states of mono- and bilayer graphene on SiC probed by scanning-tunneling microscopy. *Physical Review B*, 76(4):041403, 2007.
- [155] D. Perilli, S. Fiori, M. Panighel, H. Liu, C. Cepek, M. Peressi, G. Comelli, C. Africh, and C. Di Valentin. Mechanism of CO intercalation Through the graphene/Ni (111) Interface and Effect of Doping. *The Journal of Physical Chemistry Letters*, (11), 2020.
- [156] J. S. Bunch, S. S. Verbridge, J. S. Alden, A. M. Van Der Zande, J. M. Parpia, H. G. Craighead, and P. L. McEuen. Impermeable atomic membranes from graphene sheets. *Nano letters*, 8(8):2458–2462, 2008.
- [157] P. Z. Sun, Q. Yang, W. J. Kuang, Y. V. Stebunov, W. Q. Xiong, J. Yu, R. R. Nair, M. I. Katsnelson, S. J. Yuan, I. V. Grigorieva, M. Lozada-Hidalgo, F. C. Wang, and A. K. Geim. Limits on gas impermeability of graphene. *Nature*, 579(7798):229–232, 2020.
- [158] A Ibrahim and Y. S. Lin. Gas permeation and separation properties of large-sheet stacked graphene oxide membranes. *Journal of Membrane Science*, 550:238–245, 2018.
- [159] I. Palacio, G. Otero-Irurueta, C. Alonso, J. I. Martínez, E. López-Elvira, I. Muñoz-Ochando, H. J. Salavagione, M. F. López, M. García-Hernández, J. Méndez, G. J. Ellis, and J. A. Martín-Gago. Chemistry below graphene: Decoupling epitaxial graphene from metals by potential-controlled electrochemical oxidation. *Carbon*, 129:837–846, 2018.
- [160] S. S. K. Mallineni, D. W. Boukhvalov, I. S. Zhidkov, A. I. Kukhareenko, A. I. Slesarev, A. F. Zatsepin, S. O. Cholakh, A. M. Rao, S. M. Serkiz, S. Bhattacharya, E. Z. Kurmaev, and R. Podila. Influence of dopants on the impermeability of graphene. *Nanoscale*, 9(18):6145–6150, 2017.
- [161] X. D. Zhu, Th. Rasing, and Y. R. Shen. Surface diffusion of CO on Ni (111) studied by diffraction of optical second-harmonic generation off a monolayer grating. *Physical review letters*, 61(25):2883, 1988.
- [162] T. S. Lin, H. J. Lu, and R. Gomer. Diffusion of CO on Ni (111) and Ni (115). *Surface Science*, 234(3):251–261, 1990.
- [163] S. Del Puppo, V. Carnevali, D. Perilli, F. Zarabara, A. Lodi Rizzini, G. Fornasier, E. Zupanič, S. Fiori, L. L. Patera, M. Panighel, Z. Zou, G. Comelli, C. Africh, C. Cepek, C. Di Valentin, and M. Peressi. Tuning graphene doping by carbon monoxide intercalation at the Ni(111) interface. *Carbon*, submitted.
- [164] P. Giannozzi, S. Baroni, N. Bonini, M. Calandra, R. Car, C. Cavazzoni, D. Ceresoli, G. L. Chiarotti, M. Cococcioni, I. Dabo, A. Dal Corso, S. De Gironcoli, S. Fabris, G. Fratesi, R. Gebauer, U. Gerstmann, C. Gougoussis, A. Kokalj, M. Lazzeri, L. Martin-Samos, N. Marzari, F. Mauri, R. Mazzarello, S. Paolini, A. Pasquarello, L. Paulatto, C. Sbraccia, S. Scandolo, G. Sclauzero, A. P. Seitsonen, A. Smogunov, P. Umari, and R. M. Wentzcovitch. QUANTUM ESPRESSO: a modular and open-source software project for quantum simulations of materials. *Journal of physics: Condensed matter*, 21(39):395502, 2009.

- [165] P. Giannozzi, O. Andreussi, T. Brumme, O. Bunau, M. B. Nardelli, M. Calandra, R. Car, C. Cavazzoni, D. Ceresoli, M. Cococcioni, N. Colonna, I. Carnimeo, A. Dal Corso, S. De Gironcoli, P. Delugas, R. A. DiStasio Jr, A. Ferretti, A. Floris, G. Fratesi, G. Fugallo, R. Gebauer, U. Gerstmann, F. Giustino, T. Gorni, J. Jia, M. Kawamura, H. Y. Ko, A. Kokalj, E. Küçükbenli, M. Lazzeri, M. Marsili, N. Marzari, F. Mauri, N. L. Nguyen, H. V. Nguyen, A. Otero-de-la Roza, L. Paulatto, S. Poncé, D. Rocca, R. Sabatini, B. Santra, M. Schlipf, A. P. Seitsonen, A. Smogunov, I. Timrov, T. Thonhauser, P. Umari, N. Vast, X. Wu, and S. Baroni. Advanced capabilities for materials modelling with quantum ESPRESSO. *Journal of Physics: Condensed Matter*, 29(46):465901, 2017.
- [166] D. Vanderbilt. Soft self-consistent pseudopotentials in a generalized eigenvalue formalism. *Physical review B*, 41(11):7892, 1990.
- [167] J. P. Perdew, K. Burke, and M. Ernzerhof. Generalized gradient approximation made simple. *Physical review letters*, 77(18):3865, 1996.
- [168] S. Grimme. Semiempirical GGA-type density functional constructed with a long-range dispersion correction. *Journal of computational chemistry*, 27(15):1787–1799, 2006.
- [169] H. J. Monkhorst and J. D. Pack. Special points for Brillouin-zone integrations. *Physical review B*, 13(12):5188, 1976.
- [170] G. Henkelman, B. P. Uberuaga, and H. Jónsson. A climbing image nudged elastic band method for finding saddle points and minimum energy paths. *The Journal of chemical physics*, 113(22):9901–9904, 2000.
- [171] A. Kokalj. XCrySDen—a new program for displaying crystalline structures and electron densities. *Journal of Molecular Graphics and Modelling*, 17(3-4):176–179, 1999.
- [172] P. Nečas, D. and Klapetek. Gwyddion: an open-source software for SPM data analysis. *Open Physics*, 10(1):181–188, 2012.